Karlsruhe Series in Photonics & Communications, Vol. 25

Simon Schneider

Optical coherence tomography for characterization of nanocomposite materials

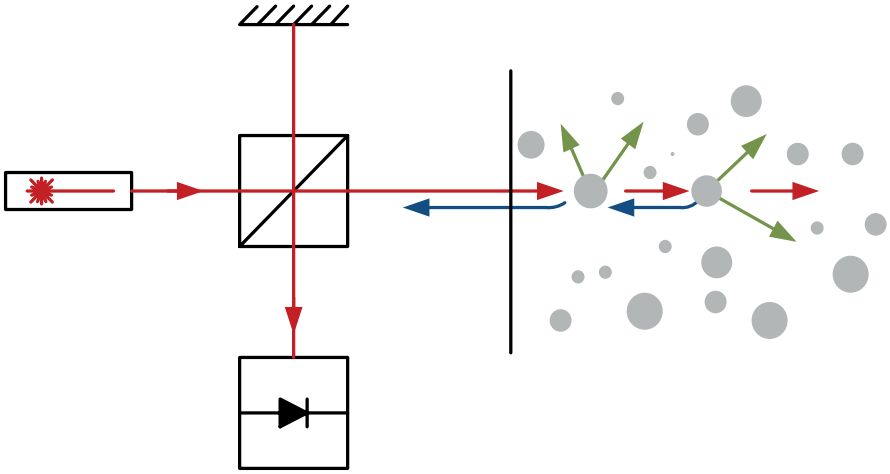

Scientific Publishing

Simon Schneider

Optical coherence tomography for characterization of nanocomposite materials

Karlsruhe Series in Photonics & Communications, Vol. 25
Edited by Profs. C. Koos, W. Freude and S. Randel

Karlsruhe Institute of Technology (KIT)
Institute of Photonics and Quantum Electronics (IPQ)
Germany

Optical coherence tomography for characterization of nanocomposite materials

by
Simon Schneider

KIT Scientific Publishing

Karlsruher Institut für Technologie
Institut für Photonik und Quantenelektronik

Optical coherence tomography for characterization
of nanocomposite materials

Zur Erlangung des akademischen Grades eines Doktor-Ingenieurs
von der KIT-Fakultät für Elektrotechnik und Informationstechnik des
Karlsruher Instituts für Technologie (KIT) genehmigte Dissertation

von Dipl.-Ing. Simon Schneider

Tag der mündlichen Prüfung: 29. November 2019
Hauptreferent: Prof. Dr.-Ing. Christian Koos
Korreferenten: Prof. Dr.-Ing. Dr. h.c. Wolfgang Freude
Prof. Dr. rer. nat. Wilhelm Stork

Impressum

Scientific Publishing

Karlsruher Institut für Technologie (KIT)
KIT Scientific Publishing
Straße am Forum 2
D-76131 Karlsruhe

KIT Scientific Publishing is a registered trademark
of Karlsruhe Institute of Technology.
Reprint using the book cover is not allowed.

www.ksp.kit.edu

Print on Demand 2020 – Gedruckt auf FSC-zertifiziertem Papier

ISSN 1865-1100
ISBN 978-3-7315-1027-7
DOI 10.5445/KSP/1000117929

Table of Contents

Kurzfassung

Nanoverbundmaterialien bestehen aus einem Träger-Material, auch als Matrix-Material bezeichnet, und einem nanoskaligen Füllstoff und spielen eine zunehmend wichtige Rolle in vielen Bereichen des industriellen, medizinischen oder des alltäglichen Umfelds. Die Attraktivität von Nanomaterialien beruht auf deren einzigartigen physikalischen Eigenschaften, die über jene von klassischen Materialien hinausgehen. So ergeben sich, beispielsweise durch Oberflächeneffekte dieser Stoffe, Materialeigenschaften, die im Wesentlichen von deren Oberflächenbeschaffenheit sowie von Form und Größe der Nanostrukturen abhängen.

Eine wesentliche Herausforderung in der Entwicklung von Nanopartikeln und Nanoverbundmaterialien, als Nanokomposit-Materialien bezeichnet, stellt die Sicherstellung von Partikelgrößen und -formen, sowie deren Verteilung im umgebenden Matrix-Material dar. Diese Eigenschaften werden während des Produktionsprozesses aktiv beeinflusst, beispielsweise durch Scherkräfte in einem Dispergierextruder. Hierbei werden sowohl Partikelagglomerationen aufgebrochen, als auch einzelne Partikel zerteilt. Je nach Anwendung können diese Vorgänge beabsichtigt oder unerwünscht sein. So ist für ein elektrisch leitfähiges Polymer mit Kohlenstoffnanoröhren ein Netzwerk vereinzelter Nanoröhren notwendig, die dabei selbst mit möglichst großem Aspektverhältnis innerhalb des Materials vorliegen sollen, um die Bildung eines leitfähigen Netzwerks zu fördern. Die Prozesskontrolle ist konventionellerweise nur nachträglich möglich, indem einzelne Ausschnitte von wenigen hundert Mikrometern Größe mit elektronenmikroskopischen Verfahren untersucht werden. Das führt zu einer Vielzahl von Problemen, welche die insbesondere mittelständischen Hersteller von Spezialkunststoffen schwer bewältigen können: Einerseits ergibt sich durch aufwändige Laboruntersuchung, die oft außer Haus stattfindet, eine große Zeitverzögerung bei der Weiterentwicklung der Produktionsverfahren, andererseits liefern bildgebende Verfahren mit mikroskopischer Auflösung nur Informationen über die Materialbeschaffenheit eben jenes kleinen untersuchten Ausschnitts. Darüber hinaus unterscheidet sich die Größe

von Nanopartikeln und ihren Agglomeraten teilweise um mehrere Größenordnungen, was die Charakterisierung vor Herausforderungen stellt. Eine weitere große Hürde stellen die Investitions- und Unterhaltungskosten für ein spezialisiertes Materiallabor dar. Viele Hersteller verzichten daher auf mikroskopische Untersuchung und optimieren ihre Prozesse unter Beobachtung von makroskopischen Materialparametern. Eine tiefere Kenntnis der Nano- und Mikrostruktur wird dabei nicht erlangt, und weiteres Entwicklungspotential bleibt begrenzt.

Im Rahmen dieser Arbeit wird die Anwendung von optischer Kohärenztomographie (OCT) auf die Nanokomposit- und Nanopartikelcharakterisierung vorgestellt. OCT ist ein Verfahren zur dreidimensionalen Bildgebung mit mikroskopischer Auflösung. Mit einem typischen Messbereich von einigen Kubikmillimetern stellt OCT eine Erweiterung von Sonographie, Computertomographie und Magnetresonanztomographie in Richtung kleinerer Auflösungen und Messbereiche dar. OCT basiert auf einer Abtastung der Probe mit einem Laserstrahl und dem Überlagerungsempfang des von der Probe rückgestreuten Lichts. Übliche Anwendungsbereiche sind weitestgehend in der Medizintechnik zu finden, insbesondere in der Augenheilkunde.

Zur Charakterisierung von Nanokomposit-Materialien wird in dieser Arbeit ein multiskaliger Ansatz verfolgt. Während Partikel und Agglomerationen im Mikro- und Millimeterbereich bildgebend analysiert werden, ergänzt eine streumodell-basierte Auswertemethode die Analyse hin zu kleinsten Partikelgrößen im Nanometerbereich. In diesem Zusammenhang werden der Durchmesser und das Aspektverhältnis von sphärischen und zylinderförmigen Partikeln in homogen verteilten, monodispersen Partikelproben mit einer Genauigkeit von wenigen Nanometern analysiert und der Dispergierungszustand von Nanokompositen wird sowohl offline als auch inline, d.h. während des Produktionsvorgangs, bestimmt. Hierbei zeigt sich die Robustheit dieses Messverfahrens, welches in der Lage ist, hinreichend große Materialproben zu untersuchen, um zuverlässige Rückschlüsse auf die globalen Materialparameter zu erlauben. Weiterhin ist dieses zerstörungsfreie Verfahren für flüssige und feste Materialproben geeignet und kommt ohne Probenvorbereitung aus.

Für Anwendungen von OCT abseits der Medizintechnik ergeben sich andere Schwerpunkte: Auflösung, Empfindlichkeit und Messgeschwindigkeit werden ergänzt durch Anforderungen hinsichtlich Robustheit, geringen Systemkosten, Parallelisierbarkeit und kleiner Baugröße. Konventionelle freistrahl- oder faseroptische Systeme sind bauartbedingt limitiert bezüglich minimaler Größe und Kosten und benötigen eine exakte geometrische Justage und Einstellung der Polarisation. Temperaturschwankungen und Vibrationen verändern optische Kopplungseigenschaften und Polarisationszustände, weshalb OCT-Systeme derzeit oft in geschützten Umgebungen und von geschultem Personal zu bedienen sind.

Die photonische Integration von Kommunikations- und Messsystemen bietet robuste, günstige und kompakte Alternativen zu herkömmlichen Aufbauten. Durch photolithographische Herstellungsverfahren kann eine Vielzahl von Systemen gemeinsam auf einem Chip untergebracht werden. Im Rahmen dieser Arbeit werden siliziumphotonisch integrierte OCT-Systeme untersucht. Dort sind sowohl Interferometer als auch differentielle Photodetektoren auf einem gemeinsamen Chip untergebracht. In Systemcharakterisierungen wird gezeigt, dass bereits kleine Probenreflektivitäten von −64 dB detektierbar sind. Die integriert-optischen Systeme ermöglichen damit die Untersuchung von biologischen und technischen Proben.

Kapitel 1 führt in die Problemstellung ein, indem zunächst auf Nanomaterialien, deren Anwendungsgebiete und auf die Notwendigkeit von geeigneten Charakterisierungsverfahren eingegangen wird. Darauf folgend wird das OCT-Messprinzip eingeführt und schließlich werden die Möglichkeiten der Siliziumphotonik zur Integration von Messsystemen beschrieben.

Kapitel 2 geht auf die Grundlagen der OCT und der polarisationsauflösenden OCT ein. Dabei wird das Messsignal eines OCT-Systems mathematisch beschrieben und Systemeinflüsse auf Auflösung, Messbereich und Empfindlichkeit werden untersucht. Grundlagen der optischen Polarisation und von polarisationsempfindlichen OCT-Systemen werden vorgestellt und beschrieben.

Kapitel 3 stellt Ergebnisse von Experimenten in denen OCT zur multiskaligen Untersuchung von Nanokompositen verwendet wird vor. Dabei werden Nanopartikel und Partikelagglomerate in Größenordnungen von Nano- bis Millimetern untersucht. Große Strukturen werden klassisch bildgebend analysiert, während Nanopartikel mittels eines optischen Streumodells untersucht werden. Die entwickelte Messmethodik wird dabei sowohl in einer Laborumgebung als auch im Produktionsumfeld angewandt. Eine eigens entwickelte OCT-Messsonde erlaubt dabei Messungen während der Nanokomposit-Produktion.

Kapitel 4 beschreibt eine Erweiterung des in Kapitel 3 vorgestellten Streumodells auf Polarisationseffekte. Im Vergleich mit elektromagnetischen Streusimulationen wird mit polarisationsauflösender OCT gezeigt, dass neben der Partikelgröße auch die Form von Nanopartikeln bestimmt werden kann.

Kapitel 5 geht auf die siliziumphotonische Integration von OCT-Systemen ein. In diesem Zusammenhang werden zwei Systeme mit integriertem Interferometer und integrierten Photodioden vorgestellt. Die Systeme nutzen entweder einen internen oder einen externen Referenzpfad, wodurch unterschiedliche Abstände zwischen Chip und untersuchter Probe ermöglicht werden. Eine umfassende Analyse spezifischer Störsignalquellen zeigt, welche Aspekte beim Design integriert-photonischer Systeme besonders berücksichtigt werden müssen. Dreidimensionale Aufnahmen von biologischen und technischen Objekten belegen die Funktionalität der Systeme.

Kapitel 6 fasst die Ergebnisse dieser Arbeit zusammen und gibt einen Ausblick auf zukünftige Entwicklungen.

Die im Rahmen dieser Arbeit entstandenen Ergebnisse wurden in mehreren wissenschaftlichen Fachzeitschriften publiziert sowie auf internationalen Konferenzen vorgetragen. Eine Auflistung aller Veröffentlichungen ist auf Seite 181 ff. zu finden.

Preface

Nanocomposite materials consist of a host material and a nanoscale filler material and play an increasingly important role in various fields of applications, reaching from medical diagnostics and therapy to industrial applications and everyday necessities. The attractiveness of nanomaterials arises from their unique physical properties, which go beyond those of classical materials. Surface effects, for instance, lead to material properties, which depend essentially on the nanostructure of the surface.

A major challenge in the development of nanoparticles and nanocomposite materials is to achieve the desired particle sizes and shapes, and the dispersion in the host material. These properties are actively influenced during the production process, e.g., by application of shear forces in a compounding extruder. Thereby, particle agglomerates are split, and single particles are fractured or separated. Depending on the application, these processes are either intended or unwanted. In the case of, e.g., an electrically conductive polymer with carbon nanotubes, a network of dispersed nanotubes is necessary, while the single tubes preferably keep their large aspect ratio and thus enable the formation of a conductive mesh. Process control is only possible afterwards, using an electron microscope for the inspection of small sample details with few hundred micrometres in size. This leads to a couple of problems, which represent challenges, especially for small and medium-sized enterprises: On the one hand, elaborate laboratory characterization, which often takes place off-site, increases the duration of process development. On the other hand, microscopic imaging methods only provide information on the small analysed spot. In addition, the size of nanoparticles and their agglomerates differs by orders of magnitude, which is a problem for many characterization methods. A further obstacle is the high investment and maintenance cost of a specialized material laboratory. For this reason, many manufacturers go without microscopic characterization and optimize their processes instead with respect to macroscopic material properties. A deeper insight into the nano- and microstructure is not obtained, and future potential for material development is thus limited.

In this work, the application of optical coherence tomography (OCT) for nanocomposite and nanoparticle characterization is investigated. OCT is a three-dimensional imaging method with microscopic resolution. Having a typical imaging range of a few cubic millimetres, OCT complements ultrasonic, X-ray computed tomographic, and magnetic resonance tomographic techniques with respect to higher resolution. OCT relies on scanning the sample with a laser beam and on interferometrically detecting the light backscattered from the sample. Typical applications are to be found in medical diagnostics, especially in ophthalmology.

For the characterization of nanocomposites, a multi-scale approach is pursued. While particles and agglomerates in the micrometre and millimetre regime are analysed based on images, an analysis method relying on a dedicated light scattering model extends the range of measurable particle sizes towards nanoparticles. With this technique, diameter and aspect ratio of spherical and cylindrical particles in homogeneous monodisperse samples are analysed with nanometre accuracy. Further, the dispersion state of nanocomposites is characterized both off-line and in-line during the production process. In this context, the robustness of the measurement principle becomes apparent, as large sample volumes can be analysed, and conclusions on global material parameters are possible. This non-destructive measurement principle proves to be suitable for liquid and solid materials and does not need any sample preparation.

Industrial applications pose new challenges to OCT systems that differ from those of medical applications: Resolution, sensitivity and imaging speed are complemented by requirements with respect to robustness, small system cost, parallelization and small system size. Conventional free-space or fibre-optic systems are bulky and expensive and need exact optical alignment. However, temperature changes and vibrations change optical coupling properties and polarization states, and this is the reason why current OCT systems often have to be operated in protected environments and by skilled personnel.

Photonic integrated systems in communication and measurement technologies offer robust, cheap and compact alternatives to traditional setups. Photolithographic production methods allow a dense integration of a multitude of

systems together on a single chip. In this work, silicon photonic integrated OCT systems are investigated. These systems comprise interferometer and balanced photodetectors integrated on a common chip. System characterizations show a sensitivity to even weak sample reflections of only −64 dB. As an application example, we examine biological and technical samples.

Chapter 1 begins with a description of the problem by introducing nanomaterials, their applications and the need for characterization techniques. This is followed by an introduction into the measurement principle of OCT. Further, the silicon photonics platform for system integration and miniaturization is presented.

Chapter 2 expands on the fundamentals of OCT and polarization-sensitive OCT. An analytic expression of an OCT signal is deduced from scalar electric field equations. System influences on resolution, measurement range and sensitivity are investigated. Basics of optical field polarization are presented, and concepts for polarization-sensitive OCT systems are shown.

Chapter 3 presents the application of multi-scale OCT for characterizing nanocomposite materials. Nanoparticles and particle agglomerates are analysed, with sizes ranging from nanometres to millimetres. Large structures are analysed classically by OCT imaging, while nanoparticles are characterized by application of a dedicated optical scattering model to the measured backscatter data. The measurement technique is applied both in laboratory and production environments. A specifically developed OCT probe enables in-line measurements during the nanocomposite production process.

Chapter 4 extends the optical scattering model from Chapter 3 towards polarization effects. Comparison of electromagnetic scattering simulations and polarization-sensitive OCT measurements show that along with the size of the nanoparticles also their shape can be inferred.

Chapter 5 describes the silicon photonic integration of OCT systems. In this context, two systems are presented, both having interferometers and balanced photodetectors integrated on a single chip. One system uses an internal integrated reference path, while the reference path of the other system is external

to the chip. This enables measurements at different distances of the sample from the photonic chip. A comprehensive analysis of specific signal artefacts reveals challenges that require special attention when designing integrated OCT systems. Three-dimensional images of biological and technical objects confirm the functionality of the systems.

Chapter 6 summarizes the results of this work and outlines possible future developments.

The results obtained in this work have been published in peer-reviewed scientific journals and at international conferences. A full list of publications is found from page 181 onwards.

Achievements of the present work

In this thesis, optical coherence tomography (OCT) systems are developed and applied to nanocomposite and nanoparticle analysis. This comprises fibre-optic swept-source OCT, both of conventional and polarization-sensitive type, as well as integrated silicon photonic systems. The material analysis aims at nanoparticles and nanocomposite materials and pursues both traditional image-based methods and scattering-model-based analysis. A summary of the main achievements within this work is presented in the following.

Polarization-sensitive optical coherence tomography system

Setup of a fibre-optic polarization-sensitive swept-source optical coherence tomography (OCT) system and development of a mathematical model for polarization calibration.

Light scattering model

Development of a dedicated light scattering model, which allows the analysis of nanoparticles with OCT. This model enables fast and reliable characterization of scatterers beyond the diffraction limit [P2, P3, P5].

Nanocomposite dispersion state analysis

Using OCT, nanocomposites are characterized with respect to their dispersion state. This comprises image-based size and shape analysis of particle agglomerates inside the volume of a sample, and scattering-model-based analysis on the nanometre scale [P2, P6].

In-line process monitoring

Application of the OCT system with a dedicated probe at a nanocomposite compounding extruder pilot line. The in-line measurement allows for the first time real-time inspection of the nanocomposite production process using OCT [P2].

Size and shape determination of nanoparticles

From measurements with the OCT system, and with the help of Mie's scattering theory, diameters of spherical nanoparticles in monodisperse samples are determined with an accuracy in the nanometre regime [P2, P3, P5]. Polarization-sensitive OCT measurements of gold nanorods are compared to a number of numerical scattering simulations, and both diameter and aspect ratio of the nanorods are determined in good agreement with the nominal values.

Silicon photonic optical coherence tomography

Demonstration of the first fully integrated silicon photonic optical coherence tomography system. This comprises an interferometer, an optional reference path and a balanced photodetector. The swept-source laser is external to the chip. Proof-of-principle measurements of biological tissue and non-biological samples are shown. For robust broadband fibre-chip coupling of multiple parallel fibres, polymer lenses are fabricated at the edge of the silicon chip, using 3D laser printing [P1, P4, P7-10].

1 Introduction

Optical coherence tomography (OCT) is a measurement technique for three-dimensional volumetric imaging of samples. Its high measurement speed makes imaging possible, and resolution in the micrometre regime can replace biopsies in histological tissue examinations. OCT relies on low-coherence interferometry, which shares the fundamental measurement principle: Obtaining depth information of a scattering or reflecting object by means of a broadband phase-sensitive interferometric evaluation of the backscattered light. Time-domain OCT (TD-OCT) systems make use of the short coherence length of spectrally broadband light. By varying the length of the reference path, the measured layer inside the sample is selected by looking at the cross-correlation peak of the reference and the sample field. Fourier-domain systems, as compared to TD-OCT, observe the interference signal as a function of optical frequency. For this purpose, either the emission wavelength of the laser is tuned over time, or the detection of a scattered broadband source takes place with a spectrometer. A general advantage of all OCT systems is the inherent signal-to-noise outperformance compared to direct detection techniques, where, in contrast, the backscattered light power is measured directly on a photodiode: In OCT, the backscattered light interferes with a relatively strong reference field, which leads to a strong beat signal. The detection principle makes the measurement of samples with reflectivities below −100 dB with respect to the incident light power possible. This allows the analysis of weakly scattering samples like low-index contrast biologic tissues, or strongly absorbing or scattering samples, where the signal strength decays significantly with increasing depth.

First reported by Huang *et al.* [1], OCT gained importance in medical applications, like ophthalmology [2,3], dermatology [4], endoscopy [5], or in cardiovascular imaging [6]. In these fields, OCT complements the conventional imaging techniques, like ultrasonic imaging, magnetic resonance tomography, or X-ray computed tomography. OCT increasingly replaces invasive histological examinations, and assists minimally invasive surgery. In ophthalmology,

which is still the most important application field of OCT, the examination of the eye is accompanied by OCT images of the anterior eye [7]. Due to light absorption of water for wavelengths larger than 1 µm inside the vitreous humour of the eye, wavelengths around 850 nm are applied for posterior eye imaging [8].

1.1 Nanomaterials

The emerging multi-billion dollar market of nanomaterials is driven by a huge variety of applications ranging from medical diagnostics and therapy [9] to mechanical and civil engineering to energy storage and life sciences. This includes the investigation of nanocomposite polymers with enhanced mechanical or electronic properties [10,11], functional coatings [12], and anode materials for lithium-ion batteries [13]. Beyond that, nanoparticles are attractive for scientific examinations. Their size is in or below the range of the optical wavelength, and their surface-to-volume ratio is large. In contrast to bulk materials, size and shape of the particles govern their physical properties. Thus, the nano-size dimensions and the distinct particle shapes become the essential parameters in achieving specific material characteristics. For example, gold nanoparticles as chemical catalysts show a significant reaction-rate-dependence on their size and shape [14], and also the cellular uptake of gold nanorods into biological tissue, when used as imaging markers, turns out to be shape- and size-dependent [9]. Figure 1.1 shows electron-microscopic images of various nanoparticles. Multi-wall carbon nanotubes (MWCNT) are depicted in Figure 1.1 (a) and (b) in dispersed and agglomerated form. Nanospheres with defined size are shown in Figure 1.1 (c). Due to their spherical shape, their light scattering properties are well described by Mie's scattering theory. Gold nanorods in Figure 1.1 (d) are an interesting class of nanoparticles, because their shape-dependent plasmonic resonances allow wavelength-selective excitation, which can be exploited for instance in tumour therapy [15].

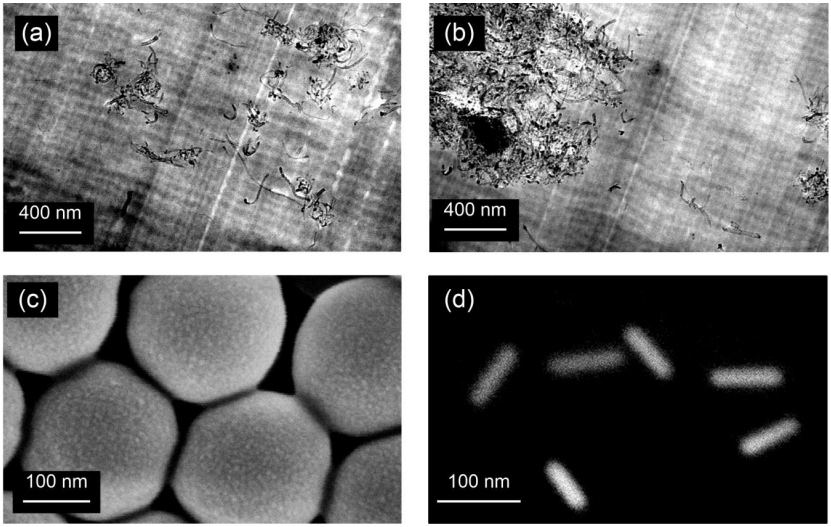

Figure 1.1: Electron-microscopic views of nanoparticles: (a, b) Multi-wall carbon nanotubes (MWCNT) dispersed (a) and agglomerated (b). The tubes form agglomerates because of their relatively strong adhesive forces and their curly shape. The spatial separation of the individual nanoparticles is a key challenge in nanocomposite engineering. (c) Polystyrene nanospheres as used as particle size standard and Mie scatterer. (d) Gold nanorods with well-defined aspect ratios.

Widespread industrial application of nanomaterials is still limited by the lack of adequate analysis tools. In particular, achieving and maintaining a well-dispersed particle distribution in nanocomposites is difficult without in-line or at least on-line analysis methods for process control. In-line methods analyse the main stream of the product material directly during production, and on-line methods analyse a continuously taken sample stream. Nevertheless, size and shape characterization of various types of nanoparticles mainly relies on microscopic imaging [16,17]. Optical or electron microscopy [18–20] need laborious, costly sample preparation and do not permit fast extraction of nanoscale structural information from statistically relevant sample volumes. Light scattering techniques, in contrast to imaging methods, are viable tools for determining particle size distributions from large sample volumes. Static light

scattering (SLS) uses angle-resolved and/or spectrally resolved detection of scattered light [21,22] and needs a rather complex optical setup, when large scattering angles are to be taken into account. Furthermore, surface reflections can distort the measurement. Dynamic light scattering (DLS) methods make use of temporal fluctuations of interference patterns of scattered light to calculate the hydrodynamic diameter of particles within the respective solvent [23]. Relying on the Brownian motion of the particles in liquid media, this technique is not applicable to solid samples. Both SLS and DLS preferentially provide information on particle size, while particle shape cannot be determined [24]. Particle size distributions can also be measured using centrifugal sedimentation techniques, where particles with different dimension are separated by differences in their sedimentation speed in presence of centrifugal forces [25]. While this technique is applicable to a broad size range, high experimental effort is necessary, only liquid samples can be analyzed, and no information on particle shape is obtained.

None of the aforementioned techniques can meet the requirements associated with industrial process development and quality control, where robustness of the measurement method, fast analysis and the capability to characterize representative sample volumes without laborious sample preparation are key. In addition, for in-line process control, good mechanical and thermal robustness of the measurement system are important, as well as the possibility to integrate the measurement system into the processing line.

In contrast to the established measurement techniques, optical coherence tomography (OCT) provides three-dimensional imaging data from a bulk sample without the need for expensive sample preparation. In the following, we show that OCT represents an attractive tool for fast and robust nanomaterial characterization and that the technique can be applied to a wide range of particle and agglomerate sizes both on the micrometre and on the nanometre scale. Using a theoretical model of light scattering in the sample, this work demonstrates accurate determination of diameter and aspect ratio of particles in homogeneous monodisperse samples. Particle agglomerates with sizes of up to hundreds of micrometres are detected by applying image processing techniques to the OCT

data. Both, the scattering-model-based method and the image-based method can be performed *in situ*, without prior sample preparation, in both liquid and solid materials, and are applicable to laboratory investigations as well as to in-line process control in industrial production.

1.2 Measurement principle of OCT

The three-dimensional measurement principle of OCT relies on scanning a thin laser beam transversely over the sample with a diffraction-limited lateral resolution (*x*, *y* dimension). Simultaneously, the depth-dependent amplitude backscattering profile $r_s(z)$ of the sample is recorded. Resolution in depth (axial resolution, *z*-dimension) is achieved by measurement and evaluation of the broadband interference of backscattered light from the sample with light reflected from a reference target. Figure 1.2 shows the measurement concept as an example for a time-domain OCT system: Light from a light source, covering a broad wavelength range, is split by a beam splitter into two parts, which travel along the sample and the reference path. Inside the sample, light is scattered back at different depths, according to the amplitude backscattering profile $r_s(z) = \sqrt{R_s(z)}$ of the sample. The part travelling along the reference path is reflected by a mirror. At the beam splitter, the backscattered light from the sample and the backreflected light from the reference mirror are superimposed, and the photodetector measures an interference pattern, depending on the length difference $z_r - z_s$ of the reference mirror position and the position of the respective sample reflection. In a time-domain OCT system, the coherence length, see Appendix A.6, of the light is small, such that only sample reflections from the layer with same optical distance to the beam splitter as the reference mirror are correlated with each other and generate an interference signal. The photocurrent is recorded by an analogue-to-digital converter for different positions z_r of the reference mirror.

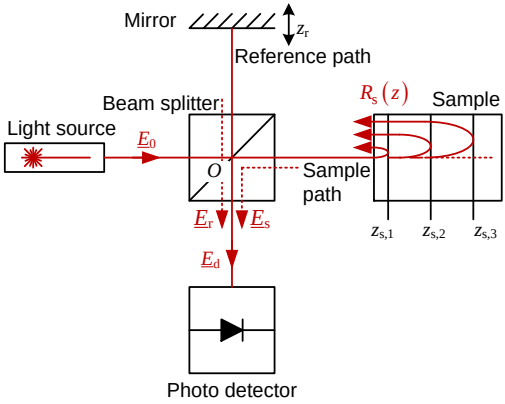

Figure 1.2: Interferometric measurement principle of time-domain optical coherence tomography (TD-OCT): A light source emits light (electric field $\underline{E}_0$) over a wide optical spectrum. The optical power is split at the beam splitter and a first part is sent to a reference path whereas a second part is sent to a sample path. Depending on the sample structure, light (electric field $\underline{E}_s$) is scattered back from different depths of the sample, here, $z_{s,1}$, $z_{s,2}$, $z_{s,3}$, measured relative to the beam splitter centre O with $z_O = 0$, and interferes with the beam (electric field $\underline{E}_r$) from the reference mirror at position z_r. The photodetector receives the electric field $\underline{E}_d$ and measures the interferogram obtained by scanning the position of the reference mirror, which contains information on the backscattering profile $R_s(z)$ of the sample.

Generally, time-domain OCT (TD-OCT) is distinguished from Fourier-domain OCT (FD-OCT), which differs in the way it measures the depth-dependent backscattering profile: The Fourier relation of the autocorrelation function of a signal and its optical power spectral density is known as the Wiener-Khintchine theorem [26]. An analogue relation holds for the TD-OCT interference signal, which is the cross correlation of the fields returning from sample and reference path and which is linked by a Fourier relation to the optical cross power spectral density. Thus, it is possible to investigate the complex backscattering factor of the sample in frequency domain, using a spectrally resolved detection of the interference signal, rather than in time-domain with a moving mirror.

The spectrally resolved detection of the interference signal can be performed in two ways: A first type is referred to as spectral-domain OCT (SD-OCT) [27], where a broadband light source is used for illumination of sample and reference path, and the frequency-resolved detection of the interference signal is accomplished by a spectrometer, see Figure 1.3 (a). A second type is called swept-source OCT (SS-OCT) [28], where a narrow-band laser source is tuned in frequency over a broad frequency range and thereby probes the sample with various frequencies, see Figure 1.3 (b).

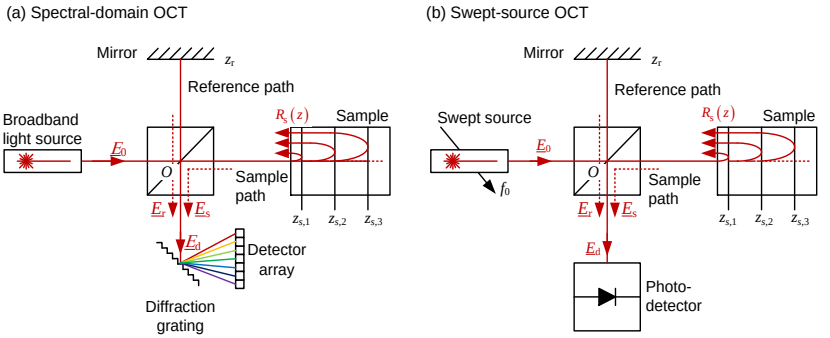

Figure 1.3: Spectral-domain and swept-source OCT, (a), (b), respectively. Both systems evaluate the interference signal of the light backscattered from the sample and the light of the reference path resolved in optical frequency and do not need a scanning reference mirror. (a) SD-OCT operates with a broadband light source and uses a spectrometer for spectrally resolved detection of the interference signal, here illustrated by a diffraction grating and a detector array. (b) SS-OCT relies on a swept-laser source, which scans its optical frequency rapidly over time, as well as a photodetector for detection.

As time-domain OCT systems can be built up with conventional opto-mechanical components and a broadband light source, it is regarded to be the simplest OCT configuration. For this purpose, most practical systems use specially developed and fast moveable optical delay lines for scanning the reference path length.

However, with rising scanning speed, the mechanical effort to build robust fast moveable components increases and the averaging time in the detector

decreases, which leads to a decrease in signal-to-noise ratio (SNR). Typically, TD-OCT systems run at depth-scan repetition rates in the low kHz range and are able to detect power reflection levels of around −110 dB with respect to the optical power incident on the sample [29]. The low scanning speed is, e.g., a major problem in biomedical OCT applications, since fast and involuntary movements of the imaged object, e.g. the human eye, disturb the measurement.

Both FD-OCT types, SD-OCT and SS-OCT, avoid mechanically movable parts, but require more advanced optical instrumentation as compared to TD-OCT, since spectrometers or swept-source lasers are necessary. FD-OCT further needs more data processing effort for inverse Fourier transform of the measurement signal, but offers higher operation speed, and higher sensitivity, which means a lower minimum detectable sample reflectivity level. The sensitivity advantage is inherent [30,31], since the Fourier transform reduces the noise level by spectral filtering. These systems are able to reach shot-noise limited performance and can detect around −120 dB sample reflectivity. Further, without need for mechanically scanned delay lines, much higher scanning speeds become possible: Choi *et al.* showed a 10 MHz depth-scan repetition rate with an SD-OCT system and Wieser, Klein *et al.* demonstrated SS-OCT systems operating at repetition rates between 3.2 MHz and 20 MHz [32–34].

1.3 Silicon photonics

While conventional OCT systems are predominantly built from discrete components, photonic integration facilitates compact systems that stand out due to robustness and that lend themselves to cost-efficient mass production. Especially in endoscopic applications as well as in industrial surface and distance metrology, integrated systems can comply with the demands in size, mechanical robustness, temperature stability and cost.

Silicon as the basis for photonic integrated circuits (PIC) gained attention as it proves to be a material platform, which allows the reuse of CMOS fabrication

infrastructure. A plurality of foundry services has emerged within the last decade [35–37], primarily driven by applications in optical communications. The foundries offer process design kits (PDK) with libraries of standardized silicon photonic devices such as passive components, electro-optic modulators, and germanium-based photodetectors.

Other material platforms, e.g., based on III-V material systems, inherently contain active materials for laser-source co-integration. Nevertheless, the low-cost and high-yield process flow in silicon photonic fabrication is an important advantage when aiming at large-scale photonic integrated systems.

Besides compatibility to CMOS fabrication lines, large-scale and inexpensive system-on-chip co-integration of photonics and electronics becomes possible [38]. Figure 1.4 shows a schematic cross-sectional drawing of a silicon-on-insulator (SOI) chip with passive photonic and active electro-optic components.

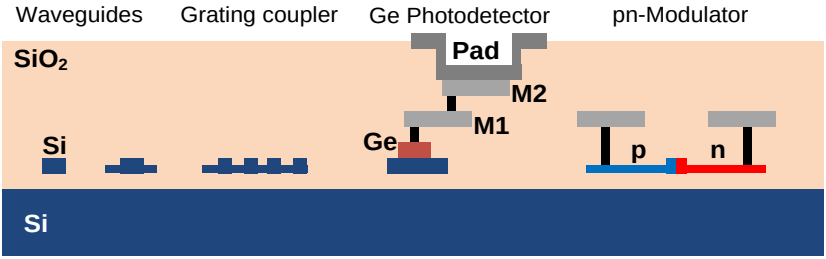

Figure 1.4: Schematic cross section of a silicon photonic chip, including passive optical components and active electro-optical components. The silicon-on-insulator (SOI) wafer with functional silicon (Si), germanium (Ge), metal (M1, M2) layers and p-, n-doped silicon allows, among others, the co-integration of waveguides, grating couplers, photodetectors and modulators.

2 Fundamentals

This chapter provides the theoretical background of optical coherence tomography (OCT) including a theoretical treatment on OCT signal calculation. Building on this, relations for achievable resolution and sensitivity are formulated, which arise from technical limitations in wavelength range, lens aperture, scanning speed and noise of available components. A section on sensitivity analysis compiles influences of different noise sources and suggests operating parameters for optimum OCT performance.

In a section comprising fundamentals on optical polarization, polarization-sensitive OCT (PS-OCT) is introduced, together with PS-OCT variations and applications thereof. Further, the individual PS-OCT setup built in the course of this work is presented, which is used for the polarization-resolved measurements shown in Chapter 4.

2.1 Optical coherence tomography

In this chapter, the signal obtained from an OCT measurement is derived analytically. The emphasis is on the calculation of the depth-dependent backscattering signal, which is the central element of OCT theory. Information on lateral resolution can be found in Section 2.1.2.

The signal calculation can either be performed in the time-domain [39,40] or in the frequency-domain [41]. In the following, the signals and fields are derived in time-domain, starting from the electric-field impulse responses of the sample and of the reference path, and convolving them with the time-dependent source field. Superposition of the fields from sample and reference path leads to interference. The resulting intensity is detected by a photodetector and is described with the help of coherence functions. These allow the analysis of the depth resolution and the measurement range. The results of this calculation are applied to TD-OCT and, using Fourier-transform, to the FD-OCT types SS-OCT and SD-OCT.

Complementing these considerations related to depth resolution, Section 2.1.2 is dedicated to lateral resolution and focal measurement range, which both relate to the optical beam properties.

In addition, the effect of sampling is addressed in Section 2.1.3, together with properties of the discrete Fourier transform, since the OCT signal is processed in the digital domain.

Finally, in Section 2.1.4 the sensitivity of an OCT measurement, describing the minimum measurable sample reflectivity, is derived from the noise contributions of the individual system components. The concept of balanced detection for sensitivity improvement is introduced, and the dependence of the sensitivity on reference and sample arm power is derived. Optimum operating points for different measurement tasks are suggested.

2.1.1 OCT signal calculation

The light source in OCT, see Figure 1.2 and Figure 1.3, can be described by the time-dependent electric field of the emitted light, which is considered to be a plane wave and which can be represented by the complex scalar electric field

$$\underline{E}_0(t) = \underline{A}_0(t)\mathrm{e}^{\mathrm{j}\omega_0 t}. \tag{2.1}$$

In this relation, $\underline{A}_0(t)$ is the complex slowly-varying random amplitude, t the time and $\omega_0 = 2\pi f_0$ the optical angular carrier frequency of the source with carrier frequency f_0. In the case of a SS-OCT system, the optical angular frequency is additionally varied over time. The light is split up by the beam splitter at position O with $z_O = 0$ on the distance axis z, which describes the distance of a reflection with respect to the beam splitter location. In the following, this axis is also referred to as the depth axis. In both sample and reference path, light is scattered and reflected back, which can be described by the corresponding field reflectivity profiles $r_\mathrm{s}(z) = \sqrt{R_\mathrm{s}(z)}$, $r_\mathrm{r}(z) = \sqrt{R_\mathrm{r}(z)}$. The reference-path reflectivity profile is given by a δ-function, see Appendix A.4 for a mathematical definition of the δ-function, with field reflectivity r_R at the depth of the mirror position z_r,

$$r_\mathrm{r}(z) = r_\mathrm{R}\ \delta(z - z_\mathrm{r})\ . \tag{2.2}$$

The field impulse responses of sample and reference path describe their temporal back reflection behaviour and are derived from the field reflectivity profiles using the respective speed of light in sample and reference path, $v_\mathrm{s} = c_0 n_\mathrm{s}$, $v_\mathrm{r} = c_0 n_\mathrm{r}$, with the vacuum speed of light c_0 and the effective refractive indices n_s, n_r. For simplicity, we assume the effective refractive indices n_s and n_r to be constant along z in the following. The depth positions $z = \left(v_{\mathrm{s,\,r}}/2\right) t_{\mathrm{s,\,r}}$ correspond to round trip times $t_{\mathrm{s,\,r}}$, where the factor of 1/2 accounts for forward and backward propagation in sample and reference path, respectively. The field impulse responses of sample and reference path thus are given by

$$\begin{aligned} h_\mathrm{s}(t_\mathrm{s}) &= r_\mathrm{s}\left(\frac{v_\mathrm{s}}{2} t_\mathrm{s}\right)\frac{v_\mathrm{s}}{2}, \\ h_\mathrm{r}(t_\mathrm{r}) &= r_\mathrm{r}\left(\frac{v_\mathrm{r}}{2} t_\mathrm{r}\right)\frac{v_\mathrm{r}}{2}. \end{aligned} \tag{2.3}$$

The factor of $\mathrm{d}z/\mathrm{d}t = v_{\mathrm{s,r}}/2$ accounts for the conversion of a reflectivity per depth to a reflectivity per time. With Eq. (2.2), the return time τ_r corresponding to the reference mirror in the reference path, and $z_\mathrm{r} = (v_\mathrm{r}/2)\tau_\mathrm{r}$, the impulse response of the reference path results in

$$\begin{aligned} h_\mathrm{r}(t_\mathrm{r}) &= r_\mathrm{R}\ \delta\left(\frac{v_\mathrm{r}}{2}(t_\mathrm{r} - \tau_\mathrm{r})\right)\frac{v_\mathrm{r}}{2} \\ &= r_\mathrm{R}\ \frac{\delta\left((t_\mathrm{r} - \tau_\mathrm{r})\right)}{\left|\frac{v_\mathrm{r}}{2}\right|}\frac{v_\mathrm{r}}{2} \\ &= r_\mathrm{R}\ \delta(t_\mathrm{r} - \tau_\mathrm{r}). \end{aligned} \tag{2.4}$$

The fields returning from sample and reference path can be calculated by a convolution of the incident fields with the impulse responses. The electric fields returning from sample and reference path are denoted as $\underline{E}_\mathrm{s}$ and $\underline{E}_\mathrm{r}$, respectively, and considered in front of the detector in the detection path, see Figure 1.2. Each of the fields is once reflected at the beam splitter with a field

reflection factor of $\mathrm{j}/\sqrt{2}$ and once transmitted through the beam splitter with a field transmission factor of $1/\sqrt{2}$. This leads to a total factor of j/2 for both of the fields,

$$\begin{aligned}\underline{E}_\mathrm{s}(t) &= \frac{\mathrm{j}}{2}\,\underline{E}_0(t) * h_\mathrm{s}(t_\mathrm{s}),\\ \underline{E}_\mathrm{r}(t) &= \frac{\mathrm{j}}{2}\,\underline{E}_0(t) * h_\mathrm{r}(t_\mathrm{r}),\end{aligned} \tag{2.5}$$

where * denotes a convolution in the time domain, see Appendix A.3. Eqs. (2.5) can be expressed as

$$\begin{aligned}\underline{E}_\mathrm{s}(t) &= \frac{\mathrm{j}}{2}\int_{-\infty}^{+\infty} h_\mathrm{s}(t_\mathrm{s})\,\underline{A}_0(t-t_\mathrm{s})\,\mathrm{e}^{\mathrm{j}\omega_0(t-t_\mathrm{s})}\mathrm{d}t_\mathrm{s}\\ &= \frac{\mathrm{j}}{2}\int_{-\infty}^{+\infty} r_\mathrm{s}\left(\frac{v_s}{2}t_\mathrm{s}\right)\frac{v_\mathrm{s}}{2}\,\underline{A}_0(t-t_\mathrm{s})\,\mathrm{e}^{\mathrm{j}\omega_0(t-t_\mathrm{s})}\mathrm{d}t_\mathrm{s},\\ \underline{E}_\mathrm{r}(t) &= \frac{\mathrm{j}}{2}\int_{-\infty}^{+\infty} h_\mathrm{r}(t_\mathrm{r})\,\underline{A}_0(t-t_\mathrm{r})\,\mathrm{e}^{\mathrm{j}\omega_0(t-t_\mathrm{r})}\mathrm{d}t_\mathrm{r}\\ &= \frac{\mathrm{j}}{2}\mathrm{r}_\mathrm{R}\,\underline{A}_0(t-\tau_\mathrm{r})\,\mathrm{e}^{\mathrm{j}\omega_0(t-\tau_\mathrm{r})}.\end{aligned} \tag{2.6}$$

In these equations, the effect of sample and reference on the electric field becomes visible: The amplitude is scattered back with factor of r_R or $r_\mathrm{s}\left((v_\mathrm{s}/2)t_\mathrm{s}\right)$ along with a phase shift $-\omega_0\tau_\mathrm{r}$ or $-\omega_0 t_\mathrm{s}$. The variables $t_\mathrm{s}, t_\mathrm{r}$ denote the respective return times from sample path and reference path.

Both fields from sample and reference path superimpose on the photodetector, which generates a photocurrent proportional to the averaged squared absolute value of the complex electric field

$$\begin{aligned}\overline{\left|\underline{E}_\mathrm{d}\right|^2} &= \overline{\left|\underline{E}_\mathrm{s}+\underline{E}_\mathrm{r}\right|^2}\\ &= \overline{\left|\underline{E}_\mathrm{s}\right|^2} + \overline{\left|\underline{E}_\mathrm{r}\right|^2} + 2\,\mathrm{Re}\left\{\overline{\underline{E}_\mathrm{s}\underline{E}_\mathrm{r}^*}\right\}.\end{aligned} \tag{2.7}$$

This average is a time average, and we assume that the fields are described by ergodic processes, see Appendix A.6. The square leads to mixing terms, of

which the sample-reference mixing term contains the depth-dependent scattering information of the sample. In the following, all terms are evaluated separately, starting with the sample-reference mixing term, which is the actual OCT signal.

With Eq. (2.6) the sample-reference mixing term is given by

$$\begin{aligned} & 2\,\mathrm{Re}\left\{\overline{\underline{E}_\mathrm{s}\underline{E}_\mathrm{r}^*}\right\} \\ &= \frac{1}{2} r_\mathrm{R}\,\mathrm{Re}\left\{\overline{\int_{-\infty}^{+\infty} h_\mathrm{s}(t_\mathrm{s})\underline{A}_0(t-t_\mathrm{s})\mathrm{e}^{\mathrm{j}\omega_0(t-t_\mathrm{s})}\underline{A}_0^*(t-\tau_\mathrm{r})\mathrm{e}^{-\mathrm{j}\omega_0(t-\tau_\mathrm{r})}\mathrm{d}t_\mathrm{s}}\right\} \\ &= \frac{1}{2} r_\mathrm{R}\,\mathrm{Re}\left\{\int_{-\infty}^{+\infty} h_\mathrm{s}(t_\mathrm{s})\overline{\underline{A}_0(t-t_\mathrm{s})\underline{A}_0^*(t-\tau_\mathrm{r})\mathrm{e}^{\mathrm{j}\omega_0(\tau_\mathrm{r}-t_\mathrm{s})}}\mathrm{d}t_\mathrm{s}\right\}. \end{aligned} \tag{2.8}$$

The integrand contains a correlation of two fields with temporal distance $\tau_\mathrm{r}-t_\mathrm{s}$ and can thus by expressed in terms of a complex coherence function, see Appendix A.6,

$$\underline{\Gamma}_\mathrm{L}(\tau_\mathrm{r}-t_\mathrm{s}) = \overline{\underline{A}_0(t-t_\mathrm{s})\underline{A}_0^*(t-\tau_\mathrm{r})}\,\mathrm{e}^{\mathrm{j}\omega_0(\tau_\mathrm{r}-t_\mathrm{s})}\ , \tag{2.9}$$

resulting in

$$2\,\mathrm{Re}\left\{\overline{\underline{E}_\mathrm{s}\underline{E}_\mathrm{r}^*}\right\} = \frac{1}{2} r_\mathrm{R}\int_{-\infty}^{+\infty} h_\mathrm{s}(t_\mathrm{s})\,\mathrm{Re}\left\{\underline{\Gamma}_\mathrm{L}(\tau_\mathrm{r}-t_\mathrm{s})\right\}\mathrm{d}t_\mathrm{s}. \tag{2.10}$$

This term can be rephrased using the real-valued coherence function

$$K_\mathrm{L}(\tau_\mathrm{r}-t_\mathrm{s}) = \frac{1}{2}\mathrm{Re}\left\{\underline{\Gamma}_\mathrm{L}(\tau_\mathrm{r}-t_\mathrm{s})\right\} \tag{2.11}$$

leading to

$$2\,\mathrm{Re}\left\{\overline{\underline{E}_\mathrm{s}\underline{E}_\mathrm{r}^*}\right\} = r_\mathrm{R}\int_{-\infty}^{+\infty} h_\mathrm{s}(t_\mathrm{s})K_\mathrm{L}(\tau_\mathrm{r}-t_\mathrm{s})\,\mathrm{d}t_\mathrm{s}. \tag{2.12}$$

The real-valued coherence function can be expressed by the normalized real-valued coherence function $k_\mathrm{L}(\tau_\mathrm{r}-t_\mathrm{s}) = K_\mathrm{L}(\tau_\mathrm{r}-t_\mathrm{s})/K_\mathrm{L}(0)$, with

$K_{\mathrm{L}}(0)=\overline{|\underline{A}_0(t)|^2}$. In the case of quasi-monochromatic sources ($f_0 \gg \delta f$), where the instantaneous source bandwidth δf is significantly smaller than the carrier frequency, which is typically valid for OCT light sources, the coherence function can be split up in a baseband coherence function $\kappa_{\mathrm{L}}(\tau)$ and a harmonic term,

$$\begin{aligned} K_{\mathrm{L}}(\tau_{\mathrm{r}}-t_{\mathrm{s}}) &= K_{\mathrm{L}}(0)k_{\mathrm{L}}(\tau_{\mathrm{r}}-t_{\mathrm{s}}) \\ &= K_{\mathrm{L}}(0)\kappa_{\mathrm{L}}(\tau_{\mathrm{r}}-t_{\mathrm{s}})\cos\left(\omega_0(\tau_{\mathrm{r}}-t_{\mathrm{s}})\right). \end{aligned} \tag{2.13}$$

Hence, the sample-reference interference term is expressed as

$$\begin{aligned} & 2\,\mathrm{Re}\left\{\overline{\underline{E}_{\mathrm{s}}\underline{E}_{\mathrm{r}}^{*}}\right\} \\ &= K_{\mathrm{L}}(0)r_{\mathrm{R}}\int_{-\infty}^{+\infty} h_{\mathrm{s}}(t_{\mathrm{s}})\kappa_{\mathrm{L}}(\tau_{\mathrm{r}}-t_{\mathrm{s}})\cos\left(\omega_0(\tau_{\mathrm{r}}-t_{\mathrm{s}})\right)\mathrm{d}t_{\mathrm{s}} \\ &= \overline{|\underline{A}_0(t)|^2}\,r_{\mathrm{R}}\int_{-\infty}^{+\infty} r_{\mathrm{s}}\left(\frac{v_{\mathrm{s}}}{2}t_{\mathrm{s}}\right)\frac{v_{\mathrm{s}}}{2}\kappa_{\mathrm{L}}(\tau_{\mathrm{r}}-t_{\mathrm{s}})\cos\left(\omega_0(\tau_{\mathrm{r}}-t_{\mathrm{s}})\right)\mathrm{d}t_{\mathrm{s}}. \end{aligned} \tag{2.14}$$

This equation shows that the signal is proportional to the square of the source amplitude $\underline{A}_0(t)$ and to the reference mirror reflectivity r_{R}. Further, the signal is given by an integration of all reflectivities $r_{\mathrm{s}}(t_{\mathrm{s}}v_{\mathrm{s}}/2)$ in the optical sample path. The contribution strength of each reflection is governed by the baseband coherence function $\kappa_{\mathrm{L}}(\tau_{\mathrm{r}}-t_{\mathrm{s}})$ and thus depends on the difference in path-length distance with respect to the reference path. The cosine-term leads to a harmonic oscillation of the signal when tuning the carrier frequency or changing the reference mirror position.

The OCT signal, Eq. (2.7), also contains a part that is proportional to the optical power returning from the reference arm. With Eq. (2.6) this part is given by

$$\overline{|\underline{E}_{\mathrm{r}}|^2}=\overline{\left|\frac{\mathrm{j}}{2}r_{\mathrm{R}}\underline{A}_0(t-\tau_{\mathrm{r}})\mathrm{e}^{\mathrm{j}\,\omega_0(t-\tau_{\mathrm{r}})}\right|^2}=\frac{1}{4}r_{\mathrm{R}}^2\overline{|\underline{A}_0(t)|^2}. \tag{2.15}$$

In contrast to the sample-reference interference, the mixing of reference with reference fields results in a constant term, since only reflections from a single depth occur.

Moreover, the OCT signal in Eq. (2.7), contains a part that is proportional to the optical power returning from the sample arm. Using Eq. (2.6), the mixing of fields from all sample reflections is calculated to

$$\begin{aligned}\overline{\left|\underline{E}_\mathrm{s}\right|^2} = \left|\overline{\underline{E}_\mathrm{s}\underline{E}_\mathrm{s}^*}\right| = \Bigg|\overline{\frac{\mathrm{j}}{2}\int_{-\infty}^{+\infty} h_\mathrm{s}(t_\mathrm{s})\,\underline{A}_0(t-t_\mathrm{s})\,\mathrm{e}^{\mathrm{j}\,\omega_0(t-t_\mathrm{s})}\mathrm{d}t_\mathrm{s}} \\ \cdot \overline{\frac{-\mathrm{j}}{2}\int_{-\infty}^{+\infty} h_\mathrm{s}(t_\mathrm{s}')\,\underline{A}_0^*(t-t_\mathrm{s}')\,\mathrm{e}^{-\mathrm{j}\,\omega_0(t-t_\mathrm{s}')}\mathrm{d}t_\mathrm{s}'}\Bigg| \\ = \frac{1}{4}\left|\overline{\int_{-\infty}^{+\infty}\int_{-\infty}^{+\infty} \underline{A}_0(t-t_\mathrm{s})\,\underline{A}_0^*(t-t_\mathrm{s}')\,h_\mathrm{s}(t_\mathrm{s})\,h_\mathrm{s}(t_\mathrm{s}')\,\mathrm{e}^{-\mathrm{j}\,\omega_0(t_\mathrm{s}-t_\mathrm{s}')}\mathrm{d}t_\mathrm{s}\mathrm{d}t_\mathrm{s}'}\right|,\end{aligned} \tag{2.16}$$

using the integration variables $t_\mathrm{s}, t_\mathrm{s}'$ for discrimination of the two integrals. The harmonic sample-sample interference term depends on the path length, and thus on the temporal differences $t_\mathrm{s} - t_\mathrm{s}'$ between the individual sample backscatterers. In order to calculate the interference signal, the integral is first written down twice, then in the second part, the integration variables are exchanged, which results in an expression of the complex conjugate (CC) of the first part. Hence, an expression of the real value results,

$$\begin{aligned}
\overline{|\underline{E}_\mathrm{s}|^2} &= \frac{1}{4}\cdot\frac{1}{2}\Bigg|\overline{\int_{-\infty}^{+\infty}\int_{-\infty}^{+\infty}\underline{A}_0(t-t_\mathrm{s})\underline{A}_0^*(t-t_\mathrm{s}')h_\mathrm{s}(t_\mathrm{s})h_\mathrm{s}(t_\mathrm{s}')\mathrm{e}^{-\mathrm{j}\omega_0(t_\mathrm{s}-t_\mathrm{s}')}\mathrm{d}t_\mathrm{s}\mathrm{d}t_\mathrm{s}'} \\
&\qquad + \overline{\int_{-\infty}^{+\infty}\int_{-\infty}^{+\infty}\underline{A}_0(t-t_\mathrm{s})\underline{A}_0^*(t-t_\mathrm{s}')h_\mathrm{s}(t_\mathrm{s})h_\mathrm{s}(t_\mathrm{s}')\mathrm{e}^{-\mathrm{j}\omega_0(t_\mathrm{s}-t_\mathrm{s}')}\mathrm{d}t_\mathrm{s}\mathrm{d}t_\mathrm{s}'}\Bigg| \\
&= \frac{1}{8}\Bigg|\overline{\int_{-\infty}^{+\infty}\int_{-\infty}^{+\infty}\underline{A}_0(t-t_\mathrm{s})\underline{A}_0^*(t-t_\mathrm{s}')h_\mathrm{s}(t_\mathrm{s})h_\mathrm{s}(t_\mathrm{s}')\mathrm{e}^{-\mathrm{j}\omega_0(t_\mathrm{s}-t_\mathrm{s}')}\mathrm{d}t_\mathrm{s}\mathrm{d}t_\mathrm{s}'} \\
&\qquad \underbrace{+\overline{\int_{-\infty}^{+\infty}\int_{-\infty}^{+\infty}\underline{A}_0^*(t-t_\mathrm{s})\underline{A}_0(t-t_\mathrm{s}')h_\mathrm{s}(t_\mathrm{s}')h_\mathrm{s}(t_\mathrm{s})\mathrm{e}^{\mathrm{j}\omega_0(t_\mathrm{s}-t_\mathrm{s}')}\mathrm{d}t_\mathrm{s}\mathrm{d}t_\mathrm{s}'}}_{CC}\Bigg| \\
&= \frac{1}{8}\int_{-\infty}^{+\infty}\int_{-\infty}^{+\infty}h_\mathrm{s}(t_\mathrm{s})h_\mathrm{s}(t_\mathrm{s}')2\,\mathrm{Re}\left\{\overline{\underline{A}_0(t-t_\mathrm{s})\underline{A}_0^*(t-t_\mathrm{s}')\mathrm{e}^{-\mathrm{j}\omega_0(t_\mathrm{s}-t_\mathrm{s}')}}\right\}\mathrm{d}t_\mathrm{s}\mathrm{d}t_\mathrm{s}'.
\end{aligned} \tag{2.17}$$

Using the definition of the real-valued coherence function in the baseband, Eqs. (2.9), (2.11) and (2.13), the sample-sample interference term is expressed as

$$\begin{aligned}
\overline{|\underline{E}_\mathrm{s}|^2} &= \frac{1}{4}\int_{-\infty}^{+\infty}\int_{-\infty}^{\infty}h_\mathrm{s}(t_\mathrm{s})h_\mathrm{s}(t_\mathrm{s}')\,\mathrm{Re}\left\{\underline{\Gamma}_0(t_\mathrm{s}'-t_\mathrm{s})\right\}\mathrm{d}t_\mathrm{s}\mathrm{d}t_\mathrm{s}' \\
&= \frac{1}{2}\overline{|\underline{A}_0|^2}\int_{-\infty}^{+\infty}\int_{-\infty}^{\infty}h_\mathrm{s}(t_\mathrm{s})h_\mathrm{s}(t_\mathrm{s}')\,\kappa_\mathrm{L}(t_\mathrm{s}'-t_\mathrm{s})\cos\left(\omega_0(t_\mathrm{s}'-t_\mathrm{s})\right)\mathrm{d}t_\mathrm{s}\mathrm{d}t_\mathrm{s}'.
\end{aligned} \tag{2.18}$$

In comparison to the sample-reference interference, Eq. (2.14), the sample-sample interference depends on the mutual return time differences from reflexions inside the sample. Due to sample reflectivities that are typically weaker than the reference reflectivity, the sample-sample mixing term is also weak, compared to the sample-reference interference.

The calculation leads to an entire OCT signal, which is dependent on the optical return time differences in both reference and sample path. By inserting

Eqs. (2.14), (2.15) and (2.18) into Eq. (2.7), the squared electric field on the photodetector amounts to

$$\overline{\left|\underline{E}_\mathrm{d}\right|^2} = \overline{\left|\underline{A}_0\right|^2}\Bigg[\underbrace{\frac{1}{4}r_\mathrm{R}^2}_{\text{const. term}} + \underbrace{\frac{1}{2}\int_{-\infty}^{+\infty}\int_{-\infty}^{\infty} h_\mathrm{s}(t_\mathrm{s})h_\mathrm{s}(t_\mathrm{s}')\,\kappa_\mathrm{L}(t_\mathrm{s}'-t_\mathrm{s})\cos\left(\omega_0(t_\mathrm{s}'-t_\mathrm{s})\right)\mathrm{d}t_\mathrm{s}\mathrm{d}t_\mathrm{s}'}_{\text{sample-sample interference}} + \underbrace{r_\mathrm{R}\int_{-\infty}^{+\infty} h_\mathrm{s}(t_\mathrm{s})\kappa_\mathrm{L}(\tau_\mathrm{r}-t_\mathrm{s})\cos\left(\omega_0(\tau_\mathrm{r}-t_\mathrm{s})\right)\mathrm{d}t_\mathrm{s}}_{\text{sample-reference interference: OCT signal}}\Bigg]. \tag{2.19}$$

In the following, the sample-reference interference signal $i_\mathrm{c}' = 2\,\mathrm{Re}\left\{\overline{\underline{E}_\mathrm{s}\underline{E}_\mathrm{r}^*}\right\}$ is in the focus, which represents the actual OCT measurement signal, compare also Eq. (2.14). Constant factors like the area and the responsivity of the photodetector are omitted. We describe this signal as an effective photocurrent i_c', since it is proportional to a detected photocurrent i_c, where the subscript denotes correlation of sample and reference path. The time integral in Eq. (2.14) is now evaluated for the specific cases of first a TD-OCT system and second an FD-OCT system.

In case of a TD-OCT system, the light source emits broadband light, which means the complex slowly-varying random amplitude $\underline{A}_0(t)$ is broadband noise, and thus the coherence time τ_c of the light is small. The coherence time is the time span, in which the normalized baseband coherence function is approximately one, $\kappa_\mathrm{L}(\tau_\mathrm{r}-t_\mathrm{s})\approx 1$, if $|\tau_\mathrm{r}-t_\mathrm{s}|\leq\tau_\mathrm{c}$. For larger time differences $|\tau_\mathrm{r}-t_\mathrm{s}|>\tau_\mathrm{c}$, the coherence function is approximately zero. The measurement signal in Eq. (2.14) contains the convolution of sample impulse response with the coherence function, $h_\mathrm{s}(t_\mathrm{s})*\left[\kappa_\mathrm{L}(\tau_\mathrm{r})\cos(\omega_0\tau_\mathrm{r})\right]$. In an idealized case, $\underline{A}_0(t)$ represents noise of bandwidth $1/\tau_\mathrm{c}$. With the approximation of $\tau_\mathrm{c}\to 0$, the convolution approaches the term $h_\mathrm{s}(\tau_\mathrm{r})\tau_\mathrm{c}$. Accordingly, the measurement signal in Eq. (2.14) becomes

$$\begin{aligned} i'_{\mathrm{c,TD}} &= K_{\mathrm{L}}(0)\, r_{\mathrm{R}}\, \tau_{\mathrm{c}}\, h_{\mathrm{s}}(\tau_{\mathrm{r}}) \\ &= \overline{\left|\underline{A}_0(t)\right|^2}\, r_{\mathrm{R}}\, \tau_{\mathrm{c}}\, r_{\mathrm{s}} \left(\frac{v_{\mathrm{s}}}{2}\tau_{\mathrm{r}}\right) \frac{v_{\mathrm{s}}}{2}. \end{aligned} \tag{2.20}$$

This shows that the signal current is in direct proportion to the impulse response and to the reflectivity profile of the sample. In the realistic case of a limited bandwidth of the source, the convolution of the sample impulse response with the coherence function leads to a limited depth measurement resolution of $\delta z = v_{\mathrm{s}} \tau_{\mathrm{c}}$.

In the case of an FD-OCT system, both in the sense of an SD-OCT or in the sense of an SS-OCT, narrow-band light is applied, either by using a tunable narrowband light source (SS-OCT) or by spectrally filtering the detected light (SD-OCT). Thus, with a narrow bandwidth, a long coherence length allows the interference of backscattered sample light with light travelling along the reference path for long path-length differences. As a consequence, the reference mirror does not have to be moved any more, and interference from various depths in the sample can be measured simultaneously. In an ideal case, the coherence time τ_{c} of the detected light is infinite and the baseband coherence function $\kappa_0(\tau) \approx 1$ equals one for all time differences τ. The measurement signal in Eq. (2.14) then results in

$$i'_{\mathrm{c,FD}}(\omega_0) = K_{\mathrm{L}}(0)\, r_{\mathrm{R}} \int_{-\infty}^{+\infty} h_{\mathrm{s}}(t_{\mathrm{s}}) \cos\left(\omega_0 (\tau_{\mathrm{r}} - t_{\mathrm{s}})\right) \mathrm{d}t_{\mathrm{s}}. \tag{2.21}$$

In FD-OCT, the frequency-dependent photocurrent $i'_{\mathrm{c,FD}}(\omega_0)$ is in direct proportion to the Fourier transform of the temporal field impulse response of the sample. The following calculation shows this relation.

The cosine in Eq. (2.21) can be expressed by exponential functions

$$i'_{\mathrm{c,FD}}(\omega_0) = K_{\mathrm{L}}(0) r_{\mathrm{R}} \int_{-\infty}^{+\infty} h_{\mathrm{s}}(t_{\mathrm{s}}) \frac{1}{2}\left(\mathrm{e}^{\mathrm{j}\omega_0(\tau_{\mathrm{r}}-t_{\mathrm{s}})} + \mathrm{e}^{-\mathrm{j}\omega_0(\tau_{\mathrm{r}}-t_{\mathrm{s}})}\right) \mathrm{d}t_{\mathrm{s}}$$

$$= \frac{1}{2} K_{\mathrm{L}}(0) r_{\mathrm{R}} \left[\int_{-\infty}^{+\infty} h_{\mathrm{s}}(t_{\mathrm{s}}) \mathrm{e}^{\mathrm{j}\omega_0(\tau_{\mathrm{r}}-t_{\mathrm{s}})} \mathrm{d}t_{\mathrm{s}} + \int_{-\infty}^{+\infty} h_{\mathrm{s}}(t_{\mathrm{s}}) \mathrm{e}^{-\mathrm{j}\omega_0(\tau_{\mathrm{r}}-t_{\mathrm{s}})} \mathrm{d}t_{\mathrm{s}} \right], \tag{2.22}$$

which represent Fourier transforms (FT, see Appendix A.1) of the sample impulse response,

$$i'_{\mathrm{c,FD}}(\omega_0) = \frac{1}{2} K_{\mathrm{L}}(0) r_{\mathrm{R}} \times \left[\underbrace{\int_{-\infty}^{+\infty} h_{\mathrm{s}}(t_{\mathrm{s}}) \mathrm{e}^{-\mathrm{j}\omega_0 t_{\mathrm{s}}} \mathrm{d}t_{\mathrm{s}}}_{\breve{\underline{h}}_{\mathrm{s}}(f_0)} \mathrm{e}^{\mathrm{j}\omega_0\tau_{\mathrm{r}}} + \underbrace{\int_{-\infty}^{+\infty} h_{\mathrm{s}}(t_{\mathrm{s}}) \mathrm{e}^{\mathrm{j}\omega_0 t_{\mathrm{s}}} \mathrm{d}t_{\mathrm{s}}}_{\breve{\underline{h}}_{\mathrm{s}}(-f_0)} \mathrm{e}^{-\mathrm{j}\omega_0\tau_{\mathrm{r}}} \right]. \tag{2.23}$$

The complex field transfer function $\breve{\underline{h}}_{\mathrm{s}}(f)$ of the sample is the Fourier transform of the temporal field impulse response

$$\breve{\underline{h}}_{\mathrm{s}}(f) = \int_{-\infty}^{+\infty} h_{\mathrm{s}}(t_{\mathrm{s}}) \mathrm{e}^{-\mathrm{j}2\pi f t_{\mathrm{s}}} \mathrm{d}t_{\mathrm{s}} \ . \tag{2.24}$$

The Fourier integrals in Eq. (2.23) can then be written as

$$i'_{\mathrm{c,FD}}(f_0) = \frac{1}{2} K_{\mathrm{L}}(0) r_{\mathrm{R}} \left[\breve{\underline{h}}_{\mathrm{s}}(-f_0) \mathrm{e}^{-\mathrm{j}2\pi f_0 \tau_{\mathrm{r}}} + \breve{\underline{h}}_{\mathrm{s}}(f_0) \mathrm{e}^{\mathrm{j}2\pi f_0 \tau_{\mathrm{r}}} \right]. \tag{2.25}$$

Equation (2.25) expresses the measurement signal of a FD-OCT system and shows that the measurement signal is proportional to the complex field transfer function of the sample.

In contrast to the general case of a sample with an arbitrary complex impulse response, the following section illustrates the case of a plane mirror as a test sample in an FD-OCT measurement. The test sample leads to a single reflection with a return time $t_{\mathrm{s},1}$ and a real-valued field amplitude reflectivity of $r_{\mathrm{s},1}$, leading to an impulse response of $h_{\mathrm{s},1}(t_{\mathrm{s}}) = r_{\mathrm{s},1}\, \delta(t_{\mathrm{s}} - t_{\mathrm{s},1})$. Accordingly, the

complex field transfer function becomes $\underline{\breve{h}}_{\mathrm{s},1}(f) = r_{\mathrm{s},1}\,\mathrm{e}^{-\mathrm{j}2\pi f t_{\mathrm{s},1}}$ and the measurement signal of such a sample is

$$\begin{aligned} i'_{\mathrm{c,FD},1}(f_0) &= \frac{1}{2} K_{\mathrm{L}}(0) r_{\mathrm{R}} \left[r_{\mathrm{s},1}\mathrm{e}^{-\mathrm{j}2\pi f_0(\tau_{\mathrm{r}} - t_{\mathrm{s},1})} + r_{\mathrm{s},1}\mathrm{e}^{\mathrm{j}2\pi f_0(\tau_{\mathrm{r}} - t_{\mathrm{s},1})} \right] \\ &= K_{\mathrm{L}}(0) r_{\mathrm{R}} r_{\mathrm{s},1} \cos\left(2\pi f_0 (\tau_{\mathrm{r}} - t_{\mathrm{s},1})\right). \end{aligned} \tag{2.26}$$

This equation describes a real-valued signal, which is dependent on the optical center frequency f_0 of the detected spectral slice. The FD-OCT measurement is performed for a range of optical frequencies, $(f_{\mathrm{m}} - \Delta f/2) \le f_0 \le (f_{\mathrm{m}} + \Delta f/2)$, with centre frequency f_{m} and measurement frequency span Δf. For the determination of the time- or equivalent depth-dependent signal, an inverse Fourier transform can be applied. Because the input spectrum is real-valued, this transformation results in a complex symmetric time-domain signal with components at positive and complex-conjugate components at negative times, with respect to the reference arm return time τ_{r}. A sample reflection with a positive return time $t_{\mathrm{s},1} - \tau_{\mathrm{r}} > 0$, thus appears also at the negative time difference $\tau_{\mathrm{r}} - t_{\mathrm{s},1}$, and vice versa. The inability to discriminate between positive and negative times or depths is often referred to as depth degeneracy [42].

For SS-OCT, the carrier frequency $f_0(t)$ is subject to a temporal variation, and the signal associated with a single reflection within the sample, Eq. (2.26), is given by an oscillation along the carrier frequency axis, $\cos\left(2\pi f_0(t)(\tau_{\mathrm{r}} - t_{\mathrm{s},1})\right)$. The return time difference $\tau_{\mathrm{r}} - t_{\mathrm{s},1}$ between a sample reflection and the reference path return time causes an intermediate frequency, whose value allows the determination of the time difference. If the optical carrier frequency f_0 is increased over time, see Figure 2.1, with a linear tuning slope $s_{\mathrm{sw}} = \Delta f / T_{\mathrm{sw}}$ and frequency ramp duration T_{sw}, starting at $t = t_0$, the time-dependent carrier frequency is given by $f_0(t) = (f_{\mathrm{m}} - \Delta f/2) + s_{\mathrm{sw}}(t - t_0)$. This dependence allows to calculate the electrical signal frequencies $f_{\mathrm{sig},1}$ occurring in the SS-OCT measurement signal

$$
\begin{aligned}
i'_{\mathrm{c,FD},1}(t) &\sim \cos\left(2\pi f_0(t)\left(\tau_\mathrm{r} - t_{\mathrm{s},1}\right)\right) \\
i'_{\mathrm{c,FD},1}(t) &\sim \cos\left(2\pi\left[\, f_\mathrm{m} - \Delta f/2 + s_\mathrm{sw}\left(t - t_0\right)\right]\left(\tau_\mathrm{r} - t_{\mathrm{s},1}\right)\right) \\
&\sim \cos\left(\underbrace{2\pi\left[\, f_\mathrm{m} - \Delta f/2 - s_\mathrm{sw} t_0\right]\left(\tau_\mathrm{r} - t_{\mathrm{s},1}\right)}_{\varphi_0} + 2\pi \underbrace{s_\mathrm{sw}\left(\tau_\mathrm{r} - t_{\mathrm{s},1}\right)}_{f_{\mathrm{sig},1}} t\right) \\
&\sim \cos\left(\varphi_0 + 2\pi f_{\mathrm{sig},1} t\right).
\end{aligned}
\tag{2.27}
$$

The measured signal has a phase offset φ_0. Note that in practical tunable lasers, the different frequency points might be subject to different offset phases. This signal model, however, assumes a chirped laser source with a continuous phase. Any initial phase offset would be present in both sample and reference arm and would thus cancel out in the measurement. The frequency of the measured signal is

$$
f_{\mathrm{sig},1} = \left(\tau_\mathrm{r} - t_{\mathrm{s},1}\right) s_\mathrm{sw} = \left(\tau_\mathrm{r} - t_{\mathrm{s},1}\right) \Delta f / T_\mathrm{sw} \,. \tag{2.28}
$$

The temporal dependence of the carrier frequencies f_0, returning from reference and sample path are depicted schematically in Figure 2.1.

The frequency ramps are assumed to be linear in time with a frequency span of Δf and a ramp time T_sw, giving a slope $s_\mathrm{sw} = \Delta f / T_\mathrm{sw}$. Depending on the return time difference $\tau_\mathrm{r} - t_{\mathrm{s},1}$ of reference and sample arm, the intermediate frequency of the OCT signal by heterodyne down-conversion amounts to $f_{\mathrm{sig},1} = (\tau_\mathrm{r} - t_{\mathrm{s},1})\, s_\mathrm{sw}$.

In order to estimate the signal frequencies in a real system, an exemplary case is investigated with a measurement frequency span of $\Delta f_1 = \left(\Delta\lambda_1 / \lambda_\mathrm{m}^2\right) c_0 = 17.5\,\mathrm{THz}$, which corresponds to a wavelength span of $\Delta\lambda_1 = 100\,\mathrm{nm}$ at a centre wavelength of $\lambda_{\mathrm{m},1} = 1310\,\mathrm{nm}$. Here, the frequency ramp time is assumed to be $T_{\mathrm{sw},1} = 500\,\mu\mathrm{s}$ and the return time difference of reference and sample path is given by $\tau_\mathrm{r} - t_{\mathrm{s},1} = 2z_1/c_0$. Sample and reference path velocities are assumed to match the vacuum speed of light, and the depth difference of both paths is $z_1 = 1\,\mathrm{mm}$. In this case, the measured signal frequency is expected to be $f_{\mathrm{sig},1} = \left(2z_1/c_0\right)\left(\Delta f_1 / T_{\mathrm{sw},1}\right) = 233\,\mathrm{kHz}$. Thus,

photodiode bandwidths and analogue-to-digital converter sampling speed should be adapted to the expected signal frequency.

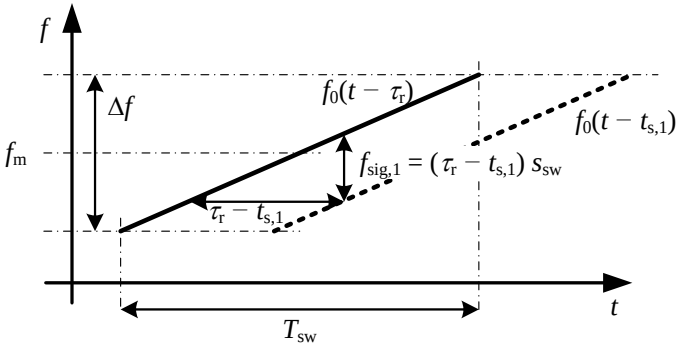

Figure 2.1: Frequency ramp used for an SS-OCT scan. The carrier frequency f_0 is increased linearly over time t. One scan of frequency range Δf centred around a frequency f_m takes the time T_sw, thus the frequency slope is $s_\mathrm{sw} = \Delta f / T_\mathrm{sw}$. The carrier frequency $f_0(t - \tau_\mathrm{r})$ (solid) of the light returning from the reference path with round-trip time τ_r and the carrier frequency $f_0(t - t_{\mathrm{s},1})$ (dashed) of the light returning from the sample path with round-trip time $t_{\mathrm{s},1}$ have a frequency difference of $f_{\mathrm{sig},1}$, which gives the intermediate frequency of the mixing product.

The limited frequency span has an influence on the depth resolution of the measurement. In practice, the frequency span Δf is limited due to either the source tuning range (SS-OCT) or the emission bandwidth of the superluminescent diode (SD-OCT). In order to account for this, the measurement signal in Eq. (2.25) is considered as a spectrum, multiplied by a windowing function in frequency, $\mathrm{W}(f_0) = \mathrm{rect}_{\Delta f}(f_0 - f_\mathrm{m})$, here given by a frequency-shifted rectangular function, see Appendix A.1 for the definition and Figure 2.2 for a visualization. Accordingly, the measurement signal is denoted by the following equation

$$i'_{\mathrm{c,FD}}(f_0) = \frac{1}{2} K_\mathrm{L}(0) r_\mathrm{R} W(f_0) \left[\breve{\underline{h}}_\mathrm{s}(f_0) \mathrm{e}^{\mathrm{j}2\pi f_0 \tau_\mathrm{r}} + \breve{\underline{h}}_\mathrm{s}(-f_0) \mathrm{e}^{-\mathrm{j}2\pi f_0 \tau_\mathrm{r}} \right]. \quad (2.29)$$

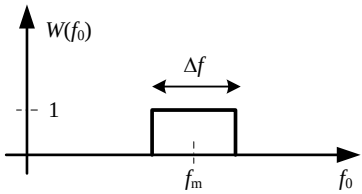

Figure 2.2: Window function $W(f_0)$ describing the bandwidth-limited scanning range of the FD-OCT signal, centred around f_m. In this case, the window is given by a rectangular function of width Δf.

In order to obtain the temporal response of the sample from the measurement signal, an inverse Fourier transform with respect to f_0 is applied to Eq. (2.29),

$$\begin{aligned} \breve{i}'_{\mathrm{c,FD}}(t_\mathrm{s}) = \frac{1}{2} K_\mathrm{L}(0) r_\mathrm{R} \Bigg[& \int_{-\infty}^{+\infty} W(f_0) \breve{\underline{h}}_\mathrm{s}(f_0) \mathrm{e}^{\mathrm{j}2\pi f_0 \tau_\mathrm{r}} \mathrm{e}^{\mathrm{j}2\pi f_0 t_\mathrm{s}} \mathrm{d}f_0 \\ & + \int_{-\infty}^{+\infty} W(f_0) \breve{\underline{h}}_\mathrm{s}(-f_0) \mathrm{e}^{-\mathrm{j}2\pi f_0 \tau_\mathrm{r}} \mathrm{e}^{\mathrm{j}2\pi f_0 t_\mathrm{s}} \mathrm{d}f_0 \Bigg]. \end{aligned} \tag{2.30}$$

The windowing function and the measurement signal can be transformed separately. The transformation of the windowing function

$$\breve{W}(t_\mathrm{s}) = \int_{-\infty}^{+\infty} W(f_0) \mathrm{e}^{\mathrm{j}2\pi f_0 t_\mathrm{s}} \mathrm{d}t_\mathrm{s}\,, \tag{2.31}$$

is in this case the transformation of a frequency-shifted rectangular function and is expressed by the following modulated sinc-function

$$\begin{aligned} \breve{W}(t_\mathrm{s}) &= \int_{-\infty}^{+\infty} \mathrm{rect}_{\Delta f}(f_0 - f_\mathrm{m}) \mathrm{e}^{\mathrm{j}2\pi f_0 t_\mathrm{s}} \mathrm{d}t_\mathrm{s} \\ &= \Delta f \,\mathrm{sinc}(\pi t_\mathrm{s} \Delta f) \mathrm{e}^{\mathrm{j}2\pi f_\mathrm{m} t_\mathrm{s}}. \end{aligned} \tag{2.32}$$

The time-domain width of the sinc is reciprocal to the measurement bandwidth Δf. The exponential phase modulation can be omitted, as the representation of the measurement as an A-scan usually contains only the absolute value.

The former multiplication of measurement signal and windowing function, see Eq. (2.30), is now expressed by a convolution of their individual transformation products

$$\breve{i}'_{\mathrm{c,FD}}(t_\mathrm{s}) = \frac{1}{2} K_\mathrm{L}(0) r_\mathrm{R} \left[\breve{W}(t_\mathrm{s}) * \int_{-\infty}^{+\infty} \breve{\underline{h}}_\mathrm{s}(f_0) \mathrm{e}^{\mathrm{j}2\pi f_0 \tau_\mathrm{r}} \mathrm{e}^{\mathrm{j}2\pi f_0 t_\mathrm{s}} df_0 + \breve{W}(t_\mathrm{s}) * \int_{-\infty}^{+\infty} \breve{\underline{h}}_\mathrm{s}(-f_0) \mathrm{e}^{-\mathrm{j}2\pi f_0 \tau_\mathrm{r}} \mathrm{e}^{\mathrm{j}2\pi f_0 t_\mathrm{s}} df_0 \right]. \tag{2.33}$$

The inverse transform of $\breve{\underline{h}}_\mathrm{s}(f_0)\mathrm{e}^{\mathrm{j}2\pi f_0 \tau_\mathrm{r}}$ is identical to a time-shift of the sample impulse response $h_\mathrm{s}(t_\mathrm{s})$ by the reference path return time τ_r, see Eq. (A.4). With the auxiliary variables $\xi_1 = t_\mathrm{s} + \tau_\mathrm{r}$ and $\xi_2 = t_\mathrm{s} - \tau_\mathrm{r}$ the integrals in Eq. (2.33) are

$$\begin{aligned} \int_{-\infty}^{+\infty} \breve{\underline{h}}_\mathrm{s}(f_0) \mathrm{e}^{\mathrm{j}2\pi f_0 \xi} df_0 &= h_\mathrm{s}(\xi_1) = h_\mathrm{s}(\tau_\mathrm{r} + t_\mathrm{s}) \\ \int_{-\infty}^{+\infty} \breve{\underline{h}}_\mathrm{s}(-f_0) \mathrm{e}^{\mathrm{j}2\pi f_0 \xi_2} df_0 &= \mathrm{h}_\mathrm{s}(-\xi_2) = \mathrm{h}_\mathrm{s}(\tau_\mathrm{r} - t_\mathrm{s}), \end{aligned} \tag{2.34}$$

and the entire Eq. (2.33) results in

$$\breve{i}'_{\mathrm{c,FD}}(t_\mathrm{s}) = \frac{1}{2} K_\mathrm{L}(0) r_\mathrm{R} \left[\breve{W}(t_\mathrm{s}) * h_\mathrm{s}(\tau_\mathrm{r} + t_\mathrm{s}) + \breve{W}(t_\mathrm{s}) * h_\mathrm{s}(\tau_\mathrm{r} - t_\mathrm{s}) \right]. \tag{2.35}$$

Expressed in sample reflectivities, this reads

$$\breve{i}'_{\mathrm{c,FD}}(t_\mathrm{s}) = \frac{1}{2} K_\mathrm{L}(0) r_\mathrm{R} \left[\breve{W}(t_\mathrm{s}) * r_\mathrm{s}\left(\frac{v_\mathrm{r}}{2}\tau_\mathrm{r} + \frac{v_\mathrm{s}}{2} t_\mathrm{s} \right) \frac{v_\mathrm{s}}{2} + \breve{W}(t_\mathrm{s}) * r_\mathrm{s}\left(\frac{v_\mathrm{r}}{2}\tau_\mathrm{r} - \frac{v_\mathrm{s}}{2} t_\mathrm{s} \right) \frac{v_\mathrm{s}}{2} \right]. \tag{2.36}$$

The inverse transform of the measurement signal corresponds to the sample reflectivity profile mirrored at z_r, but is mainly influenced by three effects: Depth degeneracy, window artefacts and coherence decay. These are explained in detail in the following section.

The measured profile $r_s(z_r + z_s)$, $r_s(z_r - z_s)$ occurs twice, which is referred to as "depth-degeneracy". This effect is related to the real-valued input spectrum, Eq. (2.21), leading to a symmetric result of the inverse Fourier transform. Positive and negative path-length differences cannot be discriminated and superimpose. Further, since each singular reflection is broadened by the convolution with the window response $\breve{W}(t_s)$, this causes a limited resolution $\delta t_s = 1/\Delta f$ in sample response time and accordingly a limited depth resolution $\delta z = v_s/(2\Delta f)$.

Up to now, the coherence time τ_c of the source was assumed to be infinite. Now the case is regarded, where the baseband coherence function $\kappa_L(\tau_r - t_s)$, see Eq. (2.19), is limited to a finite width τ_c. This time is typically large enough to allow coherence lengths in the millimetre range, but significantly limits the imaging depth in the sample. With this influence, Eq. (2.35) can be written as

$$\begin{aligned} \breve{i}'_{c,FD}(t_s) = \frac{1}{2} K_L(0) r_R \big[&\breve{W}(t_s) * \kappa_L(\tau_r - t_s) h_s(\tau_r + t_s) \\ &+ \breve{W}(t_s) * \kappa_L(\tau_r - t_s) h_s(\tau_r - t_s) \big]. \end{aligned} \tag{2.37}$$

The impulse response of the sample $h_s(t_s)$ is multiplied by $\kappa_L(\tau_r - t_s)$ and the signal intensity decreases, once the path-length difference of sample and reference path increases. The measurable range of sample response times is limited by the coherence length $\Delta t_s = \tau_c$, leading to a maximum measurement depth of $\Delta z = \tau_c v_s/2$. Figure 2.3 visualizes the different effects on a FD-OCT measurement signal. The amplitudes of all signal components are plotted versus response time t_s.

The original sample response is assumed to consist of three infinitely sharp responses at times $t_{s,1}$, $t_{s,2}$, $t_{s,3}$ (black). The reference path return time is τ_r (dotted vertical line). The measured sample response, see Eq. (2.37) (absolute value in blue), is subject to mirroring at the reference path return time, to a decay with the coherence function $\kappa_L(\tau_r - t_s)$ (red), and to broadening by convolution with the time response of the spectral window $\breve{W}(t_s)$ (absolute value in green), here assumed to be of a sinc-shape, i.e. by a rectangular

spectrum, Figure 2.2. Note that an actual OCT signal would contain parts from sample-sample and reference-reference interference as well, which are both not included in this investigation. For a mitigation of the undesired signal components emerging from interference of fields from the same path, most practical measurement setups include balanced detection, where these signal components are suppressed, see Section 2.1.4. Here, only the signal originating from sample-reference interference $\left|\breve{i}'_{\mathrm{c,FD}}\left(t_{\mathrm{s}}\right)\right|$ is shown.

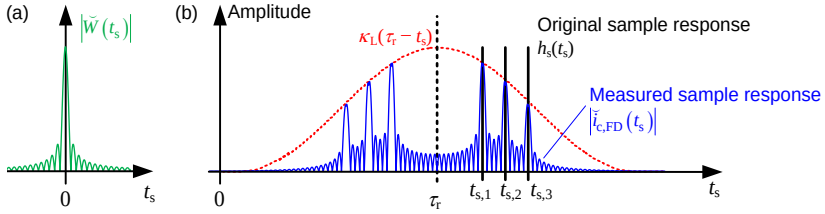

Figure 2.3: (a) Visualization of the absolute value of the time response of the spectral window $\left|\breve{W}\left(t_{\mathrm{s}}\right)\right|$, here assumed of sinc-shape. (b) Visualization of an original (black) and measured by FD-OCT (blue) sample response, $h_{\mathrm{s}}\left(t_{\mathrm{s}}\right)$, $\left|\breve{i}'_{\mathrm{c,FD}}\left(t_{\mathrm{s}}\right)\right|$, respectively. The original profile is idealized as three sharp peaks. The measured profile is subject to three effects: mirroring of the original profile at the reference return time τ_{r}, decay of the coherence function $\kappa_{\mathrm{L}}\left(\tau_{\mathrm{r}}-t_{\mathrm{s}}\right)$, (red), and broadening of each peak by the time response of the spectral window $\breve{W}\left(t_{\mathrm{s}}\right)$.

2.1.2 Lateral resolution and focal measurement range

In OCT, three-dimensional images are obtained either by laterally scanning a laser beam over the sample or by moving the sample position laterally, both in addition to the depth-resolved backscatter measurement. Typically, the beams are considered to be Gaussian beams. In a conventional fibre-based system, standard single-mode fibres (SMF) guide light towards and away from the OCT scan head. The scan head includes scanning mirrors and a scan lens. The fundamental mode in these step-index fibres is the linearly polarized LP_{01} fibre-mode [43]. Its radial field distribution can be approximated by a Gaussian distribution. This Gaussian shape is conserved after transmission through the collimator and the scan lens objective [44] and results in a focussed Gaussian free-space beam in the sample, see Figure 2.4.

In the following, the lateral resolution and the axial measurement range of an OCT system are derived from the properties of a Gaussian beam, see Appendix A.5. The complex field amplitude of the dominant transversal field component of a Gaussian beam, as depicted with its radial amplitude and its axial profile in Figure 2.5, is given by

$$\underline{A}_{\mathrm{G}}(r,z) = A_{\mathrm{G},0}\,\frac{w_0}{w(z)}\,\mathrm{e}^{-\left(\frac{r}{w(z)}\right)^2}. \tag{2.38}$$

Accordingly, the intensity distribution of a Gaussian beam is

$$\begin{aligned} I_{\mathrm{G}}(r,z) &\sim \left|\underline{A}_{\mathrm{G}}(r,z)\right|^2 \\ &= I_{\mathrm{G},0}\,\frac{w_0^2}{w^2(z)}\,\mathrm{e}^{-2\left(\frac{r}{w(z)}\right)^2}, \end{aligned} \tag{2.39}$$

with the radial distance r form the beam axis and the axial position z.

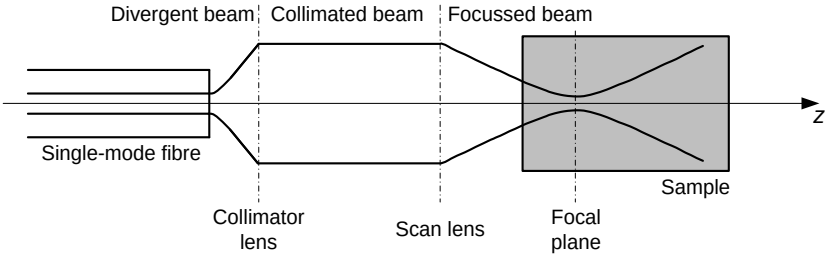

Figure 2.4: Schematical drawing of the Gaussian beam, which is emitted by the single-mode fibre. The beam is then collimated by the collimator lens and finally focussed into the sample by the scan lens. The focal plane of the scan lens defines the plane of best lateral resolution. In the drawing, the sample refractive index is assumed to match the surrounding refractive index. A scan mirror (not shown) can be placed in the collimated beam section.

The maximum intensity in the focal spot is given by $I_{\mathrm{G},0}$ and the radius of the beam waist is w_0. The beam profile $w(z)$ widens with axial distance from the position z_{f} of the beam waist according to

$$w(z) = w_0 \sqrt{1 + \left(\frac{\lambda (z - z_\mathrm{f})}{w_0^2 \pi} \right)^2} \,, \tag{2.40}$$

see Eq. (A.23) in Appendix A.5. For an analysis of the lateral resolution of the OCT system, we first calculate the focal response of the system, which is defined by both illumination and reception of the scattered power by the same optical system. This can be explained by a point scatterer as measurement target, which is exposed to the incident light, with an intensity distribution given by Eq. (2.39). Additionally, the efficiency for coupling scattered light back into the reception optics is governed by the same relation and reduces with radial and axial distance from the focal spot. Thus, the focal power response function $\eta_\mathrm{f}(r,z)$ is given by the squared normalized intensity

$$\eta_\mathrm{f}(r,z) = \frac{I_\mathrm{G}^2(r,z)}{I_\mathrm{G,0}^2} = \frac{w_0^4}{w^4(z)} \mathrm{e}^{-4\left(\frac{r}{w(z)}\right)^2} \,. \tag{2.41}$$

From the focal response function, two important system parameters can be derived: the lateral resolution and the axial measurement range. We define the lateral resolution in the focus at $z = z_\mathrm{f}$ as the span between the points, where the power response is $1/\mathrm{e}^2$. The lateral resolution thus is given by

$$\delta r = \sqrt{2}\, w_0 \,. \tag{2.42}$$

For the exemplary fibre-based OCT system described in this work, the beam waist is $w_0 = 18.8\,\mu\mathrm{m}$, and the lateral resolution at the beam waist is $\delta r = 26.6\,\mu\mathrm{m}$.

The focal measurement range Δz_f is determined from the decay of the focal power response function $\eta_\mathrm{f}(r,z)$ along the beam axis ($r = 0$) to 1/4. The span between both points with $\eta_\mathrm{f}(0,z) = 1/4$ is given by the confocal parameter b of the underlying Gaussian beam

$$\Delta z_\mathrm{f} = \frac{2\pi w_0^2}{\lambda} = b \,. \tag{2.43}$$

The focal measurement range in the system used in this work is $\Delta z_f = 1.7$ mm. The wider the beam waist and thus the worse the lateral resolution is, the longer is the focal measurement range. For an optimum OCT operation, it is useful to design the system such that the decay caused by coherence effects and the decay due to the axial focal response function are in a comparable range and hence do not unnecessarily limit each other. By choosing the coherence point in depth apart from the focus at z_f, both functions can even counteract and form a rather flat depth-response of the system.

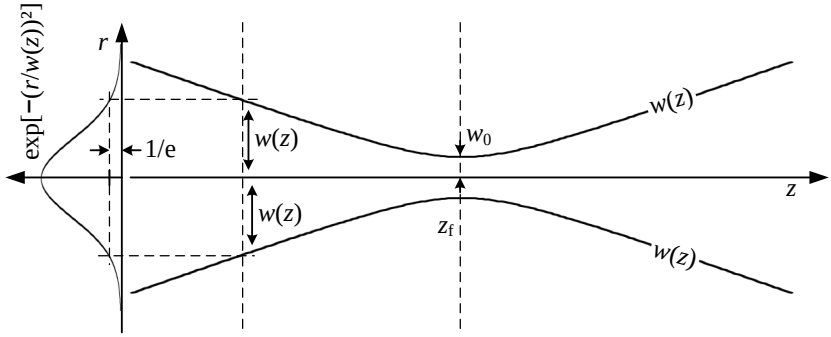

Figure 2.5: Gaussian beam illuminating the sample. Left: Normalized radial amplitude profile. Right: Axial profile of the beam with the beam waist of radius w_0 at the position z_f and the depth-evolution of the beam radius $w(z)$.

Some OCT systems use Bessel beams instead of Gaussian beams in order to improve the focal measurement range in scattering media. These beams are characterized by an energy flux from the outside lobes to the inner main lobe and are thus said to have self-healing properties [45] in scattering media. Bessel beams can be generated by sending a Gaussian beam through an axicon.

2.1.3 Sampling and DFT for acquisition of FD-OCT signals

For processing, display and storage, the OCT voltage signal is digitized, either by sampling and quantization of the photodetector output signal using an analogue-to-digital converter (ADC) in SS-OCT, or by digitizing the spectrometer

output, e.g., with a charge-coupled device (CCD) followed by an ADC, in SD-OCT. Sampling the signal in optical frequency steps f_0 with a limited number of samples M and a step size of δf_d covers a limited range of the optical spectrum $\Delta f_\mathrm{d} = M \delta f_\mathrm{d}$, see Figure 2.6 (a). Since positive and negative frequencies cannot be discriminated, only the positive part of the spectrum is sampled. The signal is processed by an (inverse) Fourier transform, see Eq. (2.30), which is performed digitally after sampling, using a discrete (inverse) Fourier transform (IDFT) algorithm, see Appendix A.2. The transformation with an (I)DFT generally links discretization in one domain with periodicity in the other domain. Specifically, the limited spectral observation range Δf_d leads to discrete data points separated by the resolution in return time $\delta t_\mathrm{d} = 1/(2\Delta f_\mathrm{d})$, and the step size δf_d in frequency-space leads to a limited unambiguity range $\Delta t_\mathrm{d} = 1/(2\delta f_\mathrm{d})$, see Figure 2.6 (b). The number of points M stays the same before and after the (I)DFT, however, after an (I)DFT, the data points are distributed over positive and negative sample path return times t_s. The number of relevant data points is reduced to M/2, since the complex amplitudes at positive and negative times are complex conjugate with respect to each other, thus containing redundant information. This fact corresponds to the depth-degeneracy as artefact in OCT signal reconstruction introduced in Chapter 2.1.1.

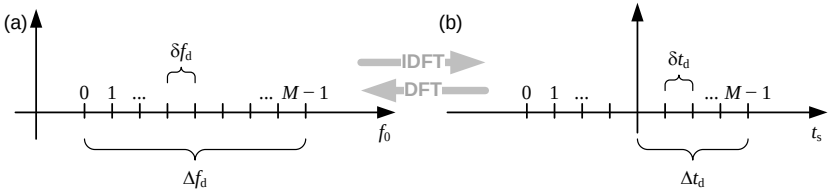

Figure 2.6: Illustration of discrete-Fourier-transform-(DFT-)related quantities in both frequency domain and time domain. (a) Sampling points 0, 1, … , $M-1$ in the frequency-domain, with total sampling range Δf_d, step size δf_d, and total number of sampling points M. (b) Data points 0, 1, … , $M-1$ after inverse DFT (IDFT) with one-sided unambiguity range of $\Delta t_\mathrm{d} = 1/(2\delta f_\mathrm{d})$, discretization $\delta t_\mathrm{d} = 1/(2\Delta f_\mathrm{d})$, and the number of points *M*.

The system design is chosen reasonably if the sampling-related temporal resolution δt_d and the coherence-related temporal resolution δt_s are in the same range. Furthermore, the sampling related unambiguity range Δt_d should not be significantly smaller than the coherence-related temporal range Δt_s. Otherwise, the measurement signal is superimposed by periodic backscatter from sample return times exceeding Δt_d.

2.1.4 Sensitivity considerations and noise analysis

The coherent mixing process of reflected sample light with reference-arm light is key to the high sensitivity of OCT, since the measured signal power in the electrical domain is proportional to both, the sample arm power and the typically higher reference arm power, see Eq. (2.19). In order to achieve systems with high sensitivity, one would apply strong reference arm powers to lift the signal power above the noise floor of the electronics. However, with rising power, light source related noise contributions also increase, like the relative intensity noise from the laser, while the signal power might run into a detection limit, given by, e.g., the maximum input voltage of the analogue-to-digital converter. Hence, a comprehensive noise analysis becomes important to achieve the optimum operating point. This section is focussed on the situation in fibre-based SS-OCT systems.

The following considerations on noise and sensitivity in an SS-OCT system rely on the configuration as shown in Figure 2.7, which is exemplary for the SS-OCT systems used in this work. The wavelength-swept source (SS, Micron Optics s3) with a wavelength range of $1260 - 1370$ nm and relative intensity noise $\mathrm{RIN_{dB}} = -100\ \mathrm{dB\,Hz^{-1}}$ at 2 MHz is connected to a fibre-based interferometer, consisting of two 3-dB couplers (CPL1,2). The first coupler CPL1 splits the light power from the source among the sample and the reference path. The sample path (SP) includes a free-space propagation section between fibre collimator (FC) and sample, and the reference path (RP) is completely fibre-based. Optical path lengths of RP and SP are considered to be matched. The second 3-dB coupler CPL2 acts as combiner and feeds the interfering light to both inputs of the balanced detector (BD, Thorlabs PDB430C), which

features a responsivity of $\rho = 1\ \mathrm{A/W}$, an optical noise-equivalent power $\mathrm{NEP} = 7\ \mathrm{pW}/\sqrt{\mathrm{Hz}}$, a common-mode rejection ratio (CMRR) of $\zeta = -25\ \mathrm{dB}$, and a transimpedance gain of $Z_\mathrm{a} = 5000\ \mathrm{V/A}$ for a $50\ \Omega$ load. Note that, for this device, the transimpedance gain is $Z_{\mathrm{a},0} = 1 \times 10^4\ \mathrm{V/A}$ for a load with a high input impedance. This number reduces by a factor of 2 for a $50\,\Omega$-load since the output resistance of the transimpedance amplifier also amounts to $50\,\Omega$. The NEP is defined by an optical input power

$$P_{\mathrm{opt,NEP}} = \mathrm{NEP}\sqrt{\Delta f_\mathrm{el}}\,, \tag{2.44}$$

which leads to a signal-to-noise ratio at the detector output of one, assuming an electrical measurement bandwidth Δf_el.

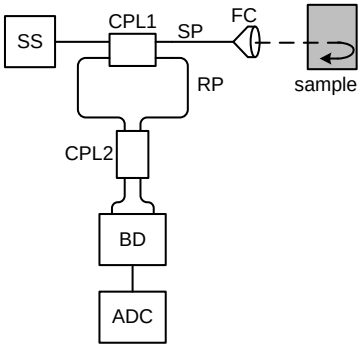

Figure 2.7: Swept-source OCT setup considered for sensitivity calculations. SS: swept-source laser (Micron Optics s3, 1260−1370 nm, $\mathrm{RIN} = 1 \times 10^{-10}\ 1/\mathrm{Hz}$), CPL1,2: 3-dB-coupler, SP: sample path, RP: reference path, FC: fibre collimator, BD: balanced detector (Thorlabs PDB430C, responsivity of $\rho = 1\ \mathrm{A/W}$, noise of $\mathrm{NEP} = 7\ \mathrm{pW}/\sqrt{\mathrm{Hz}}$, CMRR of $\zeta = -25$ dB and transimpedance gain of $Z_\mathrm{a} = 5000\ \mathrm{V/A}$ for a $50\ \Omega$ load), ADC: analogue-to-digital converter (Alazar ATS660, 16 bit, voltage step size $\delta u_\mathrm{q} = 392\ \mu\mathrm{V}$).

The difference signal of the BD is digitized by an analogue-to-digital converter (ADC, Alazar ATS660) with 16 bit resolution and a voltage step size of $\delta u_\mathrm{q} = 392\ \mu\mathrm{V}$ in the low-noise operating mode, corresponding to an effective number of 12 bits. The polarizations of the light from the RP and SP are assumed to match and are hence not regarded explicitly. Deflection and

focussing optics in the sample path are neglected. The sample power reflectivity $R_s(z) = r_s^2(z)$ is the squared sample field reflectivity and is defined by the backscattering into the fibre-optic system, thus including coupling losses into the optical system.

Using this setup configuration, the following section introduces the concept of balanced detection and evaluates the impact of the different noise contributions on the overall SNR. As will be shown in this section, highest sensitivity, allowing measurements of lowest sample reflections, is only achieved with this system using rather low reference path powers, when RIN contributions from the light of the reference path are small. This situation can be different for sources with low RIN or for perfect balancing over all wavelengths. Real systems, however, make this comprehensive noise consideration necessary. In contrast, reaching the maximum SNR and thus exploiting the dynamic range of the system is shown to be possible with higher sample path powers and with rather relaxed constraints to the reference path power.

A technical solution to reduce noise and to remove constant parts in a signal is balanced detection. The following section briefly introduces this concept and points out its benefits. A balanced detector (BD) comprises two photodiodes PD1 and PD2 connected electrically antiparallel, as well as a transimpedance amplifier (TIA), see Figure 2.8. The fields $\underline{E}_{r,0} = \sqrt{2}\underline{E}_r$, $\underline{E}_{s,0} = -j\sqrt{2}\underline{E}_s$ returning from reference and sample path, respectively, in front of the combining coupler, are denoted with pre-factors of $\sqrt{2}$, $-j\sqrt{2}$, since $\underline{E}_r$ and $\underline{E}_s$ are defined as the respective fields after the coupler (CPL2) and in front of PD1. The photodiodes PD1,2 generate the respective photocurrents $i_{d1,2}$ from the respective electric fields $\underline{E}_{d1}$ and $\underline{E}_{d2}$ entering the photodiodes. Due to the antiparallel connection of both photodiodes (PD1,2), the difference current $i_{sig,BD} \approx i_{d1} - i_{d2}$ can be tapped and amplified by a transimpedance amplifier (TIA) with real-valued transimpedance gain Z_a, leading to the output voltage

$$u_{sig,BD} = -Z_a \, i_{sig,BD}. \tag{2.45}$$

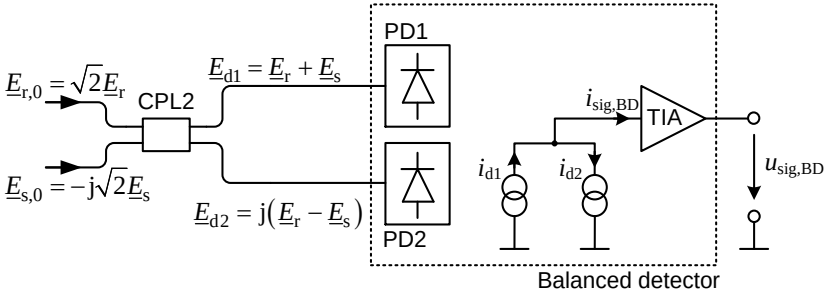

Figure 2.8: Balanced detection concept with coupler (CPL2) and balanced detector. The input fields $\underline{E}_{r,0} = \sqrt{2}\underline{E}_r$ and $\underline{E}_{s,0} = -j\sqrt{2}\underline{E}_s$ come from reference and sample path, respectively. A balanced detector comprises two photodiodes (PD1,2) connected electrically antiparallel, and a transimpedance amplifier (TIA). The photodiodes PD1,2 generate the respective photocurrents $i_{d1,2}$. In comparison to detection of the signal at one port of the interferometer, both ports with the respective electric input fields $\underline{E}_{d1}$ and $\underline{E}_{d2}$ are converted into currents. The antiparallel connection of both photodiodes (PD1,2) leads to a difference current $i_{sig,BD} \approx i_{d1} - i_{d2}$ at the TIA input and to a voltage $u_{sig,BD} = -Z_a i_{sig,BD}$ at the output of the TIA.

The optical fields on both ports

$$\begin{aligned} \underline{E}_{d1} &= \underline{E}_r + \underline{E}_s, \\ \underline{E}_{d2} &= j(\underline{E}_r - \underline{E}_s) \end{aligned} \tag{2.46}$$

are a superposition of the fields from sample and reference path. The photodiode currents are proportional to the squared absolute values of the respective electric fields $|\underline{E}_{d1}|^2$, $|\underline{E}_{d2}|^2$, which are calculated as

$$\begin{aligned} i_{d1} &\sim \overline{|\underline{E}_{d1}|^2} = \overline{|\underline{E}_r|^2} + \overline{|\underline{E}_s|^2} + 2\,\mathrm{Re}\left\{\overline{\underline{E}_r^* \underline{E}_s}\right\} \\ i_{d2} &\sim \overline{|\underline{E}_{d2}|^2} = \overline{|\underline{E}_r|^2} + \overline{|\underline{E}_s|^2} - 2\,\mathrm{Re}\left\{\overline{\underline{E}_r^* \underline{E}_s}\right\}. \end{aligned} \tag{2.47}$$

With the respective optical powers $P_r, P_s,$ arriving from reference and sample path, and measured in front of each of the photodetectors, for optimum coherence ($\kappa_L(\tau_r - t_s) = 1$), and for a single reflection in the sample path, which leads to a phase difference of $\Delta\varphi = \omega_0(\tau_r - t_s)$ at the optical angular frequency ω_0, see Eq. (2.14), the photodiode currents in Eq. (2.47) can be expressed as

$$\begin{aligned} i_{\mathrm{d1}} &= \rho\left(P_{\mathrm{r}} + P_{\mathrm{s}} + 2\sqrt{P_{\mathrm{r}}P_{\mathrm{s}}}\cos\left(\Delta\varphi\right)\right), \\ i_{\mathrm{d2}} &= \rho\left(P_{\mathrm{r}} + P_{\mathrm{s}} - 2\sqrt{P_{\mathrm{r}}P_{\mathrm{s}}}\cos\left(\Delta\varphi\right)\right). \end{aligned} \tag{2.48}$$

The subtraction in the balanced detector leads to a rejection of signal parts, which arrive with equal power on both detector inputs. Depending on the coupling ratio of the coupler and on the similarity of the photodiodes the rejection is not perfect but can be described by a common-mode rejection ratio (CMRR) ζ of the electrical signal powers. Using the CMRR, the signal current after balanced detection can be expressed as

$$\begin{aligned} i_{\mathrm{sig,BD}} &= i_{\mathrm{d1}} - i_{\mathrm{d2}} + \sqrt{\zeta}\left(i_{\mathrm{d1}} + i_{\mathrm{d2}}\right) \\ &\approx i_{\mathrm{d1}} - i_{\mathrm{d2}} \end{aligned} \tag{2.49}$$

and can thus be described by the difference of the individual photodiode currents i_{d1} and i_{d2}, plus a small not-suppressed additive part $\sqrt{\zeta}\left(i_{\mathrm{d1}} + i_{\mathrm{d2}}\right)$. This analysis concentrates on the calculation of the OCT signal current $i_{\mathrm{sig,BD}}$ after balanced detection, while noise contributions will be treated separately. Inserting Eq. (2.47) or (2.48) into Eq. (2.49) leads to

$$\begin{aligned} i_{\mathrm{sig,BD}} &\sim 4\,\mathrm{Re}\left\{\overline{\underline{E}_{\mathrm{r}}^{*}\underline{E}_{\mathrm{s}}}\right\} + 2\sqrt{\zeta}\left(\overline{\left|\underline{E}_{\mathrm{r}}\right|^{2}} + \overline{\left|\underline{E}_{\mathrm{s}}\right|^{2}}\right) \\ i_{\mathrm{sig,BD}} &= \rho\left(4\sqrt{P_{\mathrm{r}}P_{\mathrm{s}}}\cos\left(\Delta\varphi\right) + 2\sqrt{\zeta}\left(P_{\mathrm{r}} + P_{\mathrm{s}}\right)\right), \end{aligned} \tag{2.50}$$

where ρ denotes the responsivity of the photodetector. This shows the advantage of balanced detection in OCT systems: The sample-reference interference term $\mathrm{Re}\left\{\overline{\underline{E}_{\mathrm{r}}^{*}\underline{E}_{\mathrm{s}}}\right\}$ remains strong, while the parts that do not contain information on the depth-dependent reflectivity of the sample are attenuated.

For quantification of the dynamic properties of OCT measurements, three terms need to be defined: First, sensitivity is defined as a system property, expressed in sample power reflectivity. The sensitivity quantifies the lowest measurable reflectivity of a sample and is linked to the noise floor of the measurement system in case the measurement signal is weak enough to not raise the noise floor itself, e.g., as a result of RIN. Second, the signal-to-noise ratio (SNR) relates the signal power level to the level of the noise floor. Third,

the dynamic range (DR) is a system property, describing the maximum achievable SNR. Usually, the DR is smaller than the total range of measurable signal strengths. The range of measurable signal strengths is limited on the lower side by the sensitivity and on the upper side by the smallest individual saturation value of a system component. Typically, ADC input range or photodetector saturation define the upper limit. By variation of the reference arm power, the DR can be shifted inside the total range, see Figure 2.9 (a).

The lower limit of the measurement range is defined by the noise level. For a quantitative description, the following section is dedicated to an analysis of the individual noise terms in swept-source OCT systems. Figure 2.9 (b) shows the origin of the most prominent noise types in OCT: Relative intensity noise (RIN) from the swept source (SS), shot noise arising from the corpuscular nature of light, thermal noise from the amplification circuits in detector and ADC, and quantization noise from the digitization process in the ADC.

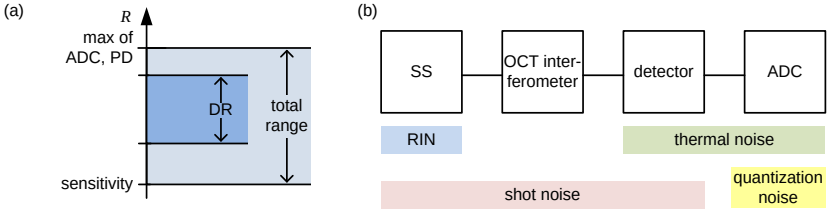

Figure 2.9: Sensitivity, dynamic range and noise sources in an OCT system. (a) Definition: sensitivity, dynamic range (DR), and total range. The total possible range of a measurement signal (expressed in sample power reflectivity *R*, light blue) is limited on the lower side by the sensitivity of the system and on the upper side by the saturation values of the individual system components like ADC or PD. The dynamic range (DR, dark blue) is within this range and typically smaller. By variation of the reference arm power, the DR can be shifted within the total range. (b) Origin of the different noise sources in an OCT system: Relative intensity noise (RIN) from the frequency-swept source (SS), shot noise arising from the corpuscular nature of light, thermal noise from the amplification circuits in detector, and ADC, as well as quantization noise in the ADC.

Relative intensity noise (RIN) describes noise originating from intensity fluctuations of a laser diode [46]. In swept-source lasers, these fluctuations do not

only come from random phase noise as in conventional continuous-wave lasers. Instead, longitudinal mode hopping and gain competition between different longitudinal modes happen during the fast wavelength sweep and contribute to the RIN [47]. RIN relates the intensity fluctuations to the average intensity and can be expressed as [44]

$$\mathrm{RIN}_{\mathrm{tot}} = \int_0^\infty \mathrm{RIN}(f)\,\mathrm{d}f = \frac{\overline{\delta P_0^2(t)}}{\overline{P_0}^2}, \tag{2.51}$$

with the one-sided power spectrum $\mathrm{RIN}(f)$, which can be determined by a spectral analysis of the photocurrent in the baseband. To this end, the temporal fluctuations of the laser power are detected by a photodiode and spectrally analysed by an electrical spectrum analyzer. The spectral $\mathrm{RIN}(f)$ is specified in units of Hz^{-1}. The optical output power is given by P_0, and $\delta P_0(t) = P_0(t) - \overline{P_0(t)}$ defines the mean-free power fluctuations over time *t*.

In the following, we assume that with small electrical frequency ranges, the relative intensity noise spectrum is independent of the frequency, thus $\mathrm{RIN}(f) = \mathrm{RIN}$. If RIN is known by measurement, the resulting second moment of the noise current

$$\overline{|i_{\mathrm{RIN}}|^2} = \rho^2\ \mathrm{RIN}\ P_{\mathrm{d}}^2\ \Delta f_{\mathrm{el}} \tag{2.52}$$

is given by multiplication of the RIN with the optical power P_{d} on the photodetector, with the measurement bandwidth Δf_{el}, and with the detector responsivity ρ. Expressed in signal current $i_{\mathrm{d}} = \rho P_{\mathrm{d}}$ the relation follows as

$$\overline{|i_{\mathrm{RIN}}|^2} = \mathrm{RIN}\ i_{\mathrm{d}}^2\ \Delta f_{\mathrm{el}}. \tag{2.53}$$

Shot noise is inherent in photon generation and detection systems and arises from the discrete random arrival times of the individual photons at the detector. As a result, the generated photocurrent shows random fluctuations. Shot noise is a Poisson process and follows the Poisson distribution [44]. The resulting noise current can be expressed with its time averaged second central moment as

$$\overline{|i_{\mathrm{sh}}|^2} = 2q_0\bar{i}_{\mathrm{d}}\Delta f_{\mathrm{el}}, \tag{2.54}$$

with the elementary charge q_0, the average photocurrent $\bar{i}_{\mathrm{d}}$ and the measurement bandwidth Δf_{el}. The average noise power is proportional to the signal current, which is in accordance with the fact that the expectation value of a Poisson distribution equals its variance.

Detector noise comprises thermal noise originating from the detector electronics. Often detector noise is specified in noise-equivalent power (NEP), see Eq. (2.44), expressing an assumed optical input power, which leads to a detector output current with an SNR of one in the electrical bandwidth of 1 Hz. With the general expression for the photocurrent $i_{\mathrm{d}} = \rho P_{\mathrm{opt}}$, dependent on detector responsivity ρ and optical input power P_{opt}, the averaged second central moment of the detector noise current inside the measurement bandwidth Δf_{el} can be expressed as

$$\overline{|i_{\mathrm{dn}}|^2} = \rho^2 \mathrm{NEP}^2 \Delta f_{\mathrm{el}}. \tag{2.55}$$

Quantization noise has its origin in the assignment of discrete quantization levels to the analogue input signal with continuous values. Although, strictly speaking, quantization is not a random process, the quantization error can be described by stochastic means and is part of this investigation. Dependent on the step size, the quantization error can be larger or smaller. This error is equally distributed within one voltage step δu_{q} [48]. Because of the uniformly distributed quantization error n_{q}, this results in a central second moment of the quantization error of[1]

[1] The quantized signal $u_{\mathrm{q}} = u_0 + n_{\mathrm{q}}$ differs from the input signal u_0 by the equally distributed quantization error $n_{\mathrm{q}} \in \left[-\delta u_{\mathrm{q}}/2,\ \ \delta u_{\mathrm{q}}/2\right]$. Accordingly, the probability density function inside the interval is $p_{\mathrm{q}} = 1/\delta u_{\mathrm{q}}$. The central second moment (variance) of the mean-free quantization error is then calculated to be

$$\overline{\left|\overline{n_{\mathrm{q}}} - n_{\mathrm{q}}\right|^2} = \overline{\left|n_{\mathrm{q}}\right|^2} = \int_{-\delta u_{\mathrm{q}}/2}^{\delta u_{\mathrm{q}}/2} n_{\mathrm{q}}^2\, p_{\mathrm{q}}\,\mathrm{d}n_{\mathrm{q}} = \frac{1}{\delta u_{\mathrm{q}}}\left[\frac{1}{3}n_{\mathrm{q}}^3\right]_{-\delta u_{\mathrm{q}}/2}^{\delta u_{\mathrm{q}}/2} = \frac{1}{3\delta u_{\mathrm{q}}}\left(\frac{\delta u_{\mathrm{q}}^3}{8} + \frac{\delta u_{\mathrm{q}}^3}{8}\right) = \frac{\delta u_{\mathrm{q}}^2}{12}.$$

$$\overline{\left|n_{\mathrm{q}}\right|^2} = \frac{\delta u_{\mathrm{q}}^2}{12} \,. \tag{2.56}$$

For ease of comparison to other noise sources, the quantization error in voltages, n_{q}, is expressed as it was an effective photocurrent $i_{\mathrm{q}} = n_{\mathrm{q}} / Z_{\mathrm{a}}$, using the real-valued transimpedance Z_{a} of the transimpedance amplifier. The resulting central second moment of the equivalent noise current is then given by

$$\overline{\left|i_{\mathrm{q}}\right|^2} = \frac{\delta u_{\mathrm{q}}^2}{12 Z_{\mathrm{a}}^2} . \tag{2.57}$$

In the following, all noise contributions are determined for the case of balanced detection.

In order to calculate the relative intensity noise contributions of the different signal currents arising from interference of sample path with sample path reflections (subscript SS), reference path with reference path reflections (subscript RR), and sample path with reference path reflections (subscript SR), the signal current in Eq. (2.50) is rephrased to

$$i_{\mathrm{sig,BD}} = \underbrace{2\rho\sqrt{\zeta}P_{\mathrm{s}}}_{i_{\mathrm{SS}}} + \underbrace{2\rho\sqrt{\zeta}P_{\mathrm{r}}}_{i_{\mathrm{RR}}} + \underbrace{4\rho\sqrt{P_{\mathrm{r}}P_{\mathrm{s}}}\cos\left(\Delta\varphi\right)}_{i_{\mathrm{SR}}} . \tag{2.58}$$

The corresponding second moments of the RIN-related noise currents are derived from Eq. (2.53)

$$\begin{aligned}
\overline{\left|i_{\mathrm{RIN,SS}}\right|^2} &= \mathrm{RIN}\; i_{\mathrm{SS}}^2\; \Delta f_{\mathrm{el}} = 4\rho^2\; \mathrm{RIN}\; \zeta P_{\mathrm{s}}^2 \Delta f_{\mathrm{el}} \\
\overline{\left|i_{\mathrm{RIN,RR}}\right|^2} &= \mathrm{RIN}\; i_{\mathrm{RR}}^2\; \Delta f_{\mathrm{el}} = 4\rho^2\; \mathrm{RIN}\; \zeta P_{\mathrm{r}}^2 \Delta f_{\mathrm{el}} \\
\overline{\left|i_{\mathrm{RIN,SR}}\right|^2} &= \mathrm{RIN}\; i_{\mathrm{SR}}^2\; \Delta f_{\mathrm{el}} = 16\rho^2\; \mathrm{RIN}\; P_{\mathrm{r}} P_{\mathrm{s}} \Delta f_{\mathrm{el}} \cos^2\left(\Delta\varphi\right)
\end{aligned} \tag{2.59}$$

and sum up to the overall second moment of the electrical RIN

$$\begin{aligned}\overline{\left|i_{\mathrm{RIN}}\right|^2} &= \overline{\left|i_{\mathrm{RIN,SS}}\right|^2} + \overline{\left|i_{\mathrm{RIN,RR}}\right|^2} + \overline{\left|i_{\mathrm{RIN,SR}}\right|^2} \\ &= 4\rho^2 \mathrm{RIN}\left[\zeta\left(P_\mathrm{s}^2 + P_\mathrm{r}^2\right) + 4P_\mathrm{r}P_\mathrm{s}\cos^2\left(\Delta\varphi\right)\right]\Delta f_\mathrm{el}.\end{aligned} \tag{2.60}$$

The second moment of the total RIN current is thus dependent on the optical powers returning from both reference and sample arm, however, for perfectly balanced detectors, only the mixing product of $P_\mathrm{r}P_\mathrm{s}$ plays a significant role. For typical detectors with $\zeta > 0$, the total RIN current also depends on the individual return powers and on ζ. In most cases, in OCT, the reference arm returns a higher optical power level than the sample arm, thus the strong reference-reference RIN contribution in the measurement signal can be suppressed by choosing a well-balanced combiner (CPL2 in Figure 2.8) and balanced detector such that they provide a good common-mode rejection (small ζ).

The shot noise, see Eq. (2.54), of both photodiodes can be expressed as

$$\begin{aligned}\overline{\left|i_{\mathrm{sh},1}\right|^2} &= 2q_0\overline{i_{\mathrm{d1}}}\Delta f_\mathrm{el} = 2q_0\rho\left(P_\mathrm{r} + P_\mathrm{s} + 2\sqrt{P_\mathrm{r}P_\mathrm{s}}\cos\left(\Delta\varphi\right)\right)\Delta f_\mathrm{el} \\ \overline{\left|i_{\mathrm{sh},2}\right|^2} &= 2q_0\overline{i_{\mathrm{d2}}}\Delta f_\mathrm{el} = 2q_0\rho\left(P_\mathrm{r} + P_\mathrm{s} - 2\sqrt{P_\mathrm{r}P_\mathrm{s}}\cos\left(\Delta\varphi\right)\right)\Delta f_\mathrm{el}\end{aligned} \tag{2.61}$$

and adds up in noise power, as both noise sources are independent,

$$\overline{\left|i_{\mathrm{sh}}\right|^2} = \overline{\left|i_{\mathrm{sh},1}\right|^2} + \overline{\left|i_{\mathrm{sh},2}\right|^2} = 4\,q_0\rho\left(P_\mathrm{s} + P_\mathrm{r}\right)\Delta f_\mathrm{el}. \tag{2.62}$$

In the OCT measurement, the variances of all noise currents add up to a total noise current variance

$$\begin{aligned}\overline{\left|i_\mathrm{n}\right|^2} &= \overline{\left|i_\mathrm{q}\right|^2} + \overline{\left|i_\mathrm{dn}\right|^2} + \overline{\left|i_\mathrm{sh}\right|^2} + \overline{\left|i_\mathrm{RIN}\right|^2} \\ &= \frac{\delta u_\mathrm{q}^2}{12Z_\mathrm{a}^2} + \rho^2\mathrm{NEP}^2\Delta f_\mathrm{el} + 4q_0\rho\left(P_\mathrm{s} + P_\mathrm{r}\right)\Delta f_\mathrm{el} \\ &\quad + 4\rho^2\mathrm{RIN}\left[\zeta\left(P_\mathrm{s}^2 + P_\mathrm{r}^2\right) + 4P_\mathrm{s}P_\mathrm{r}\cos^2\left(\Delta\varphi\right)\right]\Delta f_\mathrm{el}.\end{aligned} \tag{2.63}$$

In analogy to the noise power, the photocurrent signal power can also be expressed dependent on the incident optical powers returning from sample arm and reference arm. Using Eq. (2.50) for the case of full coherence

$\kappa_L(\tau_r - t_s) = 1$ between reference path light and light returning from one single sample reflection, as well as assuming perfect common-mode rejection ($\zeta = 0$) leads to a balanced signal current of

$$i_{sig,BD} = 4\rho\sqrt{P_s P_r}\cos(\Delta\varphi). \tag{2.64}$$

For comparison to noise powers, the mean of the squared signal photocurrent is calculated to

$$\overline{i_{sig,BD}^2} = \left(4\rho\sqrt{P_s P_r}\cos(\Delta\varphi)\right)^2 = 16\rho^2 P_s P_r \cos^2(\Delta\varphi). \tag{2.65}$$

This signal current is amplified by the transimpedance amplifier, see Figure 2.8 and Eq. (2.45). For the calculation of the signal level, the upper signal limit of the transimpedance amplifier inside the photodetector and the limit of the ADC need to be taken into account. In the specific setup discussed in this work, the amplifier of the photodetector saturates at $u_{max,PD} = \pm 1.8\ \mathrm{V}$ output voltage, and the ADC is limited at $u_{max,ADC} = \pm 0.5\ \mathrm{V}$ when operated in the low-noise amplifier-bypass mode. The lower of these limits ($u_{max,ADC}$) causes a corresponding maximum measurable photocurrent $i_{max} = u_{max,ADC}/Z_a$, which limits the photocurrent to

$$\overline{i_{sig,lim}} = \min\left\{i_{sig,BD},\ i_{max}\right\}. \tag{2.66}$$

This limitation is usually not important for moderate sample and reference arm powers, but plays a role when strongly reflecting elements are placed into the beam at perpendicular incidence and thus lead to strong sample arm return power. To keep the signal level below the saturation limit, either the transimpedance gain Z_a is reduced or an additional electrical attenuation is used.

In the following, signal and noise contributions are evaluated basing on the aforementioned models and for the fibre-based SS-OCT system discussed in this work. Polarization effects are neglected and optimum coherence is assumed. Figure 2.10 shows the OCT signal and the various noise contributions as a function of reference arm power, when the sample reflectivity $R_s = -50\ \mathrm{dB}$ is low. The vertical axis represents the mean squared photocurrents on a logarithmic scale. The sample power of $P_s = 1.4\ \mathrm{nW}$ incident on the

photodetectors is derived from the output power of the swept source of 10 mW (+10 dBm), less 3 dB for the power split at each of the three passes through a coupler (CPL1 forward, CPL1 reverse and CPL2), less 50 dB at the sample, see Figure 2.7 for a sketch of the setup. Finally, the sample return power is subject to additional 9.5 dB measured coupling loss in the free-space optics part. The responsivity of the photodetector is $\rho = 1\ \mathrm{A/W}$. The electrical signal power (black solid line) increases linearly with reference arm power, see Eq. (2.65). The ADC is not yet saturated at a sample arm reflectivity of $-50\ \mathrm{dB}$ and for the reference arm powers investigated here. Quantization noise (brown curve) and detector noise (green curve) stay constant versus reference arm power and are calculated using Eqs. (2.57) and (2.55), assuming an ADC voltage step size of $\delta u_\mathrm{q} = 392\ \mu\mathrm{V}$. The photodetector is specified with noise-equivalent power $\mathrm{NEP} = 7\,\mathrm{pW}/\sqrt{\mathrm{Hz}}$, CMRR of $\zeta = -25\ \mathrm{dB}$ and transimpedance gain of $Z_\mathrm{a} = 5000\ \mathrm{V/A}$ at a $50\ \Omega$ load. The detection bandwidth is limited by an anti-aliasing filter to $\Delta f_\mathrm{el} = 2\ \mathrm{MHz}$. Shot noise power, Eq. (2.62), increases linearly with reference arm power (red curve), and thus stays in a certain fixed ratio to the signal power. The laser RIN amounts to $1\times10^{-10}\ 1/\mathrm{Hz}$ at $f = 2\ \mathrm{MHz}$, and because of the limited CMRR and the weak sample arm return power, the P_r^2 term in Eq. (2.60) dominates the shape of the RIN curve (blue), which is thus quadratically dependent on the reference arm power. In total, all noise contributions sum up, Eq. (2.63), and are displayed as the black dashed curve, limited by quantization noise for low reference arm powers and by RIN for medium and high powers.

The total noise is lowest for weak reference arm powers, however, at this point the measurement signal is weak as well. In order to find an optimum operating point of the system, the signal-to-noise ratio is calculated according to

$$\mathrm{SNR} = \frac{\overline{i_{\mathrm{sig,lim}}^2}}{\overline{|i_\mathrm{n}|^2}} \frac{M}{2}, \tag{2.67}$$

given by the ratio of averaged signal power $\overline{i_{\mathrm{sig,lim}}^2} \le i_\mathrm{max}$ and averaged noise power $\overline{|i_\mathrm{n}|^2}$. Since the OCT signal is Fourier transformed by a *M*-point DFT,

the actual noise bandwidth is $\Delta f/(M/2)$, thus decreasing the noise power by a factor of $M/2$, compare [30].

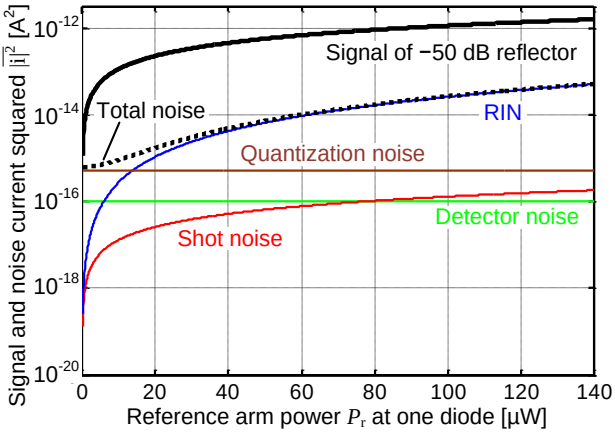

Figure 2.10: Comparison of the OCT signal power and various noise contributions versus reference arm power. All numbers are calculated for the specific fibre-based OCT system in Figure 2.7. Micron Optics SS with $\mathrm{RIN} = 1\times10^{-10}$ 1/Hz at $f = 2$ MHz; balanced photodetector with responsivity of $\rho = 1$ A/W, noise of $\mathrm{NEP} = 7\,\mathrm{pW}/\sqrt{\mathrm{Hz}}$, CMRR of $\zeta = -25$ dB and transimpedance gain of $Z_a = 5000$ V/A at 50 Ω load; the ADC voltage step size amounts to $\delta u_q = 392$ µV. The detection bandwidth is limited by an anti-aliasing filter to $\Delta f_{el} = 2$ MHz. The sample offers a reflectivity of $R_S = -50$ dB, leading to a sample arm power on one photodiode of $P_s = 1.4$ nW. The signal power (solid black) increases linearly with reference arm power and is plotted for a −50 dB reflector in the sample arm. Quantization noise (brown curve) and detector noise (green) are not dependent on the reference arm power. Shot noise (red) increases linearly with reference arm power (axis in log scale) and the RIN (blue) increases quadratically. The total noise (dashed black) is limited by quantization noise and RIN.

Besides noise currents and SNR, the minimum measurable sample reflectivity R_n is of interest. This quantity is equivalent to the noise floor at given sample and reference arm return powers and is expressed in terms of sample reflectivities. At given sample reflectivity R_S of a first reflector, a certain SNR results, due to signal power dependent noise contributions. Thus, the minimum measurable sample reflectivity of a second reflector is given by

$$R_{\mathrm{n}} = \frac{R_{\mathrm{S}}}{\mathrm{SNR}}. \tag{2.68}$$

This specification would be unnecessary, if the noise floor would be independent of the sample reflectivity, however, shot noise and RIN depend on received optical power and make this definition essential.

The sensitivity S of the OCT system is defined as the minimum measurable sample reflectivity R_{n}, at optimum sample and reference arm return powers,

$$S = \min\left\{R_{\mathrm{n}}\right\}. \tag{2.69}$$

Both noise floor R_{n} and SNR are analysed in their dependence on sample and reference arm powers, see Figure 2.11. In Figure 2.11 (a), the colour-coded minimum measurable sample reflectivity R_{n} (noise floor) in dB-units is plotted versus reference arm power P_{r} (horizontal axis) and versus sample reflectivity R_{S} (vertical axis). The respective sample arm power P_{S} on one photodiode is plotted as second vertical axis. The sensitivity of the system of $S = -100$ dB is achieved for 16 µW reference arm power and sample arm reflectivities below −45 dB. At higher reference arm powers and especially at higher sample arm powers the noise level increases. The SNR of the OCT signal is given in Figure 2.11 (b) in colour-coded dB-units for varying sample and reference arm powers, denoted on vertical and horizontal axes, respectively. The SNR increases with sample arm power, when RIN from the reference arm is negligible and the ADC is not saturated. The SNR reaches a plateau at a maximum of 66 dB, defining the dynamic range (DR) of the system.

Figure 2.11 (c-e) show the impact of all different noise contributions on the total noise floor R_{n} in sample reflectivity units: The noise floor of the system is calculated in total and plotted together with the individual contributions of the various noise sources. Three specific sample reflectivities R_{S} of -50 dB, -30 dB and 0 dB are considered, see Figure 2.11 (c), (d) and (e), respectively.

At low and medium sample reflectivities, Figure 2.11 (c) and (d), quantization noise (brown curve) and detector noise (green) are constant. However, the

signal power increases with reference arm power, so the contribution of quantization noise and detector noise to the noise floor, expressed in sample reflectivity, decreases. At high sample reflectivities, Figure 2.11 (e), and above a reference path return power of $P_r = 9\ \mu W$, the TIA gain needs to be reduced with increasing reference arm power, to avoid ADC saturation. This reduces thermal noise, whereas quantization noise stays constant.

For a given sample reflectivity, the shot noise increases linearly with reference arm power, and the same is true for the signal power. The influence of shot noise on the noise floor in sample reflectivity hence stays constant as long as the ADC is not saturated. The situation is different for strong sample arm powers, Figure 2.11 (e), where the shot noise is not dominated by the reference arm power anymore. In the regime of low reference arm powers, the squared sample arm power P_s^2 dominates the shot noise, leading to a shot noise contribution which decays with increasing reference arm power, as the signal power $\sim P_s P_r$ increases.

In the investigated setup, in most cases, RIN dominates the noise. For low and medium sample reflectivities, Figure 2.11 (c, d), RIN increases quadratically with reference arm power P_r, while the signal power increases linearly with P_r. As a consequence, the noise floor expressed in sample reflectivity units increases with the reference arm power. For high sample reflectivities, see Figure 2.11 (e) and Eq. (2.60), RIN increases linearly with P_r, and the same is true for the signal power, compare Eq. (2.65). The noise floor expressed in sample reflectivity units is hence independent of the reference arm power.

The noise floor expressed in sample reflectivity units is lowest for reference arm powers of around $P_r = 16\ \mu W$, leading to the sensitivity of $S = R_n = -100\ dB$ for a sample reflectivity of $R_S = -50\ dB$, see Figure 2.11 (c). For a sample reflectivity of $R_S = -30\ dB$, Figure 2.11 (d), a noise floor of $R_n = -95\ dB$ can be achieved. At a strong sample reflectivity of $R_S = 0\ dB$, Figure 2.11 (e), the minimum noise floor is $R_n = -66\ dB$.

A challenge in an OCT measurement is to reach both good sensitivity values and high SNR. Both goals can be achieved at a moderate reference arm power

around $P_r = 16\ \mu W$ on each photodiode. In this case, weakly reflecting samples make OCT operation at the sensitivity limit possible, and strongly reflecting samples with $R_S > -25\ dB$ still exploit the entire dynamic range of the system.

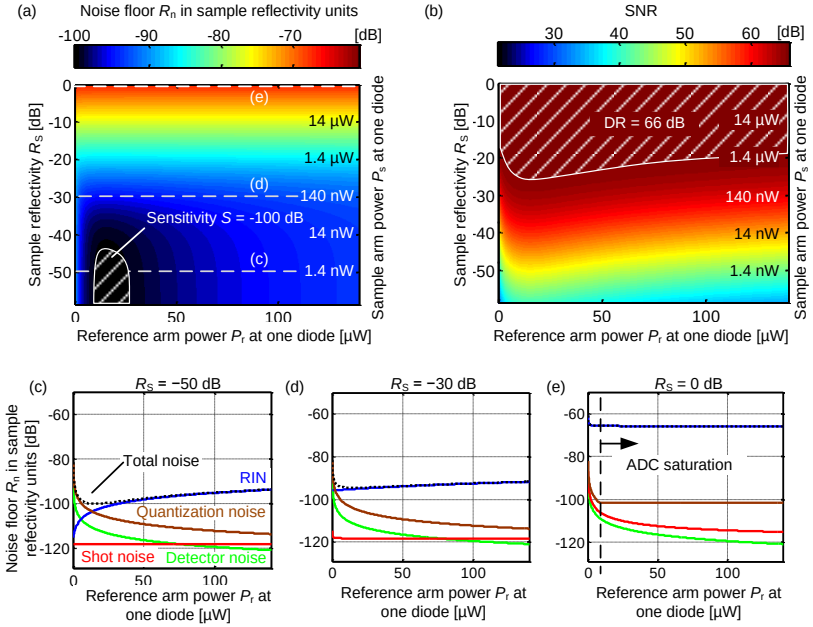

Figure 2.11: Minimum measurable sample reflectivity (noise floor) R_n and signal-to-noise ratio (SNR) of the exemplary OCT system in Figure 2.7. **(a)** Colour-coded noise floor R_n of the OCT system. The horizontal axis denotes the reference arm power P_r incident on each photodiode, and the vertical axes refer to sample reflectivity R_S in dB units and the corresponding sample arm powers P_S on each photodiode. The sensitivity of $S = -100$ dB is achieved for $P_r = 16\ \mu W$ reference arm power and sample arm reflectivities R_S below −45 dB (shaded area). **(b)** The SNR increases with sample reflectivity and reaches a plateau at 66 dB for sample reflectivities above approximately −20 dB. This maximum SNR defines the dynamic range (DR) of the system (shaded area gives full DR at ADC saturation). **(c)** Noise floor R_n and individual contributions to the noise floor R_n in sample reflectivity units at a low sample reflectivity of $R_S = -50$ dB, plotted versus reference arm power. Quantization noise (brown line) and detector noise (green) have less influence with raising reference arm power, shot noise (red) stays

constant and the RIN influence increases linearly (note the log-scale on vertical axis). The total noise floor (black dashed) is limited by quantization noise at low reference arm powers and by RIN at high powers. A sensitivity of $S = R_n = -100$ dB is achieved for reference arm powers of $P_r = 16$ µW. **(d)** Noise floor R_n for sample arm reflectivity of $R_S = -30$ dB. The minimum measurable sample reflection is reduced to $R_n = -95$ dB. **(e)** Noise floor R_n for sample reflectivity of $R_S = 0$ dB. RIN dominates the noise floor at $R_n = -66$ dB. From the ADC saturation limit around $P_r = 9$ µW onwards, the signal is clamped to the maximum range, e.g. by dynamic reduction of the TIA gain Z_a or by electrical attenuation. Here, the shot noise is dominated by strong sample reflected light and with reduction of the TIA gain the shot noise contribution is reduced, like the contribution of the detector noise.

2.2 Polarization-sensitive optical coherence tomography

This section first introduces the optical polarization and the Jones and Stokes formalisms, which serve for polarization calculations. Then polarization-sensitive OCT (PS-OCT) is introduced, followed by its typical application fields. Finally, two system variants, one with free-space bulk optical elements and one with fibre-coupled components are presented. In the following section, the underlining of complex variables is omitted for better readability.

2.2.1 Polarization of light

Light propagates as electromagnetic wave and its physical properties are described by Maxwell's equations [49], linking the electric and magnetic field vectors $\vec{E}$, $\vec{H}$ to the electric displacement $\vec{D}$, the electric material polarization $\vec{P}$ and the magnetic induction $\vec{B}$. The current density and the space charge density are assumed to be zero. The vacuum permittivity is given by ε_0 and the magnetic permittivity by μ_0. The relative magnetic permittivity is here assumed to be $\mu_r = 1$ and the material is regarded as isotropic, linear and time-invariant. In the following, we assume complex sinusoidal time-domain quantities with the dependency $\vec{\Psi}(\vec{r},t) = \underline{\vec{\Psi}}(\vec{r},\omega)\mathrm{e}^{\mathrm{j}\omega t}$, where $\vec{\Psi}$ can be replaced by $\vec{E}, \vec{H}, \vec{D}, \vec{B}, \vec{P}$ and $\underline{\vec{\Psi}}$ can be replaced by $\underline{\vec{E}}, \underline{\vec{H}}, \underline{\vec{D}}, \underline{\vec{B}}, \underline{\vec{P}}$. The breve denotes the individual complex time-domain amplitudes. Accordingly, Maxwell's equations for the complex time-domain amplitudes $\underline{\vec{\Psi}}(\vec{r},\omega)$ are

$$\begin{aligned} \nabla\times\vec{\underline{H}}(\vec{r},\omega) &= \mathrm{j}\omega\vec{\underline{D}}(\vec{r},\omega) & \nabla\times\vec{\underline{E}}(\vec{r},\omega) &= -\mathrm{j}\omega\vec{\underline{B}}(\vec{r},\omega) \\ \nabla\cdot\vec{\underline{D}}(\vec{r},\omega) &= 0 & \nabla\cdot\vec{\underline{B}}(\vec{r},\omega) &= 0 \\ \vec{\underline{D}}(\vec{r},\omega) &= \varepsilon_0\vec{\underline{E}}(\vec{r},\omega)+\vec{\underline{P}}(\vec{r},\omega) & \vec{\underline{B}}(\vec{r},\omega) &= \mu_0\vec{\underline{H}}(\vec{r},\omega)\ . \end{aligned} \tag{2.70}$$

In linear media that are isotropic and homogeneous, the electric displacement $\vec{\underline{D}}(\vec{r},\omega)$ can be expressed by the relative permittivity $\varepsilon_\mathrm{r}(\omega)=n^2(\omega)$, leading to $\vec{\underline{D}}(\vec{r},\omega)=\varepsilon_0\varepsilon_\mathrm{r}(\omega)\vec{\underline{E}}(\vec{r},\omega)$, with the real-valued refractive index $n(\omega)$. From Maxwell's equations, Eq. (2.70), the wave equation for electromagnetic waves in homogeneous isotropic media can be derived,

$$\nabla^2\vec{\underline{E}}(\vec{r},\omega)=-n(\omega)^2k_0(\omega)^2\vec{\underline{E}}(\vec{r},\omega), \tag{2.71}$$

where $c_0=1/\sqrt{\varepsilon_0\mu_0}$ is the vacuum speed of light[2]. An analogue expression exists for the magnetic field $\vec{\underline{H}}(\vec{r},\omega)$. The wave equation can be solved by an equation describing the electric field of a wave, compare the scalar equation in Eq. (2.1),

$$\vec{E}(\vec{r},t)=\vec{\underline{E}}(\vec{r},\omega)\mathrm{e}^{\mathrm{j}\omega t}=\vec{A}\mathrm{e}^{\mathrm{j}\left(\omega t-\vec{k}\cdot\vec{r}\right)}, \tag{2.72}$$

with the complex *E*-field amplitude vector $\vec{A}=A_x\vec{e}_x+A_y\vec{e}_y+A_z\vec{e}_z$, the propagation direction $\vec{r}=x\vec{e}_x+y\vec{e}_y+z\vec{e}_z$, and the wave vector $\vec{k}=k_x\vec{e}_x+k_y\vec{e}_y+k_z\vec{e}_z$. This wave propagates as a transverse wave, and the

[2] Starting from $\nabla\times\vec{\underline{E}}(\vec{r},\omega)=-\mathrm{j}\omega\vec{\underline{B}}(\vec{r},\omega)$, and applying a $(\nabla\times)$-operator to both sides of the equation, results in $\nabla\times\left(\nabla\times\vec{\underline{E}}(\vec{r},\omega)\right)=\nabla\times\left(-\mathrm{j}\omega\vec{\underline{B}}(\vec{r},\omega)\right)$, which can be rephrased to $\nabla\left(\nabla\cdot\vec{\underline{E}}(\vec{r},\omega)\right)-\nabla^2\vec{\underline{E}}(\vec{r},\omega)=-\mathrm{j}\omega\mu_0\left(\nabla\times\vec{\underline{H}}\right)$. With no space charge, and in isotropic and homogeneous media $\nabla\cdot\vec{\underline{D}}(\vec{r},\omega)=\varepsilon_0\varepsilon_\mathrm{r}(\omega)\nabla\cdot\vec{\underline{E}}(\vec{r},\omega)=0$ holds. Further, $\nabla\times\vec{\underline{H}}(\vec{r},\omega)=\mathrm{j}\omega\vec{\underline{D}}(\vec{r},\omega)$ and $\vec{\underline{D}}(\vec{r},\omega)=\varepsilon_0\varepsilon_\mathrm{r}(\omega)\vec{\underline{E}}(\vec{r},\omega)$ lead to $-\nabla^2\vec{\underline{E}}(\vec{r},\omega)=\omega^2\mu_0\varepsilon_0\varepsilon_\mathrm{r}(\omega)\vec{\underline{E}}(\vec{r},\omega)$ or, with $k_0(\omega)=\dfrac{\omega}{c_0}$ and $c_0=1/\sqrt{\varepsilon_0\mu_0}$, is rephrased to the wave equation $\nabla^2\vec{\underline{E}}(\vec{r},\omega)=-n(\omega)^2k_0(\omega)^2\vec{\underline{E}}(\vec{r},\omega)$.

direction of its oscillation can be defined within a plane perpendicular to the direction of propagation [50] and is referred to as polarization[3].

The Jones and the Stokes formalism are conventional approaches for describing the state of polarization of a light wave. This description includes changes of the state of polarization, which are induced by optical elements. In theory, both calculi could be applied for describing an optical non-depolarizing system, however in practice each of them is advantageous in different situations [51]. The Stokes formalism is able to handle depolarized light, while the Jones formalism cannot. Stokes vectors are based on a series of intensity measurements after certain polarization-optical elements, Jones vectors calculate from electromagnetic theory. A graphical representation of the Stokes parameters is the Poincaré sphere. However, only the Jones calculus allows direct access to the optical phase.

The Jones vector $\vec{J}$ is normalized, $\vec{J}\cdot\vec{J}^{*}=1$, and describes any fully polarized electric field that consists of two complex field amplitudes oriented along the *x* and *y*-direction, having a common phase δ, a phase difference 2φ, and amplitudes $\cos(\alpha), \sin(\alpha)$,

$$\vec{J}=\begin{pmatrix} J_x \\ J_y \end{pmatrix}=\mathrm{e}^{\mathrm{j}\delta}\begin{pmatrix} \mathrm{e}^{-\mathrm{j}\varphi}\cos(\alpha) \\ \mathrm{e}^{+\mathrm{j}\varphi}\sin(\alpha) \end{pmatrix}. \tag{2.73}$$

With the help of the Jones vector and its components J_x, J_y, and the scalar electric field amplitude *A*, any fully polarized plane wave, here propagating in *z*-direction, can be expressed as

---

[3] With $\nabla\cdot\underline{\vec{D}}(\vec{r},\omega)=0$, and thus $\nabla\cdot\underline{\vec{E}}(\vec{r},\omega)=0$, it follows that $\frac{\partial}{\partial x}A_x\mathrm{e}^{\mathrm{j}(\omega t-k_x x)}+\frac{\partial}{\partial y}A_y\mathrm{e}^{\mathrm{j}(\omega t-k_y y)}+\frac{\partial}{\partial z}A_z\mathrm{e}^{\mathrm{j}(\omega t-k_z z)}=0$. Applying the derivation leads to $-\mathrm{j}\,k_x E_x-\mathrm{j}\,k_y E_y-\mathrm{j}\,k_z E_z=0$, which is equivalent to $-\mathrm{j}\,\vec{k}\cdot\vec{E}=0$. Hence, the electric field $\vec{E}$ of a plane wave is transverse to the direction of propagation $\vec{k}$. This holds analogously for the magnetic field.

$$\vec{E}(\vec{r},t) = \underline{\vec{E}}(\vec{r},\omega)\mathrm{e}^{\mathrm{j}\omega t} = A\mathrm{e}^{\mathrm{j}(\omega t - kz)}\vec{J} = A\mathrm{e}^{\mathrm{j}(\omega t - kz)}\begin{pmatrix} J_x \\ J_y \end{pmatrix}. \qquad (2.74)$$

Polarization describes the relationship of the *x* and *y*-component of the complex wave vector: Linearly polarized light is defined by equal phases in the two orthogonal components, which have a phase difference of $2\varphi = 0$. Circular polarization is observed, if the phases are different by $\pi/2$ ($\varphi = \pm\pi/4$) and the amplitudes are same. If the relative vertical amplitude J_y is zero and the relative horizontal amplitude J_x is non-zero, the wave is horizontally polarized – vertical polarization is defined analogously with $J_x = 0$, $J_y \neq 0$. Any intermediate form with non-equal amplitudes and phases is called elliptical polarization.

Stokes vectors, in contrast to Jones vectors, contain four real elements, representing the total intensity I_{tot} and the intensities measured with a horizontal polarizer I_{hor}, a vertical polarizer I_{ver}, as well as intensities measured with a +45°- and a +135°-linear polarizer I_{45}, I_{135}, and the intensity measured with a right-circularly and a left-circularly polarizing filter I_{RZ}, I_{LZ}. According to these measurements the Stokes vector $\vec{S}_{\mathrm{t}}$ results in

$$\vec{S}_{\mathrm{t}} = \begin{pmatrix} s_1 \\ s_2 \\ s_3 \\ s_4 \end{pmatrix} = \begin{pmatrix} I_{\mathrm{tot}} \\ I_{\mathrm{hor}} - I_{\mathrm{ver}} \\ I_{45} - I_{135} \\ I_{\mathrm{RZ}} - I_{\mathrm{LZ}} \end{pmatrix}. \qquad (2.75)$$

Both the Stokes and the Jones formalisms allow to describe changes in the state of polarization by using matrices that transform the input polarization vector to the output vector. In case of multiple optical elements passed, the matrices have to be concatenated by matrix multiplication. In the Stokes calculus, the transformation matrices are named Mueller matrices, in the Jones calculus, Jones matrices. Accordingly, light of polarization $\vec{J_1}$ passing optical elements with Jones matrices $\mathbf{J}_{1\ldots\mathrm{n}}$ is transformed to light with Jones vector

$$\vec{J}_2 = \mathbf{J}_{\mathrm{n}} \cdots \mathbf{J}_1 \vec{J}_1. \qquad (2.76)$$

Expressed in Stokes vectors, light of polarization $\vec{S}_1$ passes elements with Mueller matrices $\mathbf{M}_{1...n}$ and is transformed to

$$\vec{S}_2 = \mathbf{M}_n \cdots \mathbf{M}_1 \vec{S}_1 . \tag{2.77}$$

Both calculi are linked and Mueller matrices can be derived from Jones matrices [52]. The reverse calculation of Jones matrices from Mueller matrices only succeeds in the case without depolarization.

The purpose of polarization considerations within this work is the description of polarization effects in optical media including the system itself and the sample under test. As OCT measurements record only the coherent part of the backscattered light, depolarized light will not be detected. Hence, the Jones calculus is sufficient for the description of PS-OCT and it allows direct access to the horizontal and vertical field components.

2.2.2 PS-OCT concepts

The very general aim of a PS-OCT measurement is the depth-dependent determination of polarization properties of a sample [53]. Depending on the application, it suffices to only determine birefringence [54], dichroism, the optical axis orientation [55] or a set of Stokes parameters [56] for a single incident polarization. This leads to simplifications in the optical setup and reduced measurement time, as compared to more comprehensive PS-OCT systems with capability of extracting the full Jones [57] or Mueller [58] matrix of the material. Early systems were based on conventional TD-OCT approaches [53], whereas later polarization-sensitive systems also adopt the SD-OCT or SS-OCT concept [59].

2.2.3 Applications of PS-OCT

PS-OCT systems can serve for various applications. In dental OCT, buried caries lesions can be detected by PS-OCT, as demineralization accompanying carious defects leads to anisotropically ordered structures, which cause cross-polarized backscatter signals [60]. Dermatologic applications comprise analysis of burn depths that can be determined by characterization of the

birefringence difference between unaffected skin layers and layers with former heat impact [61]. This is possible, since collagen proteins in the skin are originally birefringent, but denaturate from temperatures of around 60°C onwards, while losing their polarization properties. PS-OCT is further applied to the detection of basal cell carcinoma, which lead to a local alteration of skin structure and thus to local changes in dermal birefringence [62]. Recent studies combined this analysis with a machine-learning algorithm and achieved a detection sensitivity and specificity of 93 % and 87 %, respectively [63]. An important application field of PS-OCT is ophthalmology, aiming at, e.g., early-stage detection of glaucoma. This degeneration of the retinal nerve fibre layer is in some cases preceded by a necrosis of ganglion cells inducing a replacement of nerve axons by tissue of a lower degree of organization. Hence, the birefringence of the retinal nerve fibre layer changes. A PS-OCT measurement can detect this birefringence modification and thus allows for early diagnosis of glaucoma [64]. As a use case in material sciences, PS-OCT is applied to determine mechanical stress in glass/epoxy composites, where the birefringence of the material is stress dependent in both orientation and magnitude [65]. The PS-OCT analysis offers the prospect of early failure detection.

2.2.4 Measurement principle

A free-space optical setup of a PS-OCT system is depicted in Figure 2.12. With a single measurement of both received polarizations, this setup is capable of determining the birefringent properties of the sample [53].

In contrast to the conventional free-space TD-OCT, see Figure 1.2, the incident light is horizontally polarized by a polarizer (Pol) before being split among sample and reference arm. The part towards the sample passes a quarter-wave plate (QWP) at 45°, which leads to circularly polarized light incident on the sample. This can be seen from the following analysis:

A QWP with its fast axis in the horizontal direction is described by the Jones matrix [66]

$$\mathbf{J}_{\mathrm{QWP}} = \mathrm{e}^{\mathrm{j}\frac{\pi}{4}} \begin{pmatrix} 1 & 0 \\ 0 & \mathrm{j} \end{pmatrix}. \tag{2.78}$$

Using the rotation matrix [67]

$$\mathbf{R}(\vartheta) = \begin{pmatrix} \cos\vartheta & \sin\vartheta \\ -\sin\vartheta & \cos\vartheta \end{pmatrix}, \tag{2.79}$$

the optical element, here the rotated QWP with fast axis at an angle ϑ to the horizontal direction, can be expressed by the Jones matrix

$$\begin{aligned} \mathbf{J}_{\mathrm{QWP}}(\vartheta) &= \mathbf{R}(-\vartheta)\,\mathbf{J}_{\mathrm{QWP}}\,\mathbf{R}(\vartheta) \\ &= \mathrm{e}^{\mathrm{j}\frac{\pi}{4}} \begin{pmatrix} \cos^2\vartheta + \mathrm{j}\sin^2\vartheta & (1-\mathrm{j})\sin\vartheta\cos\vartheta \\ (1-\mathrm{j})\sin\vartheta\cos\vartheta & \sin^2\vartheta + \mathrm{j}\cos^2\vartheta \end{pmatrix}. \end{aligned} \tag{2.80}$$

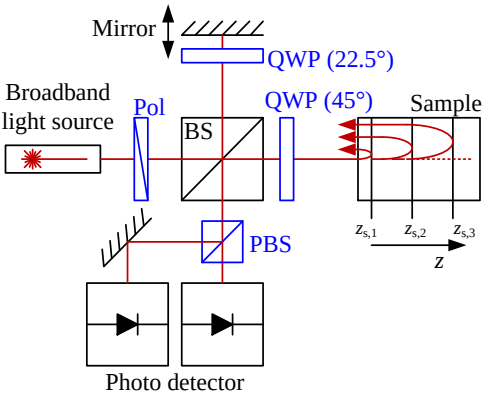

Figure 2.12: Free-space polarization-sensitive OCT setup. Pol: Polarizer, BS: (non-polarizing) beam splitter, QWP: quarter-wave plate at given orientations of the fast axis with respect to the horizontal direction, PBS: polarization beam splitter. The setup is a modification of the conventional TD-OCT setup shown in Figure 1.2. The sample comprises various reflections at depths $z_{s,1}$, $z_{s,2}$ and $z_{s,3}$. The polarizer lets horizontally polarized light pass, and the sample is illuminated by circular polarization. The light passing the 22.5°-QWP in the reference arm forth and back returns to the BS linearly polarized at −45°. The interference signal is split at the PBS in horizontal and vertical polarization and is detected.

With $\vartheta = 45°$ this results in

$$\mathbf{J}_{\mathrm{QWP}}(45°) = \frac{1}{2}\mathrm{e}^{\mathrm{j}\frac{\pi}{4}}\begin{pmatrix} 1+\mathrm{j} & 1-\mathrm{j} \\ 1-\mathrm{j} & 1+\mathrm{j} \end{pmatrix}. \tag{2.81}$$

Applied to horizontally polarized input light, as is the case here, the output polarization travelling towards the sample is

$$\vec{J}_{\mathrm{s}} = \frac{1}{2}\mathrm{e}^{\mathrm{j}\frac{\pi}{4}}\begin{pmatrix} 1+\mathrm{j} & 1-\mathrm{j} \\ 1-\mathrm{j} & 1+\mathrm{j} \end{pmatrix}\begin{pmatrix} 1 \\ 0 \end{pmatrix} = \frac{1}{2}\mathrm{e}^{\mathrm{j}\frac{\pi}{4}}\begin{pmatrix} 1+\mathrm{j} \\ 1-\mathrm{j} \end{pmatrix} = \frac{\sqrt{2}}{2}\begin{pmatrix} \mathrm{j} \\ 1 \end{pmatrix}, \tag{2.82}$$

which represents a circular polarization state, characterized by equal amplitudes in each of the orthogonal axes and 90° optical phase delay. Circular polarization is of advantage over linear polarization, as an arbitrary linear polarization could coincide with the optical axis of the sample. In this unwanted case, no birefringence information could be extracted, as the difference in propagation constants of slow and fast axes would not be measurable.

The light returning from the reference arm has passed a QWP at 22.5° in forward and backward direction, which results in −45° linearly polarized light, as is explained in the following calculation:

The reference arm represents a concatenation of QWP, plane mirror and QWP in reverse direction of propagation, leading to the total Jones matrix of the reference arm

$$\mathbf{J}_{\mathrm{ref}}(\vartheta) = \mathbf{J}_{\mathrm{QWP,rev}}(\vartheta)\mathbf{J}_{\mathrm{M}}\mathbf{J}_{\mathrm{QWP}}(\vartheta)\ . \tag{2.83}$$

The Jones matrix $\mathbf{J}_{\mathrm{QWP}}(\vartheta)$ of a rotated QWP has been evaluated in Eq. (2.80) and is unitary, as a QWP represents a loss- and gainless element [68] leading to an expression of the type

$$\mathbf{J}_{\mathrm{QWP}}(\vartheta) = \begin{pmatrix} u_1 & u_2 \\ -u_2^* & u_1^* \end{pmatrix} \tag{2.84}$$

with the matrix elements

$$u_1 = \mathrm{e}^{\mathrm{j}\frac{\pi}{4}}\left(\cos^2\vartheta + \mathrm{j}\sin^2\vartheta\right),$$
$$u_2 = \mathrm{e}^{\mathrm{j}\frac{\pi}{4}}\left((1-\mathrm{j})\sin\vartheta\cos\vartheta\right). \tag{2.85}$$

We choose a right-handed Cartesian coordinate system, with the +z-direction being always parallel to the direction of propagation of light. Hence, when light is incident on a plane mirror, the reflected light is described by a coordinate system rotated about the *x*-axis, and the Jones matrix of a plane mirror at perpendicular incidence becomes [68]

$$\mathbf{J}_{\mathrm{M}} = \begin{pmatrix} 1 & 0 \\ 0 & -1 \end{pmatrix}. \tag{2.86}$$

The Jones matrix $\mathbf{J}_{\mathrm{rev}}$ of reverse propagation of any optical reciprocal material with Jones matrix $\mathbf{J}$, when taking into account a coordinate system as described above, can be written as [69]

$$\mathbf{J}_{\mathrm{rev}} = \begin{pmatrix} m_1 & -m_3 \\ -m_2 & m_4 \end{pmatrix}, \quad \text{with } \mathbf{J} = \begin{pmatrix} m_1 & m_2 \\ m_3 & m_4 \end{pmatrix}. \tag{2.87}$$

In case of a unitary reciprocal material like the QWP, compare Eq. (2.84), this leads to

$$\mathbf{J}_{\mathrm{QWP,rev}} = \begin{pmatrix} u_1 & u_2^* \\ -u_2 & u_1^* \end{pmatrix}. \tag{2.88}$$

Now, the total Jones matrix of the reference path can be calculated from Eq. (2.83),

$$\begin{aligned} \mathbf{J}_{\mathrm{ref}}(\vartheta) &= \mathbf{J}_{\mathrm{QWP,rev}}(\vartheta)\,\mathbf{J}_{\mathrm{M}}\,\mathbf{J}_{\mathrm{QWP}}(\vartheta) \\ &= \begin{pmatrix} u_1^2 + u_2^{*2} & u_1u_2 - (u_1u_2)^* \\ -u_1u_2 + (u_1u_2)^* & -u_1^{*2} - u_2^2 \end{pmatrix} \\ &= \mathrm{j}\begin{pmatrix} \cos(2\vartheta) & \sin(2\vartheta) \\ -\sin(2\vartheta) & \cos(2\vartheta) \end{pmatrix}. \end{aligned} \tag{2.89}$$

This combination of forward-pass of the QWP, the mirror and the reverse pass of the QWP acts similarly to a half-wave plate (HWP) with

$$\mathbf{J}_{\mathrm{HWP}}(\vartheta) = \mathrm{j}\begin{pmatrix} \cos(2\vartheta) & \sin(2\vartheta) \\ \sin(2\vartheta) & -\cos(2\vartheta) \end{pmatrix}, \tag{2.90}$$

where the second row of the Jones matrix is negated as compared to $\mathbf{J}_{\mathrm{ref}}(\vartheta)$. With the fast axis of the QWP at $\vartheta = 22.5°$ with respect to the horizontal axis, the overall reference path matrix is

$$\mathbf{J}_{\mathrm{ref}}(22.5°) = \mathrm{j}\frac{\sqrt{2}}{2}\begin{pmatrix} 1 & 1 \\ -1 & 1 \end{pmatrix}. \tag{2.91}$$

Applied to horizontally polarized input light, this results in

$$\bar{J}_{\mathrm{r}} = \mathrm{j}\frac{\sqrt{2}}{2}\begin{pmatrix} 1 & 1 \\ -1 & 1 \end{pmatrix}\begin{pmatrix} 1 \\ 0 \end{pmatrix} = \mathrm{j}\frac{\sqrt{2}}{2}\begin{pmatrix} 1 \\ -1 \end{pmatrix} \tag{2.92}$$

referring to as linear polarization at −45°. Hence, with equal amplitudes in horizontal and vertical direction, the reference field could interfere with both horizontally and vertically polarized components of the field backscattered from the sample. The polarizing beam splitter in the detection path splits both polarizations and guides them to separate detectors. Birefringence of the sample would emerge as oscillation of signal strength between the two detection polarizations versus measured sample depth. With rotation of the sample or of the optic elements in the system, the optic axis of the sample could be determined.

In free-space optical systems, the polarization can be controlled exactly at any point of the system but is sensitive with respect to mechanical misalignment. In contrast to that, fibre-based systems are more robust, but propagation of light in single-mode fibres (SMF) influences the optical phase in both orthogonal polarizations in an undetermined way and thus modifies the polarization state. In case of commonly used standard SMF, this impact is highly dependent on the exact positioning of the fibres, fibre bend stress and temperature. Thus, without calibration, the Jones matrix of a fibre is unknown. The use of polarization-maintaining fibres could circumvent this calibration step, as the

incident polarization state can be maintained. This polarization-maintaining behaviour is possible by minimizing cross-talk between signals in the slow and the fast axis of the fibre, which is achieved by stress-induced differences in the individual propagation constants.

In OCT practice, polarization-maintaining fibres are difficult to deploy, since the strong group delay differences between the slow and the fast axis leads to ghost images at a relative amplitude, which corresponds to the polarization cross talk, which may, e.g., occur at each fibre-to-fibre connection. From the moment of polarization mode coupling, each portion of the respective polarization travels with a distinct speed and arrives at the detector with a respective time delay. This is equivalent to different imaging depths in the sample. With these ghost images, OCT signal analysis would become severely disturbed. For high-end PM connectors, cross-talk can be kept smaller than -30 dB. Still, with dynamic ranges of more than 60 dB, this is insufficient for many OCT applications. As a consequence, the use of polarization-maintaining fibres is avoided and we use standard single-mode fibres instead. A polarization calibration process is then mandatory.

A fibre-based system faces two challenges: First providing a method for characterization and compensation of the SMF-induced polarization change, and second, supplying the sample with incident light, with polarization different to the principal state of the sample medium. The latter property is important in order to measure material birefringence by observing a difference in propagation constants of the material. For a more comprehensive analysis of the material, e.g., when Mueller or Jones matrices are to be measured, the system needs to be able to vary the state of polarization incident on the sample.

In the following we present a system concept, which satisfies the abovementioned conditions for a fibre-based Jones matrix PS-OCT, see Figure 2.13. Light emitted by the frequency-swept light source (SS) is sent through a first polarizer, thus guaranteeing a constant input polarization during one measurement. This light propagates either towards the sample measurement head or to the calibration setup and leaves the fibre section in the sample path (SP) with polarization $\bar{J}_{\mathrm{in}}$. The portion of the input light travelling through the ref-

erence path (RP) is adjusted in polarization, such that it later splits in equal parts on the two axes of the PBS in the detection path. This is controlled by monitoring the received power at each of the single photodiodes. This setting ensures that a received sample field can interfere with the reference field, independent of its polarization. When a sample is characterized, the sample is illuminated with a set of different polarizations, arising from different rotational positions ϑ_Q of the fast axis of the QWP (QWP 2) with respect to the horizontal axis (0° to 165° with a step size of 15) with corresponding Jones matrices $\mathbf{J}_\mathrm{QWP2}\left(\vartheta_\mathrm{Q}\right)$. In the sample, the light undergoes a depth-dependent polarization change $\mathbf{J}_\mathrm{s}\left(z\right)$. This Jones matrix incorporates forward propagation to the backscattering plane at depth *z*, the scattering process itself, and backpropagation. Dependent on the material to be investigated, either material propagation, e.g., in birefringent material like skin, or the scattering processes, e.g., at elongated nanoparticles, dominate the Jones matrix. Backscattered light exiting the sample towards the fibre-optic system reversely passes the QWP 2. The reverse propagation leads to the Jones matrix $\mathbf{J}_\mathrm{QWP2,rev}\left(\vartheta_\mathrm{Q}\right)$, see Eqs. (2.88) and (2.85). The following fibre-optic propagation back through the SP and then towards the PBS in the receiver arm is taken into account by the matrix $\mathbf{J}_\mathrm{sys}$. Finally, the Jones vector as incident on the PBS, and thus measured by the detector is

$$\vec{J}_\mathrm{m} = \mathbf{J}_\mathrm{sys}\mathbf{J}_\mathrm{QWP2,rev}\left(\vartheta_\mathrm{Q}\right)\mathbf{J}_\mathrm{s}\mathbf{J}_\mathrm{QWP2}\left(\vartheta_\mathrm{Q}\right)\vec{J}_\mathrm{in}\,. \tag{2.93}$$

The matrices $\mathbf{J}_\mathrm{QWP2}\left(\vartheta_\mathrm{Q}\right)$ and $\mathbf{J}_\mathrm{QWP2,rev}\left(\vartheta_\mathrm{Q}\right)$ are defined by the rotation angle ϑ_Q of the QWP 2. The matrix of interest $\mathbf{J}_\mathrm{s}$ is unknown, as well as the system matrix $\mathbf{J}_\mathrm{sys}$ and the Jones vector $\vec{J}_\mathrm{in}$ of the input light. Assuming $\mathbf{J}_\mathrm{sys}$ and $\vec{J}_\mathrm{in}$ would be known, $\mathbf{J}_\mathrm{s}$ could be determined from a set of measurements of $\vec{J}_\mathrm{m}$ with different QWP-settings. However, both $\mathbf{J}_\mathrm{sys}$ and $\vec{J}_\mathrm{in}$ depend on the unknown polarization transformation in the fibre optic system, which makes a preceding calibration step necessary. Once both are determined, the calibration holds until fibres are moved or the temperature changes.

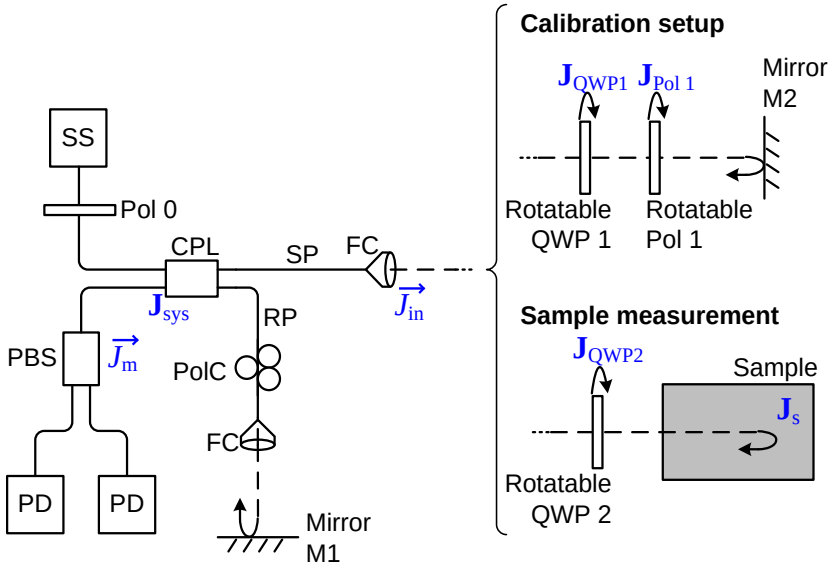

Figure 2.13: Fibre-based swept-source polarization-sensitive OCT setup. SS: Swept source, Pol 0,1: Polarizer, CPL: 3-dB fibre coupler (polarization-insensitive), SP: sample path, RP: reference path, FC: fibre collimator, QWP 1,2: quarter-wave plates with Jones matrix $\mathbf{J}_{\mathrm{QWP1,2}}\left(\vartheta_{\mathrm{Q}}\right)$, PBS: polarization beam splitter, PD: photodetector, PolC Polarization controller. Jones vectors and matrices are denoted in blue colour. $\vec{J}_{\mathrm{in}}$: Jones vector of the light exiting the fibre section towards the sample, $\mathbf{J}_{\mathrm{Pol1}}\left(\vartheta_{\mathrm{P}}\right)$: Jones matrix of the polarizer in the calibration setup, $\mathbf{J}_{\mathrm{s}}$: Jones matrix of the sample, $\mathbf{J}_{\mathrm{sys}}$: Jones matrix of the fibre optic system connecting the FC in the sample path to the PBS, $\vec{J}_{\mathrm{m}}$: measured Jones vector at the PBS. For polarization calibration a calibration setup consisting of a rotatable QWP (QWP 2), a polarizer , and a mirror (M2) is used in the sample arm.

In order to perform this calibration, the sample is replaced by a calibration setup, comprising a rotatable polarizer and a plane mirror, see Figure 2.13. By rotation of the polarizer POL 1 to the angular positions $\vartheta_{\mathrm{P}} = 0°$ to 150° in steps of 30°, and by rotation of the QWP 1 to the angular positions $\vartheta_{\mathrm{Q}} = 0°$ to 165° in steps of 15°, several polarization states can be generated and the fibre-optic system can be probed with these. During this calibration, the Jones vector received by the PBS is given by

$$\vec{J}_{\mathrm{m,cal}} = \mathbf{J}_{\mathrm{sys}}\mathbf{J}_{\mathrm{QWP1,rev}}\left(\vartheta_{\mathrm{Q}}\right)\mathbf{J}_{\mathrm{Pol1,rev}}\left(\vartheta_{\mathrm{P}}\right)\mathbf{J}_{\mathrm{M}}\mathbf{J}_{\mathrm{Pol1}}\left(\vartheta_{\mathrm{P}}\right)\mathbf{J}_{\mathrm{QWP1}}\left(\vartheta_{\mathrm{Q}}\right)\vec{J}_{\mathrm{in}}, \quad (2.94)$$

with the Jones matrices $\mathbf{J}_{\mathrm{Pol1}}\left(\vartheta_{\mathrm{P}}\right)$ of the polarizer, $\mathbf{J}_{\mathrm{Pol1,rev}}\left(\vartheta_{\mathrm{P}}\right)$ of the polarizer in reverse direction of propagation, and the Jones matrix $\mathbf{J}_{\mathrm{M}}$ of the plane mirror. The mirror can be replaced by any strongly reflecting surface, e.g. by the surface of a glass cuvette containing the sample. The determination of $\mathbf{J}_{\mathrm{sys}}$ and $\vec{J}_{\mathrm{in}}$ results from a least-squares fit of the system model in Eq. (2.94) for several angular settings of the QWP 1 and of the polarizer.

3 Multi-scale dispersion-state characterization of nanocomposites using OCT

The following chapter corresponds to publication [P2] with slight adaptations to match the format and the structure of this thesis.

[Begin of Publication P2]

Multi-scale dispersion-state characterization of nanocomposites using optical coherence tomography

Scientific Reports; Volume 6; 31733; August 2016
DOI: 10.1038/srep31733

S. Schneider[1], F. Eppler[1,*], M. Weber[1], G. Olowojoba[2,†], P. Weiss[2], C. Hübner[2], I. Mikonsaari[2], W. Freude[1,3] and C. Koos[1,3]

[1] Karlsruhe Institute of Technology (KIT), Institute of Photonics and Quantum Electronics (IPQ), 76131 Karlsruhe, Germany.
[2] Fraunhofer Institute for Chemical Technology (ICT), 76327 Pfinztal, Germany.
[3] Karlsruhe Institute of Technology (KIT), Institute of Microstructure Technology (IMT), 76131 Karlsruhe, Germany.
[*] Present address: Karlsruhe Institute of Technology (KIT), Institute of Product Engineering (IPEK), 76131 Karlsruhe, Germany.
[†] Present address: Imperial College London, Department of Mechanical Engineering, London SW7 2AZ, UK.

Nanocomposite materials represent a success story of nanotechnology. However, development of nanomaterial fabrication still suffers from the lack of adequate analysis tools. In particular, achieving and maintaining well-dispersed particle distributions is a key challenge, both in material development and industrial production. Conventional methods like optical or electron microscopy need laborious, costly sample preparation and do not permit fast extraction of nanoscale structural information from statistically relevant sample volumes. Here we show that optical coherence tomography (OCT) represents a versatile tool for nanomaterial characterization, both in a laboratory and in a production environment. The technique does not require sample preparation and is applicable to a wide range of solid and liquid material systems. Large particle agglomerates can be directly found by OCT imaging, whereas dispersed nanoparticles are detected by model-based analysis of depth-dependent backscattering. Using a model system of polystyrene nanoparticles, we demonstrate nanoparticle sizing with high accuracy. We further prove the viability of the approach by characterizing highly relevant material systems based on nanoclays or carbon nanotubes. The technique is perfectly suited for in-line metrology in a production environment, which is demonstrated using a state-of-the-art compounding extruder. These experiments represent the first demonstration of multi-scale nanomaterial characterization using OCT.

3.1 Introduction

Nanomaterials represent an emerging multi-billion dollar market driven by a vast variety of applications that range from mechanical and civil engineering to energy storage and life sciences. Examples comprise nanocomposite polymers with enhanced mechanical or electronic properties [11,12], functional coatings [70], flame-retardant materials [71], advanced drug-delivery systems [13], and anode materials for Li-ion batteries [72]. These applications mostly rely on the unique properties of nanosize particles, namely huge surface-to-volume ratios, enhanced tensile strengths and superior electrical conductivities as shown by carbon nanotubes (CNT) or other nanofibers [73], or outstanding barrier properties of nanoplatelets [74]. Properties of

nanocomposites depend not only on the size and shape of the particles but also on their dispersion state, characterized by the degree of agglomeration when immersed into a liquid or solid host material. The dispersion state is governed by the nanoparticle properties, by the composition and the physical parameters of the host material, as well as by the processing route adopted for dispersing the nanoparticles in the host material. In order to ensure consistent product quality, the dispersion state must be continuously monitored during fabrication, which has been identified a key challenge both in nanomaterial development and industrial production [18]. In solid media, dispersion-state characterization mainly relies on microscopic imaging. For small nanoparticles, this requires high-resolution techniques such as scanning-electron microscopy (SEM) of specially prepared sample surfaces [19], or transmission electron microscopy (TEM) of microtome slices [20]. In both cases, sample preparation is laborious and costly and not well suited for quality control or process development, where sample processing and analysis have to be continuously iterated. Moreover, SEM and TEM are limited to small sample volumes, which are not necessarily representative of the entire batch. Light microscopy, on the other hand, can reduce the experimental effort [21], but is limited to the identification of large agglomerates in sufficiently transparent samples and areas close to the surface. In contrast to image-based methods, light scattering techniques have proven to be viable tools for measuring particle size distributions from large sample volumes. Static light scattering (SLS) relies on angle-resolved and/or spectrally resolved detection of scattered light [22,23] and is based on a rather complex optical setup, especially when large scattering angles have to be taken into account. Moreover, for solid samples, it is challenging to separate scattering inside the sample volume from contributions of the rough sample surface. Dynamic light scattering (DLS) methods exploit temporal fluctuations of interference patterns of scattered light to calculate the Brownian motion and the hydrodynamic diameter of particles within the respective solvent [75]. This technique is limited to low concentrations, and can only be applied to liquid media. In addition, both SLS and DLS suffer from limitations in dealing with mixtures of particles having vastly different diameters that may range, e.g., from a few nanometres to hundreds of micrometres,

as is often the case for nanocomposites with poorly dispersed nanoparticles. Partial wave spectroscopic microscopy (PWS) [76] has been used for investigation of nanoscale refractive index fluctuations, which can be an early indicator of carcinogenesis, yet without providing a link to the size of the scatterers. X-ray diffraction (XRD) [77] or small-angle X-ray scattering (SAXS) [78] finally rely on diffraction or scattering of X-rays in the sample and are able to reveal the atomic or molecular arrangement inside the material. However, high instrumental effort and a small probing region limit the application range of these methods to the laboratory environment. Hence, none of the aforementioned techniques can meet the stringent requirements associated with industrial process development and quality control, which comprise robustness of the measurement method, fast analysis, the capability to characterize representative sample volumes without laborious sample preparation, good mechanical and thermal robustness of the measurement system, and the possibility to integrate the measurement system into the processing line for enabling in-line process control. The lack of adequate analysis methods for dispersion-state characterization is considered one of the major obstacles towards large-scale industrial processing and exploitation of nanomaterials.

As an alternative, optical coherence tomography (OCT) [1,28,79] was proposed as a tool for nanocomposite characterization [80,81]. OCT provides three-dimensional imaging data from the bulk of the sample and avoids expensive sample preparation. However, previous demonstrations have been limited to image-based analysis of composites containing rather large microparticles combined with wavelet-based processing of the image data [81]. Due to the limited resolution of OCT imaging, this method cannot provide information about the nanoscopic structure of the nanocomposite such as the particle size. A further method uses a spectral-domain OCT setup and measures the size of particles suspended in a fluid by the temporal variation of the optical phase due to particle diffusion [82,83]. Particle sizes range from 15 nm to 625 nm. The main disadvantage is that only particles suspended in a fluid can be investigated, and that parameters like viscosity and temperature need to be tightly controlled. Another technique is angle-resolved OCT [84], where the angular dependence of the scattered intensity is evaluated according to Mie's theory.

However, the angular range is limited to about 0.5 rad due to practical reasons, and the particle size which can be detected is not smaller than 5 µm in diameter. A further approach is low-coherence spectroscopy, which allows the extraction of wavelength-dependent scattering coefficients of the investigated samples and compares well with Mie scattering calculations [85]. The aforementioned techniques serve well for the determination of scattering parameters from nanoparticle samples, but miss the multi-scale approach, including imaging of large agglomerates. A technique using a setup similar to spectral-domain OCT is super-resolution imaging relying on spectral encoding of spatial frequency (SESF) [86]. With that approach, sub-micrometre imaging has been demonstrated, but exact nanoparticle sizes cannot be extracted due to the still limited resolution. In summary, OCT-based quantitative and qualitative characterization of composites at the nanoscale still remains to be shown.

In this paper we demonstrate that OCT represents an attractive tool for fast and robust dispersion-state characterization of composite materials over a wide range of particle and agglomerate sizes both on the micrometre and on the nanometre scale. The technique pursues a multi-scale approach: Using a theoretical model of light scattering in the sample, we accurately measure particle sizes down to 140 nm. Particle agglomerates with sizes of up to hundreds of micrometres can be easily detected by applying dedicated image processing techniques to the OCT data. Both methods can be performed *in situ*, without prior sample preparation, in both liquid and solid materials, and are applicable to laboratory investigations as well as to in-line process control in industrial production. Using a model system of polystyrene nanoparticles dispersed in water, we prove the reliability and accuracy of our sizing technique. We further apply the technique to an epoxy resin filled with multi-wall carbon nanotubes (MWCNT). The results of OCT-based scattering analysis show good correlation with independently measured material properties, thereby outperforming conventional characterization techniques based on light microscopy. Finally, we show that our technique is also perfectly suited for in-line metrology in a production environment. To this end, we integrate our system with a state-of-the-art industrial compounding extruder using a dedicated optical probe. The OCT system operates reliably during the compounding process and

allows to immediately examine the impact of extruding parameters on the dispersion state of the material. We believe that OCT will pave the path towards industrially viable nanomaterial characterization and process control.

3.2 Materials and Methods

3.2.1 Swept-source optical coherence tomography system

Optical coherence tomography (OCT) evolved greatly in the past decades. The technique provides microscopic resolution in volumetric imaging and highly sensitive detection of backscattered optical power. OCT opened a wide field of applications reaching from ophthalmology in medical diagnostics [87] to particle and defect characterization in material sciences [80,88]. Among various implementations, swept-source OCT (SS-OCT) offers a particularly attractive combination of highest sensitivity and high imaging speed [28].

The SS-OCT setup used in this work is depicted in Figure 3.1 (a). In general, an OCT system measures the position and the strength of a multitude of scatterers along a light path in a sample. To this end, the electric field that is backreflected from a sample is compared in amplitude and phase to a reference field. Both the sample and the reference field are derived from the same optical swept-wavelength source (SS). In our experiments, we use an SS laser with central wavelength of 1315 nm and a wavelength scanning range of 1260−1370 nm, a scan rate of 1 kHz, and 10 dBm average output power (model s3, Micron Optics Inc., Atlanta, GA, USA). The scan range of the laser corresponds to a theoretical depth resolution of 7 µm, which compares well to the experimentally observed resolution of 11 µm. A first fibre-based directional coupler (CPL1, splitting ratio 50:50) is used to split the power among the sample path (SP) and the reference path (RP). The reference path contains a free-space section allowing precise matching of the RP and SP length. Backscattered light from the sample and light travelling along the RP is superimposed in a second fibre-based coupler (CPL2, splitting ratio 50:50) and coupled to a balanced photodetector (BD, model PDB430C, Thorlabs, Munich, Germany). The output current of the BD contains patterns resulting from

interference of the backscattered field with the reference field. The BD suppresses intensity noise from the strong RP signal and enables a large dynamic range and a high sensitivity, defined by the lowest detectable backscatter from the sample, of −110 dB. The electrical signal is digitized by a 16 bit analogue-to-digital converter (ADC, model ATS660, Alazar Technologies Inc., Pointe-Claire, Canada) and processed in a personal computer (PC). The amplitude and the position of the backscatter along the light path can be obtained by Fourier analysis of the photocurrent as a function of optical frequency [28]. One depth-scan (A-scan) consists of 768 measurement points with 8 µm step size. We extract the backscatter strength, which denotes the ratio of backscattered optical power to optical power incident on the sample.

In the course of this work, the SP of the SS-OCT system is connected to two different scan heads: First, to a conventional OCT scan head for off-line characterization of laboratory samples, Figure 3.1 (b), and second, to a specially developed probe head for in-line dispersion characterization during the compounding process in an industrial extruder, Figure 3.1 (c). This probe is designed for the harsh environmental conditions at a nanocomposite production line and must tolerate vibrations, high temperatures of 250°C, and high pressures of 200 bar. The probe features a titanium shaft and a sapphire window towards the sample, and is designed to allow the adjustment of focal length and the axial position of the focus within the sample.

3.2.2 Model-based dispersion-state analysis and sizing of nanoparticles

Big agglomerates of nanoparticles with dimensions larger than the resolution limit of the OCT system can be detected directly by imaging. However, size information on nanoscale agglomerates and single particles is relevant as well. In this section we show that model-based analysis of OCT backscatter measurements allows to extract scattering parameters that are correlated with the dispersion state of the material so that even small particle sizes can be determined.

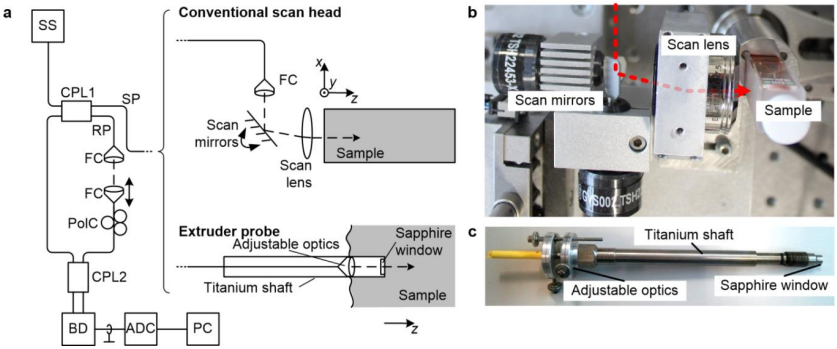

Figure 3.1: Fibre-based swept-source optical coherence tomography (SS-OCT) setup for laboratory measurements and in-line process control. **(a)** Schematic setup of the SS-OCT. SS: Swept-wavelength source, scanning range 1260-1370 nm; CPL1,2: fibre-based directional coupler; SP: sample path; RP: reference path; FC: fibre collimator; PolC: polarization controller; BD: balanced photodetector; ADC: analogue-to-digital converter; PC: personal computer. **(b)** Laboratory scan head with galvo-based scanners and a scan lens for 3D-imaging. The red line indicates the light beam towards the sample. **(c)** Extruder probe for in-line measurements. The probe consists of a titanium shaft for a high temperature environment and comprises a sapphire window towards the sample.

The analysis relies on a single-scattering model assuming that incident light is scattered at maximum once within the medium, similar to the approach used by Kodach *et al.* [89]. This model is found to be appropriate for weakly scattering samples and for an analysis of moderate scattering depths [90]. As depicted in Figure 3.2 (a), a light beam with input power P_{in} enters the sample. At each particle (grey), a first portion (blue) of the incident light in the respective depth z is scattered back into the numerical aperture of the optical system, a second portion (red) is scattered into all other directions or is absorbed, and the remaining third portion (black) is propagating deeper into the medium. The total scattering σ_{s} and absorption cross section σ_{a} can be described by the extinction cross section $\sigma_{\mathrm{t}} = \sigma_{\mathrm{s}} + \sigma_{\mathrm{a}}$ of a single particle, or by the extinction coefficient $\mu_{\mathrm{t}} = N\sigma_{\mathrm{t}}$ for an ensemble of particles with volume number density N. In analogy, the backscatter is described by the backscatter cross section σ_{b}, or by the backscatter coefficient $\mu_{\mathrm{b}} = N\sigma_{\mathrm{b}}$ of the material.

The depth-dependent decay $\mathrm{d}P(z)/\mathrm{d}z = -\mu_t P(z)$ of the forward-travelling power $P(z)$ is dictated by the extinction coefficient μ_t, leading to an exponential decay of optical power $P(z) = P_{in}\mathrm{e}^{-\mu_t z}$ inside the sample. For a given depth *z*, the power in a depth element δz as scattered back into the numerical aperture of the optical system amounts to $P_b(z) = \mu_b \delta z P(z)\mathrm{e}^{-\mu_t z}$, where $\mathrm{e}^{-\mu_t z}$ accounts for the extinction of the backscattered light during backpropagation. The signal measured in an OCT scan corresponds to the depth-dependent backscatter $P_b(z)/P_{in}$. In the presence of a depth-independent noise floor R_n, the depth-dependent backscatter signal measured by the OCT system is

$$R_s(z) = \mu_b \, \delta z \, \mathrm{e}^{-2\mu_t z} + R_n . \tag{3.1}$$

A semi-logarithmic plot $R_{dB}(z) = 10\lg\left(R_s(z)\right)$ of this backscatter signal is depicted in Figure 3.2 (b). The background noise term R_n defines the sensitivity limit of the OCT system. For real OCT systems, this background noise is sometimes dominated by relative intensity noise (RIN) of the swept source, which may lead to a depth-dependent noise floor. In contrast to that, the noise floor in our system originates from thermal noise of the receiver electronics, which exhibits a white power spectrum and is hence constant over the depth range of interest. Note that all measurements for particle sizing are taken under oblique incidence of the OCT beam on the sample surface. This avoids occurrence of isolated reflection peaks at the sample surface such that the signal model according to Eq. (3.1) can be directly used to fit the measurement data.

In real OCT measurements, the measured backscatter depends on further parameters, which need to be determined in a calibration step. This comprises the divergence of the measurement beam, the decay of the coherence function of the swept laser, and the absorption of the matrix material which surrounds the scatterers. These influences are approximated by including two calibration factors [80,91] *q* and *Q* in the single-scattering model according to Eq. (3.1),

$$R_s(z) = Q\mu_b \, \delta z \, \mathrm{e}^{-2z(\mu_t + q)} + R_n . \tag{3.2}$$

Both calibration factors are determined by comparing measured backscatter of a NIST-traceable polystyrene particle standard (246 nm diameter polystyrene nanospheres in 0.5 wt.% aqueous dispersion, BS-Partikel GmbH, Wiesbaden, Germany) with the model calculations according to Eq. (3.1).

In the special case of spherical scatterers with a size in the order of the wavelength, the scattering cross section σ_s can be modelled by means of Mie's theory [50]. As an example, Figure 3.2 (c) shows direction-dependent scattering lobes of water-dispersed polystyrene nanospheres with diameters 143 nm and 506 nm. The larger sphere (506 nm diameter) shows stronger total scattering (red), but less pronounced fractional backscatter as compared to the small sphere (143 nm diameter). For a small aperture of the scan head (1° half-angle, corresponding to a theoretical and experimental lateral resolution of 28 µm and 36 µm, respectively), the Mie scattering lobes can be parameterized using the total scattering cross section σ_s and the backscattering cross section σ_b. Figure 3.2 (d) shows both cross sections σ_s and σ_b as a function of the sphere diameter d for polystyrene (PS) spheres (refractive index $n_{PS} = 1.57$) dispersed in water (refractive index $n_{H_2O} = 1.33$) at a wavelength of 1315 nm. In the limit of small diameters d, Mie scattering can be approximated by Rayleigh scattering. In this regime, both scattering cross sections increase in proportion to d^6. For larger diameters, the spheres show resonances, which lead to dips in the backscattering cross section σ_b, whereas the total scattering cross section remains unaffected. The relationship between backscattering cross section σ_b and particle size is unambiguous only if the particle diameter is smaller than 460 nm, which corresponds to roughly half the material wavelength in the polystyrene spheres.

In real measurements, the total scattering cross section σ_s and the backscattering cross section σ_b cannot be assessed directly. Instead, only the extinction coefficient $\mu_t = N\sigma_t$ and the backscatter coefficient $\mu_b = N\sigma_b$ are extracted from the backscatter signal $R_s(z)$. For non-absorbing particles in the Rayleigh scattering regime, particle size and concentration cannot be separately evaluated, since both σ_s and σ_b increase with d^6, Figure 3.2 (d). As an example, for particle sizes of less than 150 nm ($\lambda / 9$), we can safely assume Rayleigh

scattering, and the backscattering probability $p_b = \sigma_b / \sigma_s$ stays constant within 10 %. As a consequence, a low concentration of bigger particles cannot be distinguished from a high concentration of smaller particles. However, for the case of nanomaterial characterization, the total volume of nanoparticles added to the sample is usually known.

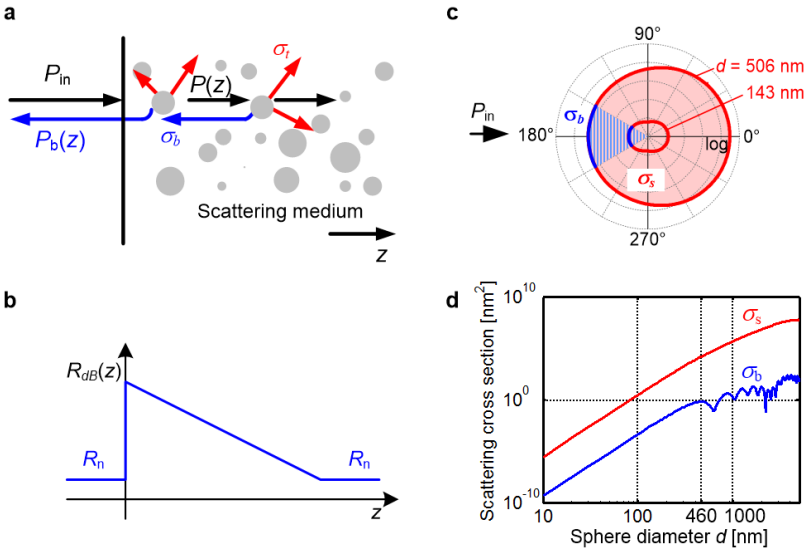

Figure 3.2: Concept of model-based dispersion state analysis and sizing of nanoparticles. **(a)** Single scattering model: Incident light is scattered at maximum once inside the medium. A light beam with power P_{in} enters the sample. At each particle (grey), a first portion (σ_b, blue) of the incident light in the respective depth z is scattered back into the numerical aperture of the optical system, a second portion (σ_t, red) is scattered into all other directions or is absorbed, and the remaining third portion (black) propagates deeper into the medium. **(b)** Schematic profile of the logarithmic backscattering factor $R_{dB}(z) = 10\lg(R_s(z))$. **(c)** Direction-dependent scattering lobes according to Mie's theory, plotted here for the example of polystyrene (PS) nanospheres (diameters 506 nm and 143 nm, refractive index $n_{PS} = 1.57$ at 1315 nm) in aqueous dispersion ($n_{H_2O} = 1.33$). σ_s: total scattering (red); σ_b: backward scattering (blue). **(d)** Total scattering σ_s and backscattering σ_b cross sections for non-absorbing polystyrene spheres in aqueous dispersion.

For an increasing degree of dispersion, the average size d of the agglomerates decreases and their volume number density N increases in proportion to d^{-3}. Together with the d^6-dependence of the scattering cross sections in the Rayleigh regime, this leads to an overall decrease of the scattering coefficients in proportion to d^3, which allows robust separation of particle size d and volume number density N. Note that this applies to non-absorbing particles only. If the extinction coefficient μ_t is dominated by the contribution of absorption rather than scattering, an increased degree of dispersion could lead to an increase of μ_t. This is due to the fact that the breaking-up of agglomerates exposes more particles from the inner region to the incident light. These particles from the inner region were formerly shielded from light by the absorbing outer shell, and did therefore not contribute to attenuation. If absorption dominates, the effect of increasing extinction with increasing number of separated absorbing particles can be exploited for the analysis of the dispersion state. We use this approach in the section on dispersion analysis of epoxy-CNT composites.

3.2.3 Image-based dispersion-state analysis

Although nanocomposites ideally feature a homogeneous distribution of nanosized fillers, in practice, microscale agglomerates cannot be completely avoided. The size of the agglomerates could reach several hundreds of micrometres, especially at the beginning of the so-called compounding process, which usually exploits shear forces to break up particle agglomerates into their nanoscale constituents. Therefore, a dispersion-state analysis suitable for process monitoring should be able to cope with nanometre to micrometre sized objects. This section is dedicated to imaging and analysis of agglomerates in the micrometre range.

Optical coherence tomography can be used to visualize agglomerates, if their dimensions exceed the spatial resolution δx, δy, δz of the imaging system in x, y and z-direction (about 10 µm), and if the backscattering is stronger than the background noise. Below these limits, an analysis based on a scattering-model has to be applied. To identify agglomerate regions with stronger backscatter within the OCT image, we use an image segmentation algorithm based on

seeded region growing [92]. For quantitative information related to agglomerate size and number, two independent parameters are extracted from the segmented images, namely the area fraction (AF) and the perimeter-to-area ratio (PAR) of the agglomerates, see Figure 3.3. The area fraction relates the image area covered by all identified agglomerates with individual area A_i to the entire imaging cross section A_{tot},

$$\text{AF} = \frac{\sum_i A_i}{A_{\text{tot}}}. \tag{3.3}$$

For a given volume fraction of the nanosize filler, and assuming spherical agglomerate shapes which are accurately detected by an ideal measurement system, the AF would be independent of the agglomerate diameter. This can be understood by the following consideration: Assume that each spherical agglomerate splits and decreases in radius by a factor of ν. The total amount of material remains constant, therefore the number of (smaller) agglomerates in the volume increases by ν^3, whereas the number of agglomerates in the measurement plane increases by ν^2. The average area A_i of each individual cross section in the measurement plane decreases in proportion to ν^2. Therefore the radius change of the agglomerates has no effect on AF. This would render AF as non-indicative for agglomerate analysis. For real measurement systems, however, a decreasing average agglomerate size will increase the number of agglomerates that are smaller than the detection threshold of the image-based analysis technique. In this case, a decrease of AF is observed which is correlated with a decreasing agglomerate size. In our experiments, the detection threshold is set to three times the standard deviation of the background noise floor in the image. While the threshold influences the measured percentage of the area fraction, our choice of the threshold level suffices to judge the dispersion of a certain sample type.

As a further parameter, the perimeter-to-area ratio (PAR) relates the sum of all agglomerate perimeters s_i to the sum of all agglomerate areas A_i,

$$\text{PAR} = \frac{\sum_i s_i}{\sum_i A_i} \tag{3.4}$$

Assuming agglomerates of equally distributed shapes, the PAR depends only on the average size of the agglomerates and is otherwise independent of the number density. A change in the average shape of all agglomerates during the dispersion process would influence the PAR, but this is not to be expected for typical dispersion processes that rely on milling or shear-strain-induced breaking of agglomerates. If the dimensions of each agglomerate decrease by a factor of ν, the perimeter decreases by ν, while the cross sectional area decreases by ν^2. Accordingly, the perimeter-to-area ratio of each agglomerate increases by a factor of ν, and the same applies to the overall PAR, independently of the filler content. Image-based analysis is applied to OCT measurements of nanocomposites both offline and during production.

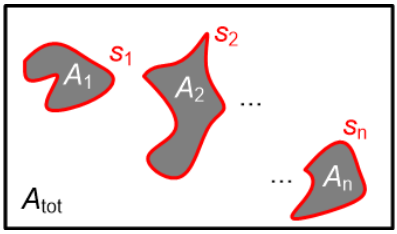

Figure 3.3: Illustration of agglomerate areas and perimeters in a cross-sectional OCT image. The total image cross section amounts to A_{tot}; the quantities $A_1 \ldots A_n$ denote the areas (grey) and the quantities $s_1 \ldots s_n$ (red) denote the perimeters of the agglomerates. The area fraction (AF) is a measure for total agglomerate content and relates the agglomerate areas $A_1 \ldots A_n$ to the total image cross section A_{tot}. The perimeter-to-area ratio (PAR) is a measure for the size of the found agglomerates and relates perimeters $s_1 \ldots s_n$ to the areas $A_1 \ldots A_n$.

3.3 Results and discussion

To prove the viability of OCT as a tool for characterization of nanoparticles and nanocomposite materials, we performed a series of experiments comprising accurate nanoparticle sizing as well as nanocomposite dispersion state analysis in liquid and solid materials. Our characterization employs image evaluation and a simplified model-based scattering analysis. We show that OCT methods are useful for measuring nanoscopic particle sizes as well as for

analyzing the dispersion of agglomerates in the micro- and millimetre regime. The technique can even cope with highly absorbing CNT-loaded materials and is well suited for in-line process control.

3.3.1 Model-based sizing of nanoscale particles

Polystyrene (PS) nanospheres (refractive index $n_{PS} = 1.57$) in aqueous dispersion (refractive index $n_{H_2O} = 1.33$) are used as a model system to prove the viability of OCT as a tool for model-based nanoparticle sizing. This model system offers higher refractive index contrast than the sample systems investigated in following sections (polyamide/clay: $n_{PA} = 1.59$, $n_{Clay} = 1.54$; polypropylene/clay: $n_{PP} = 1.49$, $n_{Clay} = 1.54$). All these samples offer sufficient backscattering levels. In this experiment, we characterize dispersed NIST-traceable polystyrene particles (BS-Partikel GmbH, Wiesbaden, Germany) with diameters of 143 nm and 246 nm. The results are depicted in Figure 3.4. The particle size is determined by fitting the calibrated single scattering model according to Eq. (3.2) to measured OCT depth scans as described in the previous section. We use three different samples S1, S2, and S3 with different diameters and particle concentrations expressed in weight-% (wt. %) of PS particles in the dispersion, see Figure 3.4 (d) and (e) for scanning electron images of the dried particles. The nominal size and concentration of the investigated dispersed particles amount to 143 nm at 2.0 wt. % for S1, 143 nm at 0.5 wt. % for S2, and 246 nm at 0.2 wt. % for S3, respectively. Figure 3.4 (a) depicts averaged OCT depth scans (light coloured circles) along with the curves of the fitted single-scattering model (bright colours). For the fit, measurement data have been taken into account only up to a depth of 1.8 mm (225 measurement points) to avoid inaccuracies by multiple scattering [93]. The extinction coefficient μ_t and the backscattering coefficient μ_b can be extracted from the fit: Sample S1 (143 nm, 0.5 wt.%): $\mu_{t1} = (85 \pm 23)\ m^{-1}$, $\mu_{b1} = (97.0 \pm 7.4)\times10^{-4}\ m^{-1}$; Sample S2 (143 nm, 2.0 wt.%): $\mu_{t2} = (352 \pm 26)\ m^{-1}$, $\mu_{b2} = (53.6 \pm 5.8)\times10^{-3}\ m^{-1}$; Sample S3 (246 nm, 0.2 wt.%): $\mu_{t3} = (125 \pm 7.5)\ m^{-1}$, $\mu_{b3} = (18.0 \pm 2.0)\times10^{-3}\ m^{-1}$. The error bounds refer to the standard deviation of the averages. Since the particle concentrations and hence the number densities N are known, we can translate

these coefficients directly to the scattering cross sections σ_s and σ_b, assuming that absorption of the PS particles can be neglected at the measurement wavelength around 1315 nm. The following total scattering σ_s and backscattering cross sections σ_b have been extracted: Sample S1 (143 nm, 0.5 wt.%): $\sigma_{s1} = (25.9 \pm 7.0)$ nm^2, $\sigma_{b1} = (29.7 \pm 2.3)\times10^{-4}$ nm^2; Sample S2 (143 nm, 2.0 wt.%): $\sigma_{s2} = (26.9 \pm 2.0)$nm^2, $\sigma_{b2} = (41.0 \pm 4.4)\times10^{-4}$ nm^2; Sample S3 (246 nm, 0.2 wt.%): $\sigma_{s3} = (488 \pm 29)$ nm^2, $\sigma_{b3} = (70.1 \pm 7.7)\times10^{-3}$ nm^2. The values given include the standard deviation of the averages. The cross sections σ_s and σ_b can be related to the diameters of the respective particles using Mie's theory [50], see Figure 3.4 (b). The total scattering cross section σ_s (left axis, red) and the backscattering cross section σ_b (right axis, blue) of polystyrene nanospheres dispersed in water are calculated and plotted as a function of the sphere diameter, assuming incident light of 1315 nm wavelength and a system aperture of 0.018 (1° half-angle).

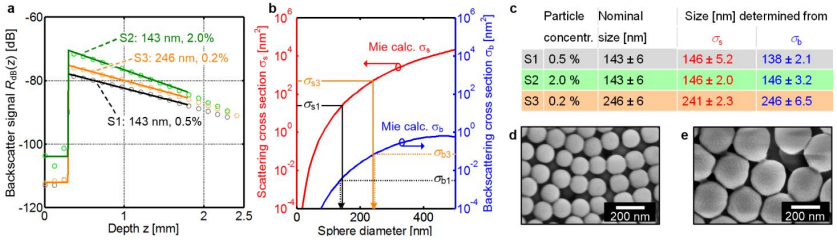

Figure 3.4: Size determination of sub-wavelength nanoparticles with OCT. **(a)** Measured OCT depth scans of aqueous dispersions of polystyrene (PS) nanospheres (S1: 143 nm diameter, 0.5 wt.%, grey circles: measurement, black line: fit; S2: 143 nm diameter, 2.0 wt.%, light green circles: measurement, green line: fit; S3: 246 nm diameter, 0.2 wt.%, light orange circles: measurement, orange line: fit), fitted with the calibrated single-scattering model according to Eq. (3.2). **(b)** Total scattering (red) and backscattering (blue) cross sections, according to Mie's theory for polystyrene spheres in water. Both scattering cross sections are compared with the measurements, depicted only for the samples S1 (σ_{s1}: total scattering cross section, σ_{b1} backscattering cross section) and S3 (σ_{s3}, σ_{b3}, respectively). Both parameters can be attributed to sphere diameters, horizontal axis. **(c)** Comparison of nominal particle sizes with measured sizes. Relative (absolute) deviations from the nominal values are maximal 4 % (5 nm). **(d,e)** Scanning electron micrograph (SEM) of the nanospheres having diameters of 143 nm and 246, respectively.

From the measurement fits in Figure 3.4 (a), the scattering parameters σ_{s1}, σ_{b1} for sample S1 and σ_{s3}, σ_{b3} for sample S3 are extracted. The sphere diameter can then be read from the Mie calculations displayed in Figure 3.4 (b), vertical arrows. For clarity, the analysis is only depicted for sample S1, but sample S2 yields very similar results.

The table in Figure 3.4 (c) summarizes the results as derived from scattering cross section σ_s and backscattering cross section σ_b, together with the associated standard deviations of the averages, and compares them with the nominal particle sizes and their standard deviations. The standard deviation measured by OCT can be lower than the standard deviation of the particle size distribution, since various particles contribute to one OCT measurement. Measurement errors may arise from refractive index uncertainties, where an uncertainty of 0.01 would lead to a size determination error of 2 nm to 4 nm. Relative deviations between nominally and measured particle sizes are below 4 %.

3.3.2 Model-based nanoscale dispersion-state analysis

Owing to the high sensitivity of the OCT technique, even strongly absorbing nanomaterials such as carbon-nanotube (CNT) composites can be analysed. This is a key feature, as CNT-loaded composites represent an important market segment [94]. Standard light scattering techniques like DLS or SLS are not applicable because the scattered or transmitted optical powers are small. Conventional CNT dispersion analysis relies either on thin material layers that are investigated in a light microscope (LM), or on the determination of macroscopic material parameters like the dielectric permittivity that can also indicate the dispersion quality [95]. For our experiments, we use a multi-wall CNT (MWCNT) dispersion in an epoxy resin (Araldite LY 556, Huntsman Advanced Materials GmbH, Basel, Switzerland). The samples contain 0.12 wt. % of MWCNT (NC7000, Nanocyl S.A., Sambreville, Belgium), and were prepared by 1, 3 and 5 milling cycles in a three-roll mill. We compare the results of OCT-based backscattering and extinction parameter analysis with the results of standard LM analysis as well as with rheological and dielectric measurements. For OCT measurements, the CNT-filled resin samples were filled

into cuvettes and heated up to a temperature of 50°C for melting the resin, thereby avoiding scattering from resin crystals.

The results of the dispersion analysis are shown in Figure 3.5. Conventional dispersion analysis of thin composite layers by light microscopy, see Figure 3.5 (a), reveals significant agglomerates after the first milling cycle. After three milling cycles, the size of agglomerates reduces. After five milling cycles, the light microscope images could lead to the conclusion that dispersion quality seems to decrease again, but other measurement techniques, like OCT analysis and rheological characterization, contradict this finding. Light microscopy for dispersion analysis, while being a state-of-the-art technique, suffers from small imaging areas. This could lead to an erroneous interpretation, if the agglomerate concentration is not spatially homogeneous over the whole sample. The same samples were investigated using OCT, see Figure 3.5 (b), which shows extinction coefficients μ_t and the backscattering coefficients μ_b in a two-dimensional plot. For each of the samples, we take ten measurements, each consisting of 5000 depth-scans which were taken while laterally moving the sample over a distance of 2 mm. The depth scans are averaged, and the extinction coefficient μ_t and the backscattering coefficient μ_b are extracted by fitting Eq. (3.2) to the measurement data. This has been repeated at ten different regions of each sample, each region corresponding to a cross in Figure 3.5 (b). Note that the particle sizes cannot be extracted from these data: In contrast to the situation for pure nanosphere dispersions used as a reference, the CNT agglomerates exhibit a large variety of shapes, and a Mie scattering theory based on simple spheres cannot be applied. Yet, the analysis of the extinction and backscattering coefficients suffices for a qualitative dispersion analysis. The horizontal and vertical error bars in Figure 3.5 (b) represent the average (solid dots) and the standard deviation of the measurements obtained for each sample. Although it is not possible to exactly discriminate between scattering and absorption, we may assume that the high extinction values of $5\ \mathrm{mm}^{-1}$ up to $15\ \mathrm{mm}^{-1}$ arise mainly from absorption of the CNT and only marginally from scattering. This is supported by strong reported absorption [96] of $1000\ \mathrm{mm}^{-1}$ due to separated CNT in composites with comparable concentrations. Consequently, we did not take multi-scattering into account. A

clear tendency with respect to the number of milling cycles can be seen: The more agglomerates are broken, the more isolated CNT can contribute to absorption and hence to the extinction μ_t, which rises significantly between one and three milling cycles, and increases slightly for five cycles. Simultaneously, the backscattering coefficient μ_b increases with the number of milling cycles and shows the same tendency as the extinction μ_t. The backscattering coefficient $\mu_b = \sigma_b N$, however, does not necessarily increase if the dispersion quality increases so that the agglomerates become smaller and their number N becomes larger. It is impossible to state in general how smaller agglomerates contribute to the backscattering inside the light receiving aperture, because σ_b strongly depends on the angle dependency of the backscattering for the respective agglomerate shape. In our specific case, μ_b increases with an increasing degree of dispersion, and therefore allows a qualitative judgement of the state of the sample dispersion.

These results of the OCT analysis are confirmed by a rheological characterization of the relative permittivity ε_r. For this purpose, the dispersions were investigated using a rheometer (MCR 501, Anton Paar GmbH, Graz, Austria) in combination with a programmable LCR bridge for measuring inductance, capacitance and resistance (HM 8118, HAMEG Instruments GmbH, Mainhausen, Germany). The rheometer consists of two parallel rotatable plates at a separation of s = 1 mm. The sample dispersion fills the gap between the plates, which are isolated electrically from each other and which are connected to the LCR bridge for measuring the capacitance. During a measurement, one of the plates performs an oscillating rotation. The amplitude b_r of the oscillation at the outer radius of the plate, related to the plate separation s results in the strain amplitude $\gamma = b_r / s$. Both the measurement setup and the measurement procedure are described in detail in Ref. [95]. The relative permittivity is measured at a frequency of 1 kHz and increases monotonically from the pure epoxy material over 1 to 3 to 5 milling cycles: This indicates a continuous improvement of dispersion quality, see Figure 3.5 (c), since an increasing number of CNT are separated from agglomerates and contribute to the electric polarization of the nanocomposite. Note that the rheological measurements themselves introduce shear strain into the samples, which could lead to further

exfoliation of CNT from the agglomerates and hence to an increase of the relative permittivity during characterization of the samples after three milling cycles. This additional exfoliation might be not possible for the mixture after one milling cycle (insufficient exfoliation) and five milling cycles (largely complete exfoliation). At higher strain amplitudes (not shown), the separated CNT align in parallel to the rheometer plates and thus perpendicularly to the electric field. In this case the CNT cease to influence the permittivity.

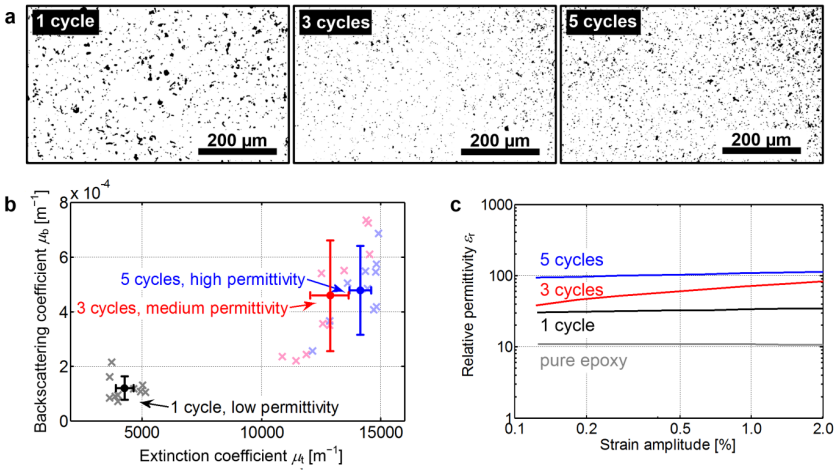

Figure 3.5: OCT characterization of highly absorbing epoxy/carbon nanotube (CNT) composite materials. Comparison to conventional characterization techniques and macroscopic material properties. The composite was milled over 1, 3 and 5 cycles in a three-roll-mill to improve dispersion. **(a)** Conventional dispersion state analysis by light microscopy of thin composite layers. Black areas are attributed to agglomerates. **(b)** OCT-determined backscattering μ_b and extinction μ_t coefficients, measured in 10 different spatial regions (crosses) of each sample (average: solid dots; standard deviations: horizontal and vertical error bars). **(c)** Rheologic dielectric characterization of the relative permittivity ε_r as a function of applied shear strain after 1, 3, and 5 milling cycles. The relative permittivity increases monotonically from the pure epoxy material over 1 to 3 to 5 milling cycles, indicating an increase in the separation of the CNT.

In contrast to the microscopy analysis and the permittivity measurement, OCT characterizes the heated sample without any further preparation. The results correlate well with the permittivity measurement and with the number of dispersion cycles. In contrast to light microscopy, OCT also reveals the increase in dispersion quality between the third and the fifth dispersion cycle. This experiment demonstrates that OCT metrology is useful to characterize even highly absorbing nanomaterials, outperforming by far the elaborate and time consuming conventional light microscopy method.

3.3.3 Image-based dispersion-state analysis for microscale agglomerates

For experimentally assessing the ability of the OCT technique to analyse nanocomposites with large agglomerates, composites of polyamide (PA; Badamid B70, Bada AG, Bühl, Germany) and nanoclay particles with 5 wt.% concentration were prepared in a compounding extruder [97]. For controlling the dispersion quality during fabrication, one batch of samples was prepared from a clay with modified surface (I.34, Nanocor Inc., Hoffman Estates, IL, USA), the other one was prepared from unmodified clay (PGN, Nanocor Inc.). The surface modification is expected to lead to an improved dispersion state and to decreased sizes of agglomerates as compared to the unmodified clay. After compounding, all samples are granulated without further sample processing. Cross-sectional images (B-scans) are taken from the granules with our laboratory OCT system. Representative B-scans from the PA/nanoclay composite without and with surface modification are shown in Figure 3.6 (a) and (b), where the pixel brightness indicates measured backscattering. The sample with no modification, Figure 3.6 (a) shows large lengthy bright areas, indicating large clay agglomerates that extend over several hundreds of micrometres, whereas the sample with modification, Figure 3.6 (b), features small bright spots only from which small agglomerates can be inferred. The image segmentation algorithm detects bright regions automatically; the corresponding borders are drawn as red lines.

For each sample type, three B-scans are taken, segmented, and the area fraction (AF) as well as the perimeter-to-area ratio (PAR) are calculated for each measurement. Figure 3.6 (c) and (d) display the average AF and the average PAR for both sample types along with the corresponding error bars showing the standard deviation of the averages. A significant decrease in the AF is obtained when the surface of the clay filler is modified (AF_{mod} = 2.0 % ± 0.4 %) as compared to the filler without surface modifications (AF_{unmod} = 5.3 % ± 0.8 %), Figure 3.6 (c). This indicates that a surface modification significantly decreases the agglomerate size such that a substantial fraction of agglomerates becomes smaller than the size detection threshold of the image analysis. This is in accordance with the observation that the cross-sectional image of the surface-modified clay composite exhibits a large number of bright spots, each of which contains only a few pixels, see Figure 3.6 (b). At the same time, the PAR increases significantly with modification of the filler surface (PAR_{unmod} = 132 mm^{-1} ±8.2 mm^{-1}, PAR_{mod} = 178 mm^{-1} ±4.1 mm^{-1}) which confirms the decrease in average agglomerate size, Figure 3.6 (d).

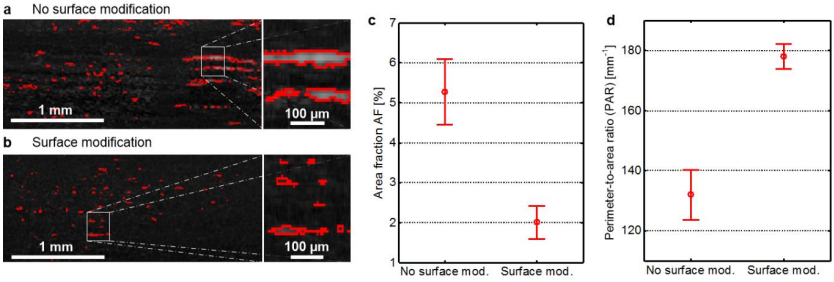

Figure 3.6: Image-based dispersion-state analysis for microscale agglomerates, showing the impact of chemical surface modification on dispersibility. **(a)** Cross-sectional image (B-Scan) of a PA/nanoclay composite with 5 wt-% nanoclay content without surface modification. Bright spots (strong backscattering) with red borders indicate agglomerates. Right part: magnified section. **(b)** Cross-sectional image of a PA/nanoclay-composite with surface-modified clay particles having the same concentration as the sample in (a). Right part: magnified section. **(c)** Area fraction (AF) covered by detected agglomerates. The circles denote average values of the three samples, and the error bars indicate the standard deviation of the average. **(d)** Perimeter-to-area ratio (PAR) of the detected agglomerates. The circles denote average values of the three samples, and the error bars indicate the standard deviation of the average.

These experiments prove the viability of image-based OCT analysis to characterize the dispersion state of samples with relatively large agglomerates sized from a few micrometres to hundreds of micrometres. The quantitative evaluation of further dispersion-related parameters like agglomerate shape and number would further increase the reliability and robustness of our technique.

3.3.4 Demonstration of in-line dispersion-state analysis

Nanocomposite development is hampered by rather long development cycles, which are dominated by time consuming off-line characterization. In this section, OCT is demonstrated to be well-suited for continuous dispersion-state monitoring in a production environment.

In the following experiment, a production-scale twin-screw compounding extruder (Leistritz GmbH, Nuremberg, Germany) is used for production of a polypropylene(PP)/nanoclay composite with a mass throughput of 6 kg/h. The applied host material is PP (R352-08R, Dow Chemical, Midland, MI, USA) and the nanosized filler is a nanoclay (Cloisite 15A, Southern Clay Products, Gonzales, TX, USA). The screws introduce shear into the polymer melt filled with nanoparticles and thus disperse the particles [97]. With this extruder, nanocomposites were dispersed with different revolution speeds. In general, increasing speed comes with higher energy input into the material and causes a better nanoparticle dispersion [21]. In order to characterize the dispersion state of the PP/clay melt during production, the extruder has been equipped with the OCT probe for in-line process monitoring, see Figure 3.1 (c). The probe is mounted to a sensor port of the extruder located at the end of the machine close to the die. The optical window of the probe is in direct contact with the main stream of the extruded nanoparticle loaded polymer melt. With the OCT probe, A-scans of the medium underneath the probe window are measured continuously. The flow of the melt causes a continuous movement of the material seen by the OCT measurement beam, thereby replacing a lateral movement of the measurement beam in conventional measurements. This results in a temporal change of the backscatter signal, which can be interpreted as 2D image data, where one dimension corresponds to time and the other

dimension is the usual imaging depth measured from the probe window, see Figure 3.7.

Figure 3.7 (a), (b) and (c) show the in-line OCT data for the screw revolution speeds 200 rpm, 500 rpm and 800 rpm, respectively. Note that, due to non-uniform mass flow as a function of depth, it not possible to directly map the measurement time (horizontal axis) to spatial coordinates of the sample. Bright spots indicate strong backscatter and are attributed to agglomerates. The straight horizontal line at $z \approx 0$ originates from permanent reflections at the probe window. With higher screw speed and accordingly higher shear strain inside the material, fewer agglomerates are visible indicating an improvement in dispersion quality. At the highest screw speed of 800 rpm, almost no agglomerates are visible. This impression is also confirmed by quantitative dispersion-related parameters. Since the measurement is performed as a function of time rather than as a function of lateral position, a perimeter-to-area ratio in the strict sense as defined by Eq. (3.4) cannot be calculated.

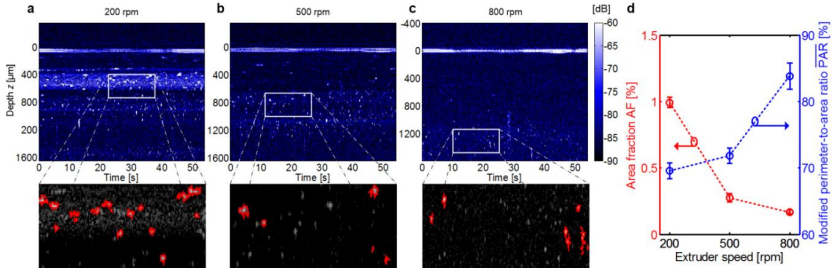

Figure 3.7: Demonstration of in-line dispersion-state analysis during operation of a compounding extruder. The OCT measurement beam is fixed, the vertical axis of the OCT images indicates the imaging depth and the horizontal axis corresponds to the measurement time. Bright spots: strong backscatter of agglomerates. Straight horizontal line at $z \approx 0$: permanent reflections at the probe window. Material system: polypropylene/nanoclay. Mass flow: 6 kg/h. Clay content: 1 %. Bottom: magnification after segmentation. **(a)** OCT scan at 200 rpm. **(b)** OCT scan at 500 rpm. **(c)** OCT scan at 800 rpm. **(d)** Quantitative analysis of the dispersion state by area fraction (AF) and modified perimeter-to-area ratio $\overline{\mathrm{PAR}}$ from five OCT scans. The circles denote average values of the five scans, and the error bars indicate the standard deviation of the averages.

Instead, we use a modified quantity $\overline{\mathrm{PAR}}$, which essentially corresponds to the PAR except that both, the agglomerate perimeters s_i and the agglomerate areas A_i, are expressed by pixel numbers rather than by physical lengths and areas. Note that $\overline{\mathrm{PAR}}$ is a dimensionless quantity in contrast to PAR, which has the unit m^{-1}. The results are depicted in Figure 3.7 (d), where the circles denote average values from five OCT scans, and the error bars denote the respective standard deviations of the averages. With increasing speed, the area fraction AF reduces, and the PAR rises. Both quantities indicate that the agglomerates inside the material flow become smaller corresponding to a better dispersion quality of the composite. These results reveal a clear relationship between operation parameters of the machine and OCT-measured dispersion parameters. This is the first demonstration of an in-line dispersion-state analysis in a nanocomposite production line. The results encourage the application of our technique to more material systems for controlling multiple production parameters.

3.4 Conclusions

In this work, we present a novel and a highly attractive approach to nanomaterial analysis applied to nanoparticles and nanocomposites. The method uses optical coherence tomography (OCT) and model-based parameter extraction. Our approach enables detection and quantification of nanoparticles and agglomerates over a wide range of size scales: Image segmentation of OCT data sets is well suited for dispersion-state characterization of nanocomposites with agglomerates in the micrometre range, whereas model-based scattering analysis lends itself to size determination of nanoparticles below the resolution limit. We elaborate the measurement technique along with theoretical models and demonstrate the viability of the procedure in a series of proof-of-principle experiments. A wide variety of material systems is investigated by our experiments: A first demonstration shows accurate OCT-based nanoparticle sizing. An in-situ dispersion-state analysis characterizes strongly absorbing CNT composites in liquid media. Finally, we perform in-line monitoring of the compounding process in a state-of-the-art production line. Major challenges in

industrial applications are the stringent requirements with respect to mechanical stability and size of the OCT system. These requirements can be met by integration of interferometer and detection system on a silicon photonic chip [98]. We believe that OCT has the potential to fill a metrology gap in the emerging field of nanocomposite technology. We conclude that OCT metrology opens new directions in material analysis, both in laboratory and production environments.

[End of Publication P2]

4 Nanoparticle size and shape characterization using PS-OCT

The following chapter is a manuscript intended for publication in a peer-reviewed journal. Slight adaptions have been made to match the format and the structure of this thesis.

Nanoparticles of diverse shapes play an increasingly important role in medical and technical applications. Their tiny size comes along with unique physical properties, which are tightly coupled to their actual size and shape. In consequence, continuous quality control in nanoparticle fabrication is mandatory. Transmission or scanning electron-microscopy is a costly and time-consuming method, yielding results from small sample batches only. Here we show that polarization-sensitive optical coherence tomography allows to determine the size and the shape of nanoparticles in a quick process with small technical effort and with no need for laborious sample preparation. The technique relies on measuring the depth and polarization-dependent backscatter and on evaluating the results by a semi-analytical model. We found the backscatter measurement to be sufficiently sensitive on gold nanorod geometry to enable diameter determination with 6.2 nm accuracy and maximum deviation in aspect ratio measurement of 10 %. These experiments correspond to the first demonstration of quantitative nanoparticle shape determination with optical coherence tomography.

4.1 Introduction

Nanoparticles are attractive for both scientific examinations and technical applications. Their size is in or below the range of the optical wavelength and is thus only one to four orders of magnitude bigger than an atomic diameter, thus leading to huge surface-to-volume ratios. As a consequence, in contrast to bulk materials, size and shape of the particles govern their physical properties

and become the essential parameter for targeted material design. As an example, the shape-dependent surface plasmon resonance frequency of metallic nanorods allows to use them as highly-sensitive refractive index sensors [99,100]. Moreover, gold and platinum nanoparticles can be used as chemical catalysts for which the reaction rate depends significantly on size and shape [14,101], and also the cellular uptake of gold nanorods into biological tissue, when used as imaging markers, turns out to be shape- and size-dependent [9]. The same is true for soft-matter nanorods as nanocarriers in tumour therapy [102]. Nanoclays form layered structures and thus feature a large lateral extension and small height. This special shape accounts for their outstanding barrier properties [74], when incorporated into a polymer host material. The aspect ratio of carbon nanotubes (CNT) determines their ability to build up electrically conductive paths inside isolating matrix materials. Transparent polymers can thus become conductive and might offer an alternative to expensive indium tin oxide (ITO) [12]. All these applications have in common that size and shape of the nanoparticles are crucial to the macroscopic material properties and thus to the final performance of the product. In this context, characterization of the nanostructure is of highest relevance, either indirectly by characterization of the final macroscopic properties or directly using imaging, scattering or filtration techniques.

State-of-the-art size and shape characterization of nanoparticles mainly relies on microscopic imaging. This requires high-resolution techniques such as scanning-electron microscopy (SEM) [16], transmission electron microscopy (TEM) [17] or atomic force microscopy (AFM) [103,104]. In all cases, sample preparation is laborious and costly and might create artefacts, e.g. agglomeration effects during the drying process in sample preparation. Moreover, SEM, TEM and AFM are limited to small sample volumes, which are not necessarily representative of the entire batch. Light scattering techniques, in contrast to imaging methods, are viable tools for determining particle size distributions from large sample volumes. Static light scattering (SLS) uses angle-resolved and/or spectrally resolved detection of scattered light [22,23] and needs a rather complex optical setup, when large scattering angles are to be taken into account. Dynamic light scattering (DLS) methods make use of temporal

fluctuations of interference patterns of scattered light to calculate the hydrodynamic diameter of particles within the respective solvent [75]. Relying on the observation of the Brownian motion of single particles, the technique is limited to rather low concentrations. Both SLS and DLS preferentially provide information on particle size, while particle shape cannot be determined [24]. X-ray diffraction (XRD) [77] or X-ray scattering (SAXS) [78] can be used to reveal the atomic or molecular structure inside the material. However, expensive instrumentation and a small probing region limit the application range of these methods to small batch sizes. Tunable resistive pulse shaping (TRPS) [25] measures the particle size by observing the ionic current through a small pore. Once a particle passes this pore the ionic flow is affected for a certain time. After calibration, this technique allows accurate determination of particle size distributions. Information on particle shape however cannot be extracted. Particle size distributions can also be measured using centrifugal sedimentation techniques, where particles with different dimension are separated by differences in their sedimentation speed in presence of centrifugal forces [25]. While this technique is applicable to a broad size range, high experimental effort is necessary and no information on particle shape is obtained.

Optical coherence tomography (OCT) represents a combination of light scattering techniques with optical imaging is [1,28,79]. OCT provides three-dimensional imaging data from the bulk of a sample and avoids expensive sample preparation. Previous demonstrations of nanoparticle analysis using OCT have shown size determination with nanometre accuracy [10] and nanocomposite dispersion-state characterization [10]. Microparticles have been investigated using image-based analysis [81]. OCT has been applied to particle diffusion measurements and showed particle size-dependent temporal variations [82,83]. Angle-resolved OCT has proven to be able to measure particle sizes down to 5 µm [84], by evaluating the angular-dependent scattering lobes with Mie's theory. Gold nanorods have been differentiated from collagen cells, exploiting their strong polarization-cross talk in OCT measurements [105]. While micro- and nanometre particle size determination has been addressed by some OCT-based methods, the exact determination of

anisotropic particle shapes, e.g., particle sizes in long and short dimension, still needs to be shown.

In this section we demonstrate that polarization-sensitive OCT (PS-OCT) [59] allows accurate determination of both nanoparticle size and shape. By evaluation of backscatter signals in different polarizations and by comparison to electromagnetic field simulations of differently shaped particles, we demonstrate precise determination of length and diameter of gold nanorods in aqueous dispersion. Without the need for sample preparation, this technique allows to measure nanometre particle dimensions in statistically relevant volumes of several cubic millimetres. We determine size and shape of gold nanorods in a unimodal aqueous dispersion by comparing measured scattering parameters with simulation results. Our samples cover particles which range from 15 to 50 nm in particle diameter and from 1 to 16 in aspect ratio. In practice, this technique can be extended to the analysis of many nanoparticles with prolate or oblate shape as long as the refractive index contrast to the surrounding media is sufficient and absorption is moderate.

4.2 Measurement principle: Size- and shape-dependent backscattering

Light scattering methods allow size and shape measurements beyond the resolution of optical imaging systems. The analysis presented here links the geometry of the particles to their scattering properties and relates those to polarization-sensitive backscattering measurements with a PS-OCT system. First, we introduce the applied scattering model on the basis of nanospheres and their size-dependent scattering. Second, we expand the model to non-spherical scatterers using a polarization-dependent scattering model.

For the analysis, a single-scattering model [89] is used, under the assumption that incident light is scattered at maximum once inside the medium, which is appropriate for weakly scattering samples and for the analysis of moderate depths [90]. Figure 4.1 depicts the scattering model in two exemplary media: nanospheres, Figure 4.1 (a), and non-spherical particles Figure 4.1 (c), with

their respective polarization-dependent backscattering curves Figure 4.1 (b) and Figure 4.1 (d). As shown in the case of nanospheres Figure 4.1 (a), a light beam with incident power P_{in} and polarization E_{in} enters the sample. At each particle (grey), one part of the incident light at depth z is scattered back into the numerical aperture of the system, another part is scattered into other directions or is absorbed (black), and the remainder propagates deeper into the medium. Mie's theory [50] is applicable to the calculation of angle-dependent scattering amplitudes of spherical particles with sizes in the range of or smaller than the optical wavelength of the incident light. The scattering amplitudes are dependent on size of the spheres, refractive index of sphere and surrounding material, as well as on the optical wavelength. Thus, observation of the angle-dependent scattering can be used for size analysis of nanospheres. In the case of spherical scatterers, the polarization of the output field $E_{out,m}$ is the same as the incident polarization E_{in} [50,106,107]. This is an indication of spherecity of the scatteres, if their size is far below the wavelength and multiple scattering can be neglected. The total scattering cross section σ_s and the absorption cross section σ_a of a particle sum up to the extinction cross section σ_t. For an ensemble of particles with number density N, the extinction coefficient can be expressed as $\mu_t = N\sigma_t$. Analogously, the backscattering cross section into the −180° direction is given by σ_b, and the backscattering coefficient is $\mu_b = N\sigma_b$. The depth-dependent decay $dP(z)/dz = -\mu_t P(z)$ of the forward travelling power $P(z)$ follows an exponential function $P(z) = P_{in}\, e^{-\mu_t z}$. For a given depth z, the power is scattered back from inside a depth element δz, and is captured by the numerical aperture of the system, $P_b(z) = \mu_b \delta z P(z) e^{-\mu_t z}$, where $e^{-\mu_t z}$ accounts for the losses in the back propagation path. In an OCT measurement the depth-dependent backscattering factor $R_0(z) = P_{in}/P_b(z) + R_n$ is measured, including a system dependent noise floor R_n, which defines the sensitivity of the system expressed as minimum measurable sample reflectivity, see Section 2.1.4. In summary, the scalar single-scattering model, which omits polarization effects is given by

$$R_0(z) = \mu_b \delta z\, e^{-2\mu_t z} + R_n \,. \tag{4.1}$$

In practice, the measured backscattering signal depends on further effects, which need to be determined in a calibration step. This comprises the decay of the coherence function of the frequency-swept laser, the divergence of the measurement beam, and the absorption of the material, which surrounds the scatterers. These influences are taken into account by including two calibration factors [10,91] q and Q in the single-scattering model according to Eq. (4.1),

$$R_{\mathrm{s}}(z) = Q\mu_{\mathrm{b}}\delta z \, \mathrm{e}^{-2(\mu_{\mathrm{t}}+q)z} + R_{\mathrm{n}} \tag{4.2}$$

Both calibration factors are determined by comparison of measured backscatter of a NIST-traceable polystyrene particle standard with 246 nm sphere diameter in 0.5 wt.% aqueous dispersion (BS-Partikel GmbH, Wiesbaden, Germany) to model calculations according to Eq. (4.1).

A sketch of a semi-logarithmic plot $R_{\mathrm{dB}}(z) = 10\,\lg(R_{\mathrm{s}}(z))$ of both the polarization-maintaining backscattering factor $R_{\mathrm{m}}(z)$ (blue) and of the cross-polarization backscattering factor $R_{\mathrm{c}}(z)$ (red) is shown in Figure 4.1 (b). With no polarization conversion, the cross-polarization backscatter is zero, and the measured signal is given by the associated noise level.

Light scattering of particles with non-spherical shape can lead to backscatter with altered polarization, see Figure 4.1 (c). In general, light scattering is caused by the excitation of dipole oscillations inside the particles and the associated radiation of light. The orientation of the dipoles and thus the polarization of the emitted light depend on both incident polarization and particle geometry [50]. For elongated particles, dipoles are preferentially excited in the direction of the long axis of the particle, thus showing a polarization change of backscattered with respect to the incoming light. With an ensemble of randomly oriented particles, all random backscatter polarizations sum up, and an average backscatter polarization is obtained, which differs the more from the incident polarization, the more the particles' shape deviate from that of a sphere.

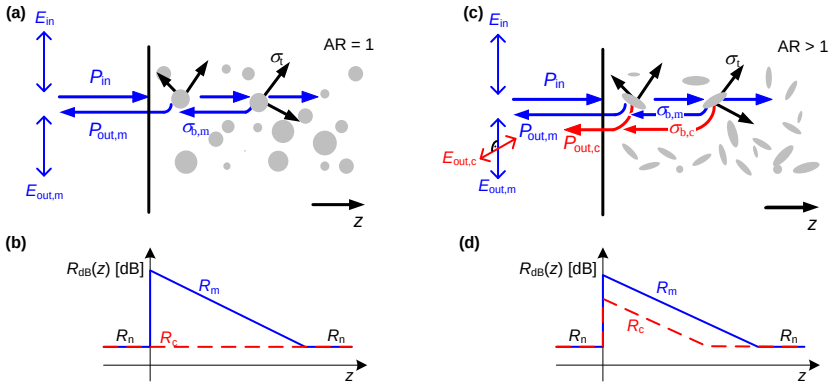

Figure 4.1: Polarization-sensitive scattering-model-based size and shape analysis of nanoparticles. **(a)** Scattering of a linearly polarized laser beam with power P_{in} inside a dispersion of spherical nanoparticles, with aspect ratio AR = 1. Concentration and refractive index contrast are low enough to assume single scattering inside the medium. The input polarization E_{in} is considered vertical here (blue colour). Backscattering of spherical particles in the −180° direction maintains the polarization, so the backscattering cross section $\sigma_b = \sigma_{b,m}$ equals the polarization-maintaining backscattering cross section. The total extinction cross section is given by σ_t. Light that is neither scattered nor absorbed propagates deeper into the medium. $P_{out,m}$ denotes the output power of light in same polarization as of the input light, $\vec{E}_{in} \parallel \vec{E}_{out,m}$. **(b)** A single-scattering model leads to a polarization maintaining backscattering factor R_m, describing the depth-dependent backscattering factor into the polarization of incidence. In case of spherical particles the cross-polarization backscattering factor R_c is zero. Together with a system-dependent noise level R_n, both factors are plotted in dB-scale along the depth axis z. **(c)** Scattering in a medium with non-spherical particles of aspect ratio AR > 1. The input polarization (vertical) is only partially maintained, and the backscattering cross section $\sigma_b = \sigma_{b,m} + \sigma_{b,c}$ is given by the sum of both the polarization-maintaining component $\sigma_{b,m}$ and the cross-polarized component $\sigma_{b,c}$ (red). Accordingly, output light is polarized partially in parallel to the input $\vec{E}_{in} \parallel \vec{E}_{out,m}$ and orthogonal $\vec{E}_{in} \perp \vec{E}_{out,c}$. $P_{out,m}$ and $P_{out,c}$ denote the corresponding backscattered powers. **(d)** In contrast to the case in (b), the cross-polarized backscattering factor R_c is non-zero for non-spherical particles. The ratio R_c/R_m can be taken as a measure for non-sphericity of the investigated particles.

Analogously to Figure 4.1 (a), a beam with power P_{in} and an electric field orientation E_{in} is incident on the sample. Interaction of the non-spherical particles with the incident light is expressed by the total extinction cross section σ_t, the

polarization-maintaining backscattering cross sections $\sigma_{b,m}$ describing polarization maintaining backscatter, and the cross-polarization backscattering cross section $\sigma_{b,c}$. The backscattered light is hence composed of light with maintained polarization with power $P_{out,m}$ and electric-field $E_{out,m}$, which is polarized parallel to the incident field, and of light with power $P_{out,c}$, and electric-field $E_{out,c}$, which is polarized orthogonally to the incident field.

The semi-logarithmic depth-dependent backscatter signal of a sample with non-spherical particles is depicted in Figure 4.1 (d). In comparison to the scalar case, the backscattering coefficient $\vec{\mu}_b = N\vec{\sigma}_b$ is vectorial,

$$\vec{\mu}_b = \begin{pmatrix} \mu_{b,m} \\ \mu_{b,c} \end{pmatrix}, \tag{4.3}$$

and the backscatter signal is given by

$$\vec{R}_s(z) = \begin{pmatrix} R_m(z) \\ R_c(z) \end{pmatrix} = \begin{pmatrix} \mu_{b,m} \\ \mu_{b,c} \end{pmatrix} Q\delta z \, e^{-2(\mu_t + q)z} + R_n \, . \tag{4.4}$$

The difference of the two backscattering coefficients, $\mu_{b,m}$ and $\mu_{b,c}$, leads to offsets between the logarithmic plots $R_m(z)$ and $R_c(z)$ in Figure 4.1 (d). This difference is denoted as polarization cross talk $\eta = 10 \lg(\mu_{b,c} / \mu_{b,m})$, which we define in dB. The decay of both curves is the same, since the particles in the sample are randomly oriented and the extinction is thus dependent on input or output polarization. While the backscatter curve in the scalar model contains information on particle size and number density, the vectorial polarization-dependent model additionally supplies information on particle shape. In the following sections, dispersions of particles with different diameters and aspect ratios are characterized by measuring their polarization-dependent backscattering signals.

4.3 Measurement results

To determine the viability of our concept, we analyse aqueous dispersions of polystyrene nanospheres and aqueous dispersions of gold nanorods with

different aspect ratios. The analysis is performed using a polarization-sensitive OCT system, which is described in detail in Section 4.6. Measurements of the nanospheres show negligible polarization conversion, which is in accordance with theoretical considerations [50,106,107]. For nanorods, we find shape-dependent polarization conversion. By comparing the measurement data to electromagnetic simulations, we find that diameter and aspect ratio (AR) of the rods can be determined with nanometre accuracy.

In our experiments, aqueous dispersions of gold nanorods with $d_G = 25$ nm diameter and average lengths of $l_{G1} = 102$ nm (sample G1) and $l_{G2} = 256$ nm (sample G2; both types of nanorods from Nanopartz Inc., Loveland, Colorado, USA) have been characterized with the PS-OCT system. These rods feature respective aspect ratios of $AR_{G1} = 4$ and $AR_{G2} = 10$ and number densities of $N_{G1} = 5.7\times10^{18}$ m^{-3} and $N_{G2} = 1.1\times10^{17}$ m^{-3}, corresponding to weight concentrations of 0.54 wt. % and 0.026 wt. %, respectively. For comparison, additionally a sample (S4) with spherical particles ($AR_{S4} = 1$), containing an aqueous dispersion of polystyrene nanospheres of diameter of $d_{S4} = 246$ nm, number density of $N_{S4} = 6.4\times10^{17}$ m^{-3} and weight concentration of 0.5 wt. % is investigated. For preparation, all samples were filled into quartz glass cuvettes with broad optical transmittance. In Figure 4.2 (a-c), OCT measurement results are depicted along with the associated scanning electron microscope (SEM) images in Figure 4.2 (d-f) of the dried particles. The measurement results consist of two curves, polarization-maintaining backscatter $R_m(z)$ and cross-polarized backscatter $R_c(z)$, both as a function of depth inside the sample. Figure 4.2 (a) depicts the results of the microsphere sample (S4), with $R_m(z)$ showing an exponential decay inside the sample ($z > 0$). The data for $z < 0$ is defined by the noise level. By tilted incidence on the sample surface, facet reflections could be avoided. The solid curves represent a fit of the scattering model in Eq. (4.4) to the measured data (light coloured). Applying Mie's theory to $R_m(z)$, the spheres' sizes can be extracted with nanometre accuracy, as we have demonstrated previously [10]. The cross-polarized backscatter $R_c(z)$ is more than 20 dB below $R_m(z)$. Since the polarization extinction ratio of the system is around 20 dB, this data can be considered to be below the noise level and no scattering model fit is reasonable. The complete

polarization maintenance of the backscatter leads to the conclusion that the sample particles are completely spherical. The SEM picture, Figure 4.2 (d), of the dried particles of sample S4 confirms this finding. The gold nanorod sample G1 with AR of 4, see Figure 4.2 (b), shows an exponential decay both for the polarization maintaining backscatter $R_m(z)$ and the cross-polarized backscatter $R_c(z)$.

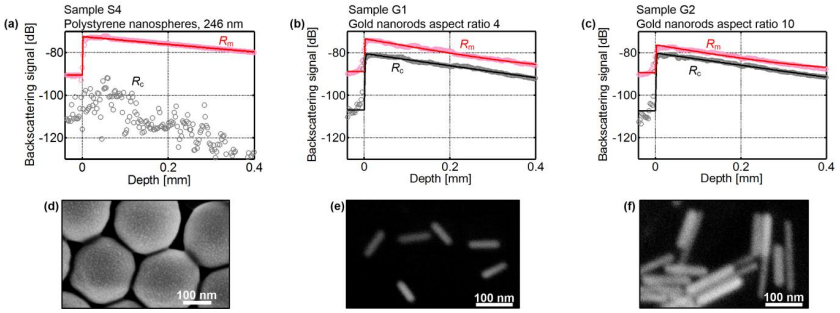

Figure 4.2: PS-OCT measurements and scanning-electron microscope (SEM) images of nanoparticles with different shapes. **(a)** Sample S4: PS-OCT depth scan of polystyrene nanospheres with d_{S4} = 246 nm diameter in 0.5 wt.-% aqueous dispersion. R_m denotes polarization-maintaining backscatter (light red: measurement, bright red: single-scattering model fit), and R_c denotes cross-polarized backscatter. The polarization maintaining curve is dominating the cross-polarized trace by more than 20 dB, hinting to an aspect ratio of the particles close to unity. Fluctuations of the cross-polarized part are due to the measurement noise around −100 dB. **(b)** Sample G1: PS-OCT measurement of gold nanorods with d_{G1} = 25 nm diameter and aspect ratio of AR_{G1} = 4 in 0.54 wt. % aqueous dispersion. The signal decay with depth corresponds to the total scattering and absorption cross sections of the gold nanorods. The cross-polarization curve (grey: measurement, black: single scattering fit) is below the polarization-maintaining backscatter, and the polarization conversion amounts to η_{G1}= −6.9 dB. The noticeable cross term is in accordance with the expected polarization conversion by scattering from non-spherical nanoscale objects. **(c)** Sample G2: PS-OCT measurement of gold nanorods with d_{G2} = 25 nm diameter and aspect ratio of AR_{G2} = 10 in 0.026 wt. % aqueous dispersion. In comparison to (b), the polarization conversion is stronger and amounts to η_{G2} = −3.7 dB. **(d-f)** Scanning electron microscope images of the respective dried nanoparticles: **(d)** Sample S4: polystyrene nanospheres of d_{S4} = 246 nm diameter, **(e)** Sample G1: gold nanorods of d_{G1} = 25 nm diameter and AR_{G1} = 4, **(f)** Sample G2: gold nanorods of d_{G2} = 25 nm diameter and AR_{G2} = 10. As can be seen in (e) and (f), the length of the rods is not completely uniform and the nominal values can be regarded as average values.

The decay coefficient of both curves is same, as expected in Eq. (4.4), and the polarization cross talk is measured to be $\eta_{G1} = -6.9$ dB. This noticeable cross talk is attributed to a clear deviation of the scatterers from a spherical shape, which is confirmed by the SEM image in Figure 4.2 (e). Compared to G1, the sample G2 shows even higher polarization cross talk $\eta_{G2} = -3.7$ dB, see Figure 4.2 (c). This behaviour is expected as the AR is increased to 10. The SEM image in Figure 4.2 (f) confirms the elongated particle shape. Further, a variation of rod length around the nominal value of 256 nm can be noticed.

The following table summarizes the determined scattering coefficients and cross sections as well as the polarization cross talk.

Table 4.1: Scattering coefficients, cross sections and polarization cross talk, determined from the measurements in Figure 4.2 using the polarization-sensitive single scattering model in Eq. (4.4). Sample S4 is used for calibration of μ_t and $\mu_{b,m}$, for this reason the values of μ and σ are nominal values.

Sample	μ_t	$\mu_{b,m}$	σ_t	$\sigma_{b,m}$	η
S4	307 m^{-1}	0.0424 m^{-1}	4.79×10^{2} nm^2	6.62×10^{-2} nm^2	< −20 dB
G1	1117 m^{-1}	0.0331 m^{-1}	1.96×10^{2} nm^2	5.80×10^{-3} nm^2	−6.9 dB
G2	1059 m^{-1}	0.0170 m^{-1}	9.63×10^{3} nm^2	1.54×10^{-1} nm^2	−3.7 dB

4.4 Shape determination by comparison of simulation and measurements

In the following, the measured scattering parameters are compared to simulation. For the determination of the particles' size and shape, a set of simulations with varying geometries is performed and used for comparison.

The selected electromagnetic simulation technique relies on a commercially available fully vectorial integral equation solver that is part of CST Microwave Studio [108]. The solver, which follows a Method of Moments (MoM) method, a rigorous full-wave technique for solving open-boundary electromagnetic problems, is used for calculating the surface integral of the electric and magnetic field at the scattering particle. This method is especially

recommended for the calculation of scattering cross sections and thus fits perfectly to our needs. An alternative numerical method, which allows scattering calculations of non-spherical particles is basing on the Discrete-Dipole Approximation (DDA) [109]. In this method, the specific particle geometry is adapted by discrete dipoles of which the mutual excitation is taken into regard along with the excitation by the incident field. The technique is used for nanorod investigations, but shows weaknesses in calculation of gold nanorods at infrared wavelengths [110], which is the regime of our analysis. A further calculation approach for non-spherical particles or small agglomerates thereof is to make use of the Rayleigh-Debye-Gans theory (RDG) [50]. In this approach, the arbitrarily shaped particle is subdivided into small Rayleigh scatterers, which are assumed to be unperturbed by each other. In a comparison [111] to other calculation techniques, RDG was found appropriate for limited size parameters $kl < 0.3$ and refractive index differences $\Delta n < 2$, with the angular optical wavenumber $k = 2\pi / \lambda$ and the particles longest dimension l. Although the RDG approach is appropriate for some types of non-spherical particles, the aforementioned conditions do not hold for our sample types. A promising method for calculation of scattering and extinction of particles as used in our experiment is the T-Matrix Method [112,113], which relies on the expansion of scattered and initial field in suitable vector spherical wave functions, and on linking the respective expansion coefficients in a so-called T-matrix. This approach is applicable to many particle types and could be a further option in future calculations.

For the CST calculations, the selection of the proper material properties of gold turned out to be crucial to the simulation results. Muskens [114] identified the complex refractive indices measured by Johnson [115] to be fitting best to gold particles of nanometre size. These values were interpolated to a wavelength of 1.3 µm and used for a Drude material model [116] within the simulations. In the simulation environment, the nanorods were built up from a cylindrical body and two hemispherical tails. We investigate a variety of differently shaped nanorods with diameters of 15 to 50 nm and aspect ratios of 1 to 16. For these particles, the absorption cross section and the spatial and polarization-dependent distribution of the scattering power were simulated and

averaged over random rod orientations to represent the scattering properties of nanorods dispersed in water. Averaging of the scattered powers from the individual particles is possible, since the particle concentration is small and light can thus be assumed to be scattered at most once. From integrating these angular scattering cross sections over the complete solid angle of 4π, the scattering cross section σ_s is obtained. The extinction cross section $\sigma_t = \sigma_s + \sigma_a$ results from taking the absorption cross section σ_a into account as well. The polarization-maintaining backscattering cross section $\sigma_{b,m}$ results from integration of the polarization-maintaining angular scattering cross section in the backward direction over 1° half-angle, which corresponds to the numerical aperture of the system. The polarization-resolving simulation allows to detect the cross-polarized backscatter separately from the polarization-maintaining backscatter, which is used for calculation of the polarization cross talk η.

Figure 4.3 depicts the simulation results and compares them to the nanorod measurements. The subplots in Figure 4.3 (a-c) show simulated extinction and backscattering cross sections as well as polarization cross-talk as a function of diameter as well as AR. The term diameter is used here for the short axis of the particle, whereas AR×d gives the extent along the long axis, see Figure 4.3 (f). For particle diameters between 15 and 40 nm, simulations were performed with a step size of 5 nm, and for diameters between 40 and 50 nm, the step size was increased to 10 nm. The step size in AR was 1 for AR = 1 … 14, and 2 for AR = 14 … 16, leading to 105 data points in total. For display and comparison to measurements, all results have been interpolated using a 2D spline interpolation. Figure 4.3 (a) shows the extinction cross section σ_t, Figure 4.3 (b) shows the polarization-maintaining backscattering cross section $\sigma_{b,m}$ and Figure 4.3 (c) shows the polarization cross talk η. Within the simulation domain, σ_t generally rises with both particle diameter and extinction ratio. In the vicinity of the plasmonic resonances around AR of 6 and 14 the extinction is highest. For $\sigma_{b,m}$ the trend is analogous, although not identical to the results in Figure 4.3 (a). The polarization cross-talk η is almost independent from diameter but shows strong dependence on AR, especially if AR is small. The black lines in the three subfigures indicate the values measured for sample G1 and G2. Table 4.2 summarizes the simulation results for the

geometries given by samples G1 and G2. The measured values, see also Table 4.1, are denoted for comparison. Measurement and simulation of σ_t and $\sigma_{b,m}$ show agreement with respect to the order of magnitude. The polarization cross-talk η differs at most by 2.71 dB between simulation and measurement.

Table 4.2: Comparison of simulated and measured extinction and backscattering coefficients, σ_t, $\sigma_{b,m}$, respectively, as well as the polarization cross talk η.

Sample	σ_t	$\sigma_{b,m}$	η
G1 simulated	1.26×10^2 nm^2	3.18×10^{-3} nm^2	−4.69 dB
G1 measured	1.96×10^2 nm^2	5.80×10^{-3} nm^2	−6.90 dB
G2 simulated	6.22×10^3 nm^2	2.31×10^{-1} nm^2	−3.67 dB
G2 measured	9.63×10^3 nm^2	1.54×10^{-1} nm^2	−3.70 dB

In principle, the determination of pairs of d and AR for a set of two measured parameters, e.g. σ_t and $\sigma_{b,m}$, is possible. However, in practice, each pair out of the three measured parameters (σ_t, $\sigma_{b,m}$, η) would lead to a different solution for d and AR, since measurement and simulation provide a limited accuracy. For this reason, all three parameters are taken into account by calculating the (d, AR)-pair which provides in sum the lowest relative difference of simulation and measurement. First, the single ratios of each measured parameter to the simulated parameters are calculated. Since the extinction and backscattering cross sections span a wide range of several magnitudes, comparison on a logarithmic scale seems to be favourable. The polarization cross talk η is expressed in logarithmic dB-units already. Thus, the absolute logarithmic values of the ratios read

$$\begin{aligned} \Delta\sigma_t &= \left| 10\lg\left(\frac{\sigma_t^{(\mathrm{meas})}}{\sigma_t^{(\mathrm{sim})}} \right) \right| \\ \Delta\sigma_{b,m} &= \left| 10\lg\left(\frac{\sigma_{b,m}^{(\mathrm{meas})}}{\sigma_{b,m}^{(\mathrm{sim})}} \right) \right| , \\ \Delta\eta &= \left| \eta^{(\mathrm{meas})} - \eta^{(\mathrm{sim})} \right| \end{aligned} \tag{4.5}$$

where the superscript denotes either measurement (meas) or simulated (sim) data. The single ratios, Eq. (4.5), are divided by their individual maxima within the simulation domain, and after this normalization the total ratio is calculated

$$\Delta_{\mathrm{tot}} = \frac{1}{3}\left(\frac{\Delta\sigma_{\mathrm{t}}}{\max\left(\Delta\sigma_{\mathrm{t}}\right)} + \frac{\Delta\sigma_{\mathrm{b,m}}}{\max\left(\Delta\sigma_{\mathrm{b,m}}\right)} + \frac{\Delta\eta}{\max\left(\Delta\eta\right)} \right). \tag{4.6}$$

The factor of 1/3 keeps the result in the [0,1] range but does not affect the calculation of the particle shape. Figure 4.3 (d-e) shows Δ_{tot} versus d and AR in colour-coded plots for both measurements of sample G1, Figure 4.3 (d), and of sample G2, Figure 4.3 (e). The white cross indicates the position of lowest total deviation. In the case of sample G1 with nominal diameter of 25 nm and nominal AR of 4, see Figure 4.3 (d), Δ_{tot} is low (blue coloured) in an area reaching from AR of 3 and diameter of 50 nm to AR of 6 and diameter of 15 nm. The rod geometry with lowest deviation from simulation is found at a diameter of 26.75 nm and at AR of 4.1. This deviates from the nominal values by only 1.75 nm in diameter and 2.5% in AR. In the case of sample G2 with nominal diameter of 25 nm and AR of 10, see Figure 4.3 (e), Δ_{tot} is low for AR > 6. In this case, the sensitivity in diameter is less pronounced. The smallest total ratio is found at a diameter of 18.8 nm and AR of 9. This amounts to a deviation of 6.2 nm in diameter and 10% in AR.

Table 4.3 summarizes the OCT measurement results, which are in good agreement with the particle parameters obtained from SEM imaging. Note that the OCT measurement captures backscatter from a multitude of particles at once, thus averaging out deviations of individual particles from the nominal shape values.

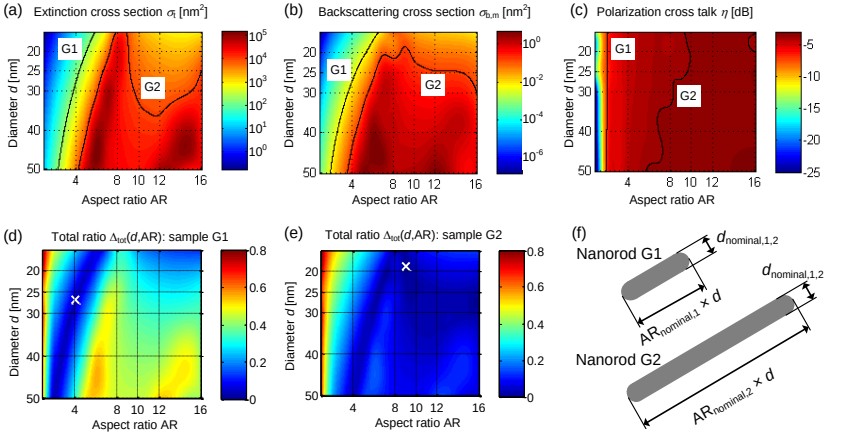

Figure 4.3: Particle shape determination by comparison of OCT-measured scattering parameters and electro-magnetic scattering simulations. Subfigures **(a-c)** show averaged scattering parameter simulations for an aqueous dispersion of randomly oriented gold nanorods. The horizontal and vertical axes denote aspect ratio AR and diameter d, respectively. **(a)** Total extinction cross section σ_t, **(b)** polarization maintaining backscattering cross section $\sigma_{b,m}$, and **(c)** polarization cross talk η. Extinction cross section σ_t and backscattering cross section $\sigma_{b,m}$ increase generally with particle diameter d and aspect ratio AR and show high values at the plasmonic resonances, e.g., around AR = 6. The crosstalk η increases with AR. The black lines indicate the values extracted from the OCT measurements of sample G1 and sample G2, which contain nanorods with nominal diameter $d_{nominal,1,2}$ = 25 nm and nominal aspect ratios $AR_{nominal,1}$ = 4 and $AR_{nominal,2}$ = 10. **(d,e)** Total ratio Δ_{tot} of measurement and simulation comprising all three parameters (σ_t, $\sigma_{b,m}$, η). **(d)** Total ratio Δ_{tot} of the simulations and the measured parameters extracted from sample G1, see Eq. (4.6). **(e)** Total ratio Δ_{tot} of the simulations and the measured parameters extracted from sample G2, see Eq. (4.6). The white crosses show minimum total ratios and thus indicate the estimated particle diameter $d_{meas1,2}$ and aspect ratio $AR_{meas1,2}$. Table 4.3 lists the results for both samples. **(f)** Schematic drawing of both nanorod geometries G1 and G2, along with the nominal diameters $d_{nominal,1,2}$ and the respective aspect ratios $AR_{nominal,1}$ and $AR_{nominal,2}$.

Table 4.3: Estimated particle diameters d_{meas} and aspect ratios AR_{meas} compared to the nominal specifications $d_{nominal}$, $AR_{nominal}$. The absolute and relative deviations between measurement and nominal values are given by ε_d and ε_{AR}.

Sample	d	ε_d	AR	ε_{AR}
G1 nominal	25 nm	1.8 nm (7 %)	4	0.1 (2.5 %)
G1 measured	26.8 nm		4.1	
G2 nominal	25 nm	6.2 nm (25 %)	10	1.0 (10 %)
G2 measured	18.8 nm		9.0	

4.5 Discussion

The ramp-up of nanotechnology-driven industry demands fast and reliable techniques for quality control. In this work, we demonstrated that polarization-sensitive OCT offers precise size and shape measurement of nanoparticles, along with no sample preparation. The large probing volume of several cubic millimetres and the prospect of integrability into production lines, as well as the instantaneous output of characterization results are unique among the nanoparticle shape characterization tools.

This work for the first time demonstrates quantitative characterization of size and shape of nanoparticles using PS-OCT. Nevertheless, the technology has some practical limitations, which we will discuss in the following. The technique is constrained to the analysis of light scattering media, which are neither fully transparent, nor strongly absorbing, however the range of possible materials is broad, as has been shown in the analysis of strongly absorbing CNT-loaded materials [10]. A further restriction is given by the aspect ratio, which should not exceed AR = 10, when exact quantitative shape determination is aimed for. Aspect ratios below this limit cover most practically relevant nanoparticles from nanospheres to nanorods, but excludes, e.g., the differentiation of high-AR nanowhiskers from long nanorods. For larger aspect ratios, see Figure 4.3, the extinction cross section, the backscattering cross section and the polarization cross talk showed to be less sensitive to further aspect ratio changes. In our experiments, the particle size distributions have been narrow. Particles with broader size and shape variations could possibly be

distinguished by trend, but a quantitative shape determination down to nanometre accuracy, as has been shown here, would be hampered.

In conclusion, we have shown that PS-OCT allows to accurately determine size and shape of monodisperse gold nanorods having 25 nm diameter and lengths of 102 nm and 256 nm. We used a polarization-sensitive OCT setup, which we calibrated with respect to both power level and polarization. We measured three parameters: extinction cross section, backscattering cross section and polarization cross talk. Shape and size information were extracted by comparison to electro-magnetic scattering simulations of randomly dispersed particles, and the results are in fair agreement with the particle dimensions obtained from SEM-based imaging. We believe PS-OCT offers an attractive option for simple and rapid nanoparticle characterization with reasonable instrumentational effort as needed, e.g., in in-line or on-line quality control.

4.6 Methods

The swept-source PS-OCT system used in this work is illustrated in Figure 4.4. In general, an OCT system measures the strength and the position of a multitude of scatterers along a light path in a sample. To this end, the electric field that is back reflected from the sample into the numerical aperture of the system is superimposed with a reference field originating from the same swept laser source. The superposition leads to optical frequency dependent interference patterns on a photodetector. The variation of signal amplitude with laser frequency is connected to the depth-dependent back reflection profile of the sample by a Fourier transform [28], see also Chapter 2.1.1. In our experiment we use a swept-source laser with central wavelength of 1315 nm and a wavelength scanning range of 1260−1370 nm, a scan rate of 1 kHz, and 10 dBm (10 mW) average output power (model s3, Micron Optics Inc., Atlanta, GA, USA). A first fibre-based directional coupler (CPL1) is used to split the power among the sample path (SP) and the reference path (RP). The reference path contains a free-space section allowing precise matching of the SP and RP lengths. Backscattered light from the sample and light travelling along the RP

is superimposed in a second fibre-based coupler (CPL2) and coupled to a polarization-sensitive balanced photodetector (PS-BD, model INT-POL-1300, Thorlabs Inc., Newton, NJ, USA) offering 15 MHz electrical bandwidth. Polarization controllers (PolC) are used for matching the polarization in both detector arms, and for setting the reference arm polarization to 45°, thus providing the same reference arm power in both orthogonal polarizations. The PS-BD consists of two polarizing beam splitters (PBS) and a balanced detector (BD) for each of the polarizations. The balanced detection principle suppresses relative intensity noise (RIN) from the strong RP light and enables a large dynamic range and a high sensitivity defined by the smallest measurable sample reflectivity of −110 dB. The electrical signal is digitized by a 16 bit analogue-to-digital converter (ADC, model ATS660, Alazar Technologies Inc., Pointe-Claire, Canada) and processed by a personal computer (PC). The sample path comprises fibre collimator (FC), rotatable quarter-wave plate (QWP) for polarization variation, a pair of galvo scan mirrors for lateral 2D beam scanning, a scan lens and the sample under test. The SP exists in two configurations: First the polarization calibration setup (top) with additional rotatable polarizer (Pol) and plane mirror instead of a sample, and second the measurement setup (bottom).

For the describing the polarization of light within the PS-OCT system, we use the Jones formalism [117], where the electric field $\vec{E}(\omega,t)$ of polarized light is represented by the Jones vector $\vec{J}$. The Jones vector consists of two complex elements J_x, J_y with the normalized field amplitudes $\cos(\alpha)$, $\sin(\alpha)$, of each of the orthogonal field components in x and y direction, as well as their common phase δ and individual phases $-\varphi$ and $+\varphi$. Thus, the electric field is $\vec{E}(\omega,t) = A\mathrm{e}^{\mathrm{j}(\omega t-kz)}\,\vec{J} = A\,\mathrm{e}^{\mathrm{j}(\omega t-kz)}\mathrm{e}^{\mathrm{j}\delta}\left(\mathrm{e}^{-\mathrm{j}\varphi}\cos(\alpha)\vec{e}_x + \mathrm{e}^{+\mathrm{j}\varphi}\sin(\alpha)\vec{e}_y\right)$.

The transmission through a linear optical system is described by a Jones matrix **J**, transforming input Jones vectors to output Jones vectors. If multiple optical systems are concatenated, their individual Jones matrices are multiplied, and reverse transmission [69] of a unitary, optical reciprocal element with forward propagation matrix **J** results in

$$\mathbf{J}_{\mathrm{rev}} = \begin{pmatrix} m_1 & -m_3 \\ -m_2 & m_4 \end{pmatrix}, \quad \text{with } \mathbf{J} = \begin{pmatrix} m_1 & m_2 \\ m_3 & m_4 \end{pmatrix}. \tag{4.7}$$

The aim of a PS-OCT measurement is the determination of the backscattering of the sample as a function of depth and polarization. This can be expressed by a Jones matrix

$$\mathbf{J}_{\mathrm{s}} = \frac{1}{R_{\mathrm{S}}(z)} \begin{bmatrix} R_{xx}(z) & R_{yx}(z) \\ R_{xy}(z) & R_{yy}(z) \end{bmatrix} \tag{4.8}$$

with the backscattering coefficient $R_{ij}(z)$ denoting backscattering of incident polarization i into backscattered polarization j, where i, j can each be x (horizontal) or y (vertical orientation). The division by the total backscattering $R_{\mathrm{S}}(z)$ is necessary to normalize the Jones matrix. According to Eq. (4.4), the sample backscatter of randomly oriented single-scattering particles only distinguishes polarization maintaining $R_{\mathrm{m}}(z)$ from cross-polarized backscatter $R_{\mathrm{c}}(z)$, thus in this case the sample Jones matrix can be simplified to

$$\mathbf{J}_{\mathrm{s}} = \frac{1}{R_{\mathrm{S}}(z)} \begin{bmatrix} R_{\mathrm{m}}(z) & R_{\mathrm{c}}(z) \\ R_{\mathrm{c}}(z) & R_{\mathrm{m}}(z) \end{bmatrix}. \tag{4.9}$$

The measurement setup was built up with standard single-mode fibres (SMF) instead of polarization-maintaining fibres (PMF). In PMF, both principal polarization axes feature different group refractive indices, which imply different group velocities, which in turn cause spurious signal peaks in the OCT measurement. Using an SMF instead avoids spurious peaks but does not maintain the incident polarization. Hence, a polarization calibration step is necessary before performing a sample measurement. This is done using the calibration setup depicted in Figure 4.4 (top). In this step, the Jones matrix $\mathbf{J}_{\mathrm{sys}}$ describing the propagation of backscattered light through the fibre-optic system towards the PS-BD is determined as well as the input polarization $\bar{J}_{\mathrm{in}}$ of the light, which is emitted from the SP fibre towards the sample.

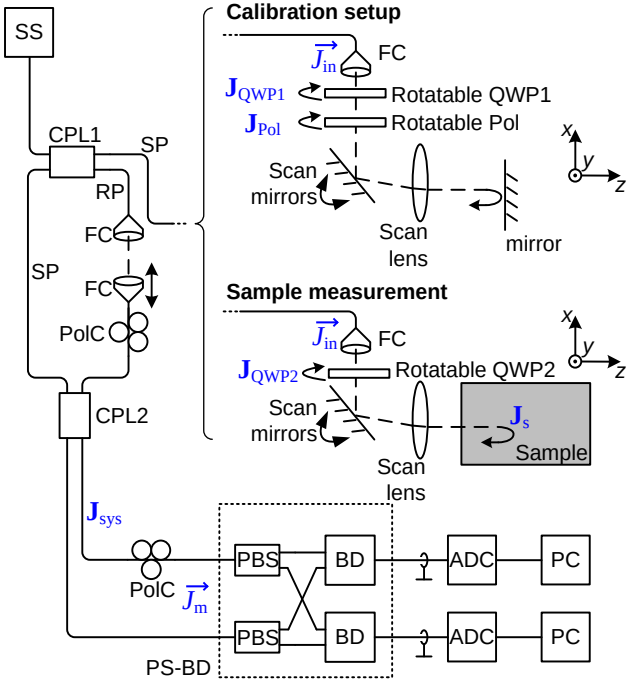

Figure 4.4: Setup schematic of the fibre-based polarization-sensitive swept-source optical coherence tomography setup used in this work. SS: swept-wavelength source, scanning range 1260-1370 nm; CPL1,2: fibre-based directional coupler; SP: sample path; RP: reference path; FC: fibre collimator; PolC: polarization controller; PS-BD: polarization-sensitive balanced detector, consisting of two polarization beam splitters (PBS) and two balanced detectors (BD); ADC: analogue-to-digital converter; PC: personal computer. For sample measurements, the sample arm comprises a free-space propagation section with a rotatable quarter-wave plate (QWP), scan mirrors, scan lens and sample. For calibration purposes, the sample is replaced by a plane mirror, and a rotatable polarizer (Pol) is added to the free-space section in the sample arm. Jones vectors and matrices are denoted in blue. $\vec{J}_{\mathrm{in}}$: Jones vector of the input polarization leaving the FC towards sample or towards calibration setup; $\mathbf{J}_{\mathrm{QWP1,2}}$: Jones matrix of the QWP1,2; $\mathbf{J}_{\mathrm{Pol}}$: Jones matrix of the polarizer; $\mathbf{J}_{\mathrm{s}}$: Jones matrix of the sample; $\mathbf{J}_{\mathrm{sys}}$: Jones matrix of the fibre-optic system from FC at the sample or calibration measurement head to the PBS at the PS-BD; $\vec{J}_{m}$: Jones vector, measured by the PS-BD.

The polarization measured at the PS-BD results from the concatenation of all transmitted optical elements

$$\vec{J}_{\mathrm{m,cal}} = \mathbf{J}_{\mathrm{sys}}\, \mathbf{J}_{\mathrm{QWP1,rev}}\left(\vartheta_{\mathrm{Q}}\right) \mathbf{J}_{\mathrm{Pol,rev}}\left(\vartheta_{\mathrm{P}}\right) \mathbf{J}_{\mathrm{M}}\, \mathbf{J}_{\mathrm{Pol}}\left(\vartheta_{\mathrm{P}}\right) \mathbf{J}_{\mathrm{QWP1}}\left(\vartheta_{\mathrm{Q}}\right) \vec{J}_{\mathrm{in}}\,, \tag{4.10}$$

which describes propagation of $\vec{J}_{\mathrm{in}}$ through the quarter-wave plate with $\mathbf{J}_{\mathrm{QWP1}}\left(\vartheta_{\mathrm{Q}}\right)$ at an angle ϑ_{Q} of the fast axis with respect to the horizontal direction, the polarizer with $\mathbf{J}_{\mathrm{Pol}}\left(\vartheta_{\mathrm{P}}\right)$ at an angle ϑ_{P} with respect to the horizontal direction, the back-reflection at the plane mirror described by $\mathbf{J}_{\mathrm{M}}$, the propagation back through polarizer $\mathbf{J}_{\mathrm{Pol,rev}}\left(\vartheta_{\mathrm{P}}\right)$ and QWP1 $\mathbf{J}_{\mathrm{QWP1,rev}}\left(\vartheta_{\mathrm{Q}}\right)$ and finally through the fibre optic system with matrix $\mathbf{J}_{\mathrm{sys}}$ towards the detector.

To determine both $\mathbf{J}_{\mathrm{sys}}$ and $\vec{J}_{\mathrm{in}}$, multiple measurements of $\vec{J}_{\mathrm{m,cal}}$ are necessary and performed at angular positions of the QWP1 of $\vartheta_{\mathrm{Q}} = 0°$ to 165° in steps of 15° combined to angular positions of the polarizer of $\vartheta_{\mathrm{P}} = 0°$ to 150° in steps of 30°. With 72 measurements in total, the system is over-defined, and a least-squares based fit allows robust determination of both $\mathbf{J}_{\mathrm{sys}}$ and $\vec{J}_{\mathrm{in}}$. The calibration is valid until fibres are moved or until a temperature drift causes a change of the fiber birefringence. In practice, the system is calibrated right before a measurement session. Here, all sample measurements use the same calibration.

The configuration for the actual sample measurement is shown in Figure 4.4 (bottom). In contrast to the calibration setup, the polarizer is removed and the mirror is replaced by the sample. The measured Jones vector is given by

$$\vec{J}_{\mathrm{m}} = \mathbf{J}_{\mathrm{sys}}\, \mathbf{J}_{\mathrm{QWP2,rev}}\left(\vartheta_{\mathrm{Q}}\right) \mathbf{J}_{\mathrm{S}}\, \mathbf{J}_{\mathrm{QWP2}}\left(\vartheta_{\mathrm{Q}}\right) \vec{J}_{\mathrm{in}}\,. \tag{4.11}$$

Now, only $\mathbf{J}_{\mathrm{s}}$ is unknown, and for a robust determination thereof, $\vec{J}_{\mathrm{m}}$ is measured at various positions of the QWP2 from $\vartheta_{Q} = 0°$ to 165°, with a step size of 15°. A least-squares fitting procedure reveals $\mathbf{J}_{\mathrm{s}}$, which we verified by using a linear polarizer as sample and determined its angular position with an accuracy of 3°.

5 Optical coherence tomography system on a silicon photonic chip

This chapter corresponds to publication [P1] with slight adaptations to match the format and the structure of this thesis. With the preceding chapters OCT has proven to be a powerful tool for the characterization of nanoparticles and nanocomposite materials. However, current systems are not suitable for many industrial environments, where often robust, small-sized and cost-effective systems are required. These challenges can be addressed by integrated-optical systems, with silicon as the material platform of choice, see Chapter 1.3.

[Begin of Publication P1]

Optical coherence tomography system mass-producible on a silicon photonic chip

Optics Express; Volume 24; Issue 2; pp. 1573-1586; January 2016
DOI: 10.1364/OE.24.001573

S. Schneider[1], M. Lauermann[1], P.-I. Dietrich[1,2], C. Weimann[1],

W. Freude[1,2] and C. Koos[1,2]

[1] Karlsruhe Institute of Technology (KIT), Institute of Photonics and Quantum Electronics (IPQ), 76131 Karlsruhe, Germany.
[2] Karlsruhe Institute of Technology (KIT), Institute of Microstructure Technology (IMT), 76344 Eggenstein-Leopoldshafen, Germany.

Miniaturized integrated optical coherence tomography (OCT) systems have the potential to unlock a wide range of both medical and industrial applications. This applies in particular to multi-channel OCT schemes, where scalability and low cost per channel are important, to endoscopic implementations with stringent size demands, and to mechanically robust units for industrial applications. We demonstrate that fully integrated OCT systems can be realized using the state-of-the-art silicon photonic device portfolio. We present two different implementations integrated on a silicon-on-insulator (SOI) photonic chip, one with an integrated reference path (OCT*int*) for imaging objects in distances of 1 mm to 6 mm from the chip edge, and another one with an external reference path (OCT*ext*) for use with conventional scan heads. Both OCT systems use integrated photodiodes and an external swept-frequency source. In our proof-of-concept experiments, we achieve a sensitivity of −64 dB (−53 dB for OCT*int*) and a dynamic range of 60 dB (53 dB for OCT*int*). The viability of the concept is demonstrated by imaging of biological and technical objects.

5.1 Introduction

Optical coherence tomography (OCT) [1,28] looks back on great advances in the past decades. Micrometer-range resolution in volumetric imaging opened a wide field of applications reaching from ophthalmology in medical diagnostics [87] to particle and defect characterization in materials science [80,88]. While current OCT systems are still assembled from discrete components, optical integration offers the prospect of compact low-cost mass-producible implementations. Especially in endoscopic applications as well as in industrial surface and distance metrology, integrated systems can comply with the demands in size, mechanical robustness, temperature stability and cost. An arrangement of multiple parallel OCT systems becomes feasible, allowing the simultaneous recording of depth scans at different positions (B-scan). Silicon photonics is a particularly attractive platform for integration of OCT systems, lending itself to large-scale photonic-electronic integration on the basis of mature high-yield CMOS processes that are offered by widely available foundry services [118].

Early in 2014, we introduced the first integrated silicon-photonic OCT system with surface imaging capabilities, comprising the interferometer and on-chip photodetectors [119]. In the same year, Yurtsever *et al.* demonstrated a silicon-photonic OCT system and showed a sensitivity of −62 dB, yet with off-chip photodetectors [120]. Recently, a silicon photonic optical combiner with integrated photodiodes was used as a polarization-diverse receiver for a fiber-based swept-source OCT system [121]. However, for completing the OCT interferometer, external couplers and circulators are used. Other realizations of integrated OCT systems rely on silicon nitride and silicon oxynitride waveguides, where both swept-source [122] and spectral-domain implementations have been shown. These demonstrations comprise, e.g., spectral-domain OCT chips based on arrayed waveguide gratings (AWG) [123], which have been used for characterization of biological samples [124]. Yet, silicon nitride and silicon oxynitride integration platforms are limited to passive components only such as waveguides and power splitters, and hence must be always complemented by external photodetectors. This limits the potential for large-scale integration.

In this paper we demonstrate the first fully integrated silicon photonic OCT system, where receiver and interferometer components are monolithically integrated on a single chip, and where only the swept-laser source (SS) and optional fiber-based delay lines are external to the chip. The experiments build upon the state-of-the-art silicon photonic device portfolio and demonstrate the advantages in size, cost and robustness inherent in monolithic integration. Based on our recent results [119] we investigate two system concepts, one with a fixed internal integrated reference path (OCT*int*), and one with external reference path with variable length (OCT*ext*). With the compact OCT*int* system, a lens at the chip edge focuses the swept-source light to the sample and collects the backscattered radiation. The OCT*ext* system allows the use of a conventional OCT scan head positioned remote from the chip. We achieve sensitivities down to –64 dB (–53 dB for OCT*int*) and demonstrate imaging of both technical and biological samples. The sensitivities of our current OCT implementations are limited by relative intensity noise (RIN) and on-chip backscatter. Further improvement is possible by using optimized integrated

components and by reducing reflections at the chip edges. Each of the OCT circuits occupies an on-chip area of less than 0.4 mm^2.

This chapter is organized as follows: In Sect. 5.2 the concept and the implementation of the OCT*int* and OCT*ext* systems is introduced. In Sect. 5.3 the sensitivity and the dynamic range of the systems are discussed. Sect. 5.4 is dedicated to the evaluation of the performance of both systems by demonstrating two-dimensional and three-dimensional imaging of technical and biological samples. A summary and an outlook are given in Sect. 5.5.

5.2 Silicon photonic OCT systems and experimental setup

Both the OCT*int* and OCT*ext* systems use the principle of swept-source OCT [28]. In general, an OCT system measures the position and the strength of a multitude of scatterers along a light path in a sample at various distances $z - z_r$ from a reference plane at z_r. To this end, the electric field E_s that is backscattered from a sample is compared in amplitude and phase to a reference field E_r. Both the sample and the reference field are derived from the same external optical swept-wavelength source. In an interferometer arrangement, sample and reference fields are superimposed on a (balanced) photodetector, the output current of which contains patterns resulting from interference of the backscattered field with the reference field. From these patterns, the amplitude and the position $z - z_r$ of the backscatter along the light path can be obtained by Fourier analysis of the photocurrent [28]. The backscatter strength denotes the ratio of backscattered optical power to optical power incident on the sample. For an optimum sensitivity, the optical length difference between the return path from the sample and the reference path should be small compared to the coherence length l_c of the source [47].

The integrated OCT configurations presented in this work are depicted in Figure 5.1 and Figure 5.2 and are described in more detail in the subsequent sections. In each of the implementations, the photonic integrated circuits (PIC) comprise passive waveguides and 3-dB couplers (CPL) based on multimode

interference (MMI), forming an interferometer structure which is connected to on-chip germanium photodiodes (PD). Silicon photonics allows particularly compact implementations: Both OCT systems were co-integrated on the same chip along with a large number of further optical circuits for various applications – the on-chip area occupied by each of the OCT circuits is less than 0.4 mm^2, and is dominated by the contact pads of the photodetectors which could be further reduced in size. As an external light source, we use a commercially available swept-source laser (Santec HSL-2100-ST) featuring a center wavelength of 1315 nm and a scanning range of 110 nm. The source is coupled to the PIC by either a lensed fiber (LF) or a polymer microlens (PL). All waveguides leading to chip facets are equipped with tapers narrowing towards the facet, designed for the full width at half maximum (FWHM) spot size of 1.9 µm of the lensed fibers. An external polarization controller (PolC) is used to precisely excite the quasi-TE mode of the on-chip waveguides. The interference signal is recorded by two balanced on-chip photodiodes, which are specified to have a bandwidth of 20 GHz. The electrical signal from the photodiodes is tapped by an RF probe, combined for balanced detection, subsequently amplified, recorded by an analog-to-digital converter, and further processed on a computer. While the OCT*int* system as described in Sect. 5.2.1 has the reference path integrated on-chip and thus allows measuring samples directly in front of the chip edge, the OCT*ext* system as described in Sect. 5.2.2 has an external reference path and allows imaging with a standard OCT scan head, meters away from the chip. Both PIC were fabricated on a silicon-on-insulator (SOI) wafer with a 2 µm thick buried oxide and a 220 nm thick device layer using 248 nm lithography in the framework of a standard multi-project-wafer (MPW) run. For fabrication, the *OpSIS* service was made use of through *IME A*STAR* in Singapore, using design elements from the *OpSIS OI25A* PDK [38].

5.2.1 OCT chip with internal integrated reference path (OCT*int* system)

The experimental setup and the silicon photonic integrated circuit (PIC) of the OCT*int* system are shown in Figure 5.1 (a). The reference path (RP) of the

OCT interferometer is integrated on the chip. The length of the reference path is designed such that the reference position z_r of the depth scan coincides with the output facet of the PIC, i.e., sample and reference light interfering at the power combiner CPL2 have traveled the same distance through integrated on-chip transport waveguides.

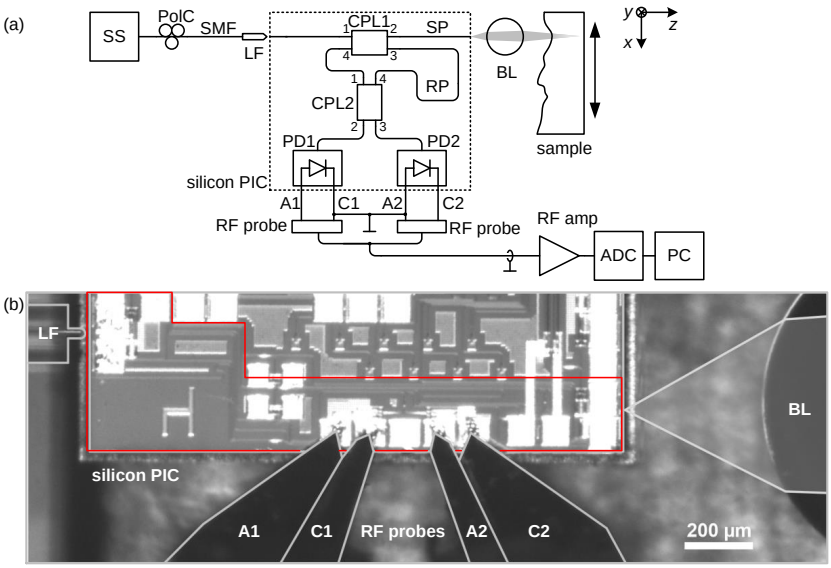

Figure 5.1: OCT*int* system configuration with integrated reference path: Experimental setup and photonic integrated circuit (PIC). (a) Schematic of setup. SS: swept-source laser, PolC: polarization controller, LF: lensed fiber, CPL1,2: 3 dB couplers with ports designated by 1…4, BL: ball lens, SP: sample path, RP: reference path, PD1,2: photodiodes with anodes (A1,2) and cathodes (C1,2), RF amp: RF amplifier, ADC: analog-to-digital converter, PC: personal computer. The photodiodes are contacted with RF probes and their photocurrents are subtracted for balanced detection. (b) PIC microscope image with optical input (LF), optical port with free-space path (via BL) to and from the sample, along with electrical connections (via RF probes). The OCT*int* system was co-integrated with a large number of additional optical circuits used for other purposes – the occupied on-chip area is indicated by a red frame and amounts to less than 0.4 mm^2.

All transport waveguides are uniform and the associated modes feature identical effective refractive indices which are invariant along the propagation direction. This leads to inherent compensation of dispersion in the on-chip sections of the reference and the sample path. The swept-source laser has +11 dBm (12.6 mW) of output power and is edge-coupled to the PIC by a lensed fiber having a 1.9 µm FWHM-spot size diameter, matched to the spot size of the waveguide tapers. This leads to an attenuation of 5 dB at the input facet and to an on-chip power of approximately +6 dBm (4 mW), averaged over a 100 nm wavelength span from 1270 nm to 1370 nm.

A polarization controller (PolC) aligns the polarization according to the quasi-TE mode of the chip waveguides. In the sample path, a silica ball lens (BL) with a diameter of 1 mm is used to focus the radiation emerging from the chip facet and to collect the backscattered light from the sample. Figure 5.1 (b) shows a micrograph of the PIC along with the lensed fiber, the ball lens and the RF probe.

5.2.2 OCT chip with external reference path (OCText system)

The experimental setup and the silicon photonic integrated circuit (PIC) of the OCT*ext* configuration with external reference path are depicted in Figure 5.2 (a). In contrast to the OCT*int* structure in Figure 5.1, the reference path (RP) is routed out of and fed back into the chip. The external reference path with adjustable length allows a long sample path (SP) and the use of a conventional scan head consisting of a fiber-collimator (FC) with angled physical contact connector (APC), a pair of galvo scan mirrors and an OCT scan lens. The reference path comprises a free-space section for precise length adjustments. Polarization controllers (PolC) align the polarization according to the quasi-TE mode of the chip waveguides. Efficient fiber-chip coupling is enabled by a novel kind of microlenses that can be fabricated in-situ by using direct-write three-dimensional laser lithography [125]. Figure 5.2 (b) shows a microscope image of the chip facet with attached polymer lenses. Fiber-chip

coupling loss was estimated by a combination of transmission and photocurrent measurements. The lensed ports on the right-hand side couple to standard single-mode fibers (SMF) with typical losses of 4 dB (6 dB at maximum) over a 100 nm wavelength span from 1270 nm to 1370 nm. The lensed port at the left-hand side has a loss between 7 dB and 10 dB in the same wavelength range, due to an offset error between lens center and chip waveguide. With this coupling scheme and an available laser source power of +11 dBm (12.6 mW), we estimate a wavelength-averaged on-chip power of +3 dBm (2 mW). The average power incident on the sample was measured to be −5 dBm (0.3 mW), and the average reference path power received by each of the photodiodes is estimated to be −17 dBm (20 µW).

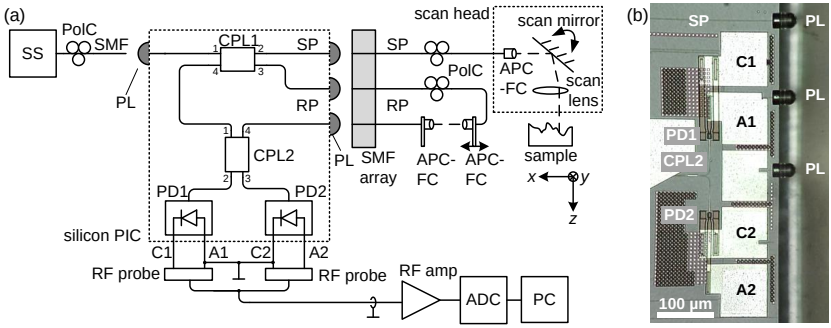

Figure 5.2: OCT*ext* configuration with long external reference and sample paths: Experimental setup and photonic integrated circuit (PIC). (a) Schematic of setup. SS: swept-source laser, PolC: polarization controller, SMF: single-mode fiber, PL: polymer lens, CPL1,2: 3 dB couplers with ports designated by 1…4, SP: sample path, RP: reference path, PD1,2: photodiodes with anodes (A1,2) and cathodes (C1,2), APC-FC: fiber collimator (FC) with angled physical contact connector (APC), RF amp: RF amplifier, ADC: analog-to-digital converter, PC: personal computer. The photodiodes are contacted with RF probes and their photocurrents are subtracted for balanced detection. (b) PIC microscope image of the chip's right edge. The OCT*ext* system is co-integrated with a large number of additional optical circuits used for other purposes – the occupied on-chip area amounts to less than 0.4 mm^2. SP: silicon waveguide for sample path, C1,2 and A1,2: contact pads for photodiode readout with RF probes, PL: Three polymer lenses between chip waveguides and a standard single-mode fiber array.

5.3 Sensitivity and dynamic range

Noise and parasitic backscatter limit both the sensitivity and the dynamic range (DR) of the system. The sensitivity is defined as the minimum measureable sample reflectivity, which is determined by the noise level of the system. The dynamic range, in turn, denotes the maximum achievable signal-to-noise power ratio (SNR) and is smaller than or equal to the sensitivity. In our implementations, noise is dominated by either the relative intensity noise (RIN) of the swept source or by parasitic backscatter – thermal noise of the photodiode RF amplifier is irrelevant in all cases.

Figure 5.3 illustrates the different signal and noise contributions as applicable to the two OCT systems. In general, the relative intensity noise of a laser source relates the variance of the optical power fluctuations to the mean power squared [46]. The relative intensity noise is generally described by its one-sided power spectrum $\mathrm{RIN}(f - f_\mathrm{c})$ centered at the carrier frequency f_c, and can be obtained from a spectral analysis of the photocurrent in the baseband. The spectrum $\mathrm{RIN}(f - f_\mathrm{c})$ is specified in units of Hz^{-1}, or, in logarithmic form, as $\mathrm{dB\,Hz}^{-1}$. The total RIN results from an integration over all frequencies above the carrier frequency,

$$\begin{aligned} \mathrm{RIN}_\mathrm{tot} &= \int_{f_\mathrm{c}}^{\infty} \mathrm{RIN}(f - f_\mathrm{c})\,\mathrm{d}f, \\ \mathrm{RIN}_\mathrm{dB}(f - f_\mathrm{c}) &= 10\lg\big(\mathrm{RIN}(f - f_\mathrm{c}) \times 1\mathrm{Hz}\big) \qquad (\text{in dB Hz}^{-1}). \end{aligned} \tag{5.1}$$

In swept-source OCT, balanced detection is normally used. The photocurrent then only exhibits RIN contributions that result from the interference of the sample field and the reference field, whereas the individual RIN fluctuations of the sample and the reference signal cancel if ideal balancing is assumed [126]. As a consequence, a reflection peak at $z = z_\mathrm{c}$ is surrounded by an accompanying noise profile $\mathrm{RIN}_z(z - z_\mathrm{c})$. Assuming an idealized SS laser for which the optical frequency increases linearly with time, the depth offset $z - z_\mathrm{c}$ from the reflection peak is proportional to a baseband frequency offset, which in these experiments is $f - f_\mathrm{c} = (z - z_\mathrm{c}) \times 3.55$ MHz/mm. This value

was determined by inserting a mirror into the sample path and by measuring the frequency shift of the photocurrent spectrum in MHz as a function of mirror position in mm. Using the relation $\mathrm{RIN}_z(z-z_c) = \mathrm{RIN}(f) \times \mathrm{d}f/\mathrm{d}z$, the spatial relative intensity noise profile is then given by

$$\mathrm{RIN}_z(z-z_c) = \mathrm{RIN}\big((z-z_c) \times 3.55\ \mathrm{MHz/mm}\big) \times 3.55\ \mathrm{MHz/mm}. \qquad (5.2)$$

When expressed in logarithmic form, it is convenient to consider the RIN contribution within a spatial element that corresponds to the depth resolution of $\delta z = 8\ \mu\mathrm{m}$ of the OCT system in vacuum,

$$\mathrm{RIN}_{z,\mathrm{dB}}(z-z_c) = 10\lg\big(\mathrm{RIN}_z(z-z_c) \times 8\mu\mathrm{m}\big) \qquad (\text{in dB}(8\mu\mathrm{m})^{-1}). \quad (5.3)$$

For a linear sweep of the optical frequency, the depth resolution of $\delta z = 8\ \mu\mathrm{m}$ is equivalent to a $\delta z \times 3.55\ \mathrm{MHz/mm} = 28.4\,\mathrm{kHz}$ frequency resolution of the photocurrent spectrum. The position-dependent $\mathrm{RIN}_z(z-z_c)$ of the SS laser can be directly measured using a conventional fiber-based OCT setup, see Figure 5.3 (a). To this end, a fully reflecting (full refl.) mirror is introduced at position $z_c - z_r = 1\,\mathrm{mm}$, leading to a spatial relative intensity noise profile $\mathrm{RIN}_{z,\mathrm{dB}}(z-z_c)$ centered at $z_c - z_r = 1\,\mathrm{mm}$ (thin blue curve). The thick blue curve provides a schematic of these data for a spatial resolution of $\delta z = 8\ \mu\mathrm{m}$. In the immediate neighborhood of this reflection peak at $z_1 - z_c = 0\,\mathrm{mm}$, we measure $\mathrm{RIN}_{z,\mathrm{dB}}(0) = -60\ \mathrm{dB}\,(8\ \mu\mathrm{m})^{-1}$, which is by 60 dB smaller than the reflection peak. Further away from the reflecting mirror, e. g., at $z_9 - z_c = 8\,\mathrm{mm}$, we find $\mathrm{RIN}_{z,\mathrm{dB}}(z_9 - z_c) = -80\ \mathrm{dB}\,(8\ \mu\mathrm{m})^{-1}$, which is smaller than the reflection peak by 80 dB. If the mirror is replaced by a −50 dB reflector, the noise is about 100 dB down (gray curve), dominated by residual RIN due to non-ideal balancing of the photodetectors. The spurious peaks in the gray curve in Figure 5.3 (a) stem from weak reflections in the setup. As a comparison, we measure the one-sided relative intensity noise spectrum $\mathrm{RIN}(f)$ of the Santec swept-laser source with a photodiode and an electrical spectrum analyzer. We find $\mathrm{RIN}_{\mathrm{dB}}(f_a) = -105\ \mathrm{dB\,Hz^{-1}}$ $= -60\ \mathrm{dB}\ (28.4\ \mathrm{kHz})^{-1}$ for $f_a = 3.55\ \mathrm{MHz}$, which corresponds to $\mathrm{RIN}_{z,\mathrm{dB}}(z_a - z_1) = -60\ \mathrm{dB}\ (8\ \mu\mathrm{m})^{-1}$ at a distance of $z_a - z_1 = 1\,\mathrm{mm}$ from the peak of a fully reflecting mirror, in perfect agreement with the results obtained

from the OCT measurement. Similarly, at a larger baseband frequency f_b = 30 MHz, we measure $\mathrm{RIN_{dB}}(f_b) = -125\ \mathrm{dB\,Hz^{-1}} = -80\ \mathrm{dB}\ (28.4\ \mathrm{kHz})^{-1}$, corresponding to $\mathrm{RIN_{z,dB}}(z_b - z_1) = -80\ \mathrm{dB}\ (8\ \mu\mathrm{m})^{-1}$ at a distance of $z_b - z_1 = 8.5\,\mathrm{mm}$ from the peak.

Besides RIN, distributed on-chip backscatter can be a reason for sensitivity limitations of integrated OCT systems. On-chip backscatter is mainly caused by random sidewall roughness or other irregularities of high index-contrast waveguides, which couple forward and backward-propagating fundamental modes to each other [127]. Interference of the backscattered light with the reference light or with light from spurious reflections on the PIC leads to a continuous measurement background. This unwanted interference signal may be suppressed by the common-mode rejection of a balanced detector if both backscattered light and reference light are coupled to the same input port of the combiner CPL2 in front of the balanced detector. Coherent backscatter is hence only visible in case of imperfect common-mode rejection or if backscattered light and reference light are coupled to different input ports of the combiner.

OCT*int* In case of the OCT*int* system, Figure 5.1 and Figure 5.3 (b), the chip edge reflection ($z_{\mathrm{edge,int}} - z_r = 0\,\mathrm{mm}$) amounts to around 3 % (−15 dB) and is by 24 dB larger than the light returned via free-space propagating from a fully reflecting (full refl., return loss 0 dB) plane mirror. This corresponds to single-pass coupling losses between the chip and the free-space beam of approximately 20 dB. Since the depth information in SS-OCT results from a Fourier analysis of the real-valued time-domain data, negative depths cannot be discriminated from the true positive depths (depth degeneracy). Therefore the on-chip backscatter appears also at depths $z - z_r > 0$. In the OCT*int* system, distributed on-chip backscatter (black) dominates over the RIN associated with the strong reflection from the chip edge for small depths $z - z_r < 5$ mm, corresponding to the optical path lengths of the on-chip waveguides. For bigger depths $z - z_r > 5$ mm, the influence of on-chip backscatter can be neglected, and the sensitivity is limited by the RIN background (blue) caused by the chip edge peak. This RIN background is $\mathrm{RIN_{z,\,dB}}(z_8 - z_0) = -80\,\mathrm{dB}\,(8\ \mu\mathrm{m})^{-1}$

below the maximum of the chip edge peak, leading to a sensitivity of −56 dB. The total background consists of the sum of on-chip backscatter and RIN (amber dotted line). Since relative intensity noise originating from the chip edge dominates all noise contributions that could possibly come from other objects (red: full refl.; green: low refl.), the DR is 56 dB.

For the OCT*int* system, sensitivity can be drastically improved by reducing the chip edge reflections using, e.g., angled chip facets [128], or by improving coupling efficiency to and from the chip, using, e.g., polymer microlenses as for the OCT*ext* system. Assuming a reduction of facet reflectivity to below −30 dB and a reduction of the single-pass coupling losses to less than 5 dB, as in the OCT*ext* system, we believe that sensitivity improvements of approximately 45 dB can be achieved.

OCT*ext* The situation is different in the case of the OCT*ext* system, Figure 5.2 and Figure 5.3 (c), where the chip edge peak at $z_{\mathrm{edge,ext}}$ is far outside the source coherence window (long reference path, $z_{\mathrm{edge,ext}} - z_{\mathrm{r}} = -8$ m). The associated $\mathrm{RIN}_{\mathrm{z}}\left(z_1 - z_{\mathrm{edge,ext}}\right)$ in the measurement window near $z_1 - z_{\mathrm{r}} = 1$ mm corresponds to $\mathrm{RIN}(28.4\ \mathrm{GHz})$, which is many orders of magnitude smaller than the RIN levels measured at MHz frequencies as described above. For the OCT*ext* system, RIN from the chip edge reflection can hence be safely neglected as a relevant source of signal impairment. Moreover, on-chip backscatter (black) is less prominent for the OCT*ext* system than for the OCT*int* system. Due to the long fiber-based RP and the limited coherence length of the source, on-chip backscatter does not coherently interfere with the reference light. For a perfectly balanced pair of photodiodes, on-chip backscatter should hence not be visible at all. This is different for the more realistic case of imperfect balancing, where the photocurrent may also contain signal components that result from interference of optical signals that are coupled to the same port of CPL2 of the OCT*ext* system. In this case, spurious reflections at the chip edges or at CPL 1 may act as a parasitic reference signal and generate an interference signal with distributed on-chip backscatter, thus limiting the sensitivity. In our implementation, the parasitic reference signal is dominated by light reflected at the chip edges of both SP and RP.

To obtain an estimate of the signal background associated with on-chip backscatter, we perform an independent measurement to determine the overall on-chip backscatter of the SP and RP waveguides to approximately $\rho_{\mathrm{WG,dB}} = -50$ dB within the depth resolution of 8 µm. To translate this into a signal background in the OCT measurement, we need to estimate the strength of the parasitic reference signal. To his end, the chip edge reflection of each of the SP and RP waveguide ports is assumed to amount to −15 dB (3 %) as in the case of the OCT*int* system, and the on-chip input power is estimated to +3 dBm (2 mW). Taking into account 1 dB of excess loss for each of CPL1 and CPL2, the parasitic reference light coupled to each of the photodiodes thus amounts to −21 dBm (8 µW), which is $\delta_{\mathrm{dB}} = 4$ dB less than the reference light from the off-chip reference path. Moreover, the parasitic reference light and the on-chip backscatter are coupled through the same port 1 to CPL2, and their interference signal is therefore attenuated by the common-mode rejection ratio (CMRR) of the balanced receiver, which amounts to $\zeta_{\mathrm{dB}} = 15$ dB. Taking into account the insertion loss of the lensed ports towards the sample, $a_{\mathrm{dB}} = 4$ dB, and referring the backscatter to an ideal mirror in the off-chip sample path, the backscatter floor in the OCT measurement can be estimated to be $\rho_{\mathrm{BG,dB}} = \rho_{\mathrm{WG,dB}} + 2a_{\mathrm{dB}} - \delta_{\mathrm{dB}} - \zeta_{\mathrm{dB}} = -61$ dB. This backscatter floor limits the sensitivity to – 61 dB and is the relevant limitation for low sample reflectivities (green: low refl.). For strong reflectivities, the total background consists of the sum of on-chip backscatter and RIN (amber dotted line) associated with the reflection peak. For a fully reflecting mirror (red: full refl.) the associated $\mathrm{RIN}_{\mathrm{z,\,dB}}(z_1 - z_{\mathrm{r}}) = -60\,\mathrm{dB}\,(8\ \mu\mathrm{m})^{-1}$ determines the DR of 60 dB.

For the OCT*ext* system, the sensitivity limitations can be mitigated in various ways: On-chip backscatter can be reduced by optimizing the fabrication processes of the waveguides – our current experiments were based on a standard silicon photonic MPW process for optical communications, where backscatter has not been considered a crucial aspect that requires special attention. Moreover, the chip edge reflections can be reduced to values well below −30 dB, by using, e.g., angled waveguide facets [128], which would lead to lower parasitic reference signals. Additionally, improved balancing of the coupler (CPL2) in front of the balanced detectors leads to an increased CMRR and thus further

improves the sensitivity of the OCT*ext* system. Using more advanced power combiners with tunable splitting ratio, e.g., based on Mach-Zehnder interferometers and phase shifters, we believe that CMRR values of significantly better than 30 dB can be achieved, leading to overall sensitivity improvements of more than 30 dB.

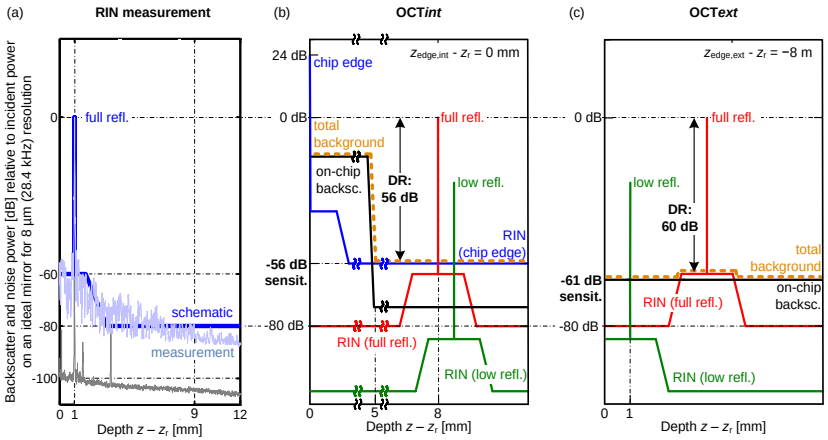

Figure 5.3: Sensitivity and dynamic range (DR) derived from a measured OCT scan in a conventional setup, and from A-scan schematics for configurations OCT*int* and OCT*ext*. Horizontal axes: Measurement depth $z - z_r$ referred to a reference position z_r. Vertical axes: Backscatter signal and noise power relative to the power reflected from an ideal mirror at position z_M. All relative intensity noise data are related to the OCT resolution bandwidth of 28.4 kHz, or, equivalently, to the OCT depth resolution of 8 µm. (a) Measurement of RIN background of the swept source used for the OCT*int* and OCT*ext* system: The profile of the $RIN_{z,dB}$ background is derived from the measured backscatter signal of a fully reflecting mirror (full refl.) positioned at $z_1 - z_r = 1$ mm in a conventional fiber-based OCT setup (thin blue curve: measurement, thick blue curve: schematic approximation). The spatial $RIN_{z,dB}(z - z_c)$ profile for a resolution of 8 µm is about 80 dB down and results from the interference of reflected source RIN with the reference field. If the fully reflecting mirror is replaced by a partially reflecting mirror (power reflection factor –50 dB), the noise level corresponds to a reflectivity of –100 dB (gray curve, spurious peaks originate from weak multiple reflections in the setup), because the balanced receiver suppresses the source RIN, which is transmitted now mainly along the reference path. (b) Noise and backscatter background for the OCT*int* setup. At small distances $z - z_r < 5$ mm, on-chip backscatter (on-chip backsc., black) is dominant. At larger distances $z - z_r > 5$ mm, RIN

from the strong reflection at the chip edge (blue, $z_{\mathrm{edge,\,int}} = z_{\mathrm{r}}$) dominates the noise level for any sample reflectivity. The total background consists of the sum of on-chip backscatter and RIN (amber dotted line). Both a fully reflecting mirror (full refl., red) and a partially reflecting mirror (low refl., green) lead to similarly shaped, but shifted RIN contributions which are smaller than the RIN related to the chip edge reflection peak. The minimum detectable reflectivity (sensitivity) is −56 dB and represents also the DR of the system. (c) Noise and backscatter background for the OCT*ext* setup with schematic backscatter curves. The chip edge peak at $z_{\mathrm{edge,\,ext}} - z_{\mathrm{r}}$ is far outside the source coherence window (long reference path, $z_{\mathrm{edge,\,ext}} - z_{\mathrm{r}} = -8$ m). However, on-chip backscatter (on-chip backsc., black) falls within the coherence window and limits the sensitivity to −61 dB. RIN from a fully reflecting mirror (full refl., red) is responsible for the noise floor 60 dB below the peak. The DR is therefore 60 dB. The total background consists of the sum of on-chip backscatter and RIN (amber dotted line). A weaker mirror reflectivity (low refl., green) can be measured as long as it is larger than −61 dB.

5.4 Performance evaluation and application demonstration

The performance of the integrated OCT systems was assessed by measuring sensitivity, dynamic range and depth scanning range with a plane mirror as a test object placed at various depth positions $z - z_{\mathrm{r}}$. In addition, two- and three-dimensional OCT images of technical and biological samples are taken.

5.4.1 OCT chip with internal integrated reference path (OCT*int* system)

The OCT*int* system is investigated by using a movable plane mirror as a sample. For calibrating the backscatter measurements, a fully reflecting sample mirror is placed at a position $z - z_{\mathrm{r}} = 8$ mm away from the chip edge $z_{\mathrm{edge,int}} - z_{\mathrm{r}} = 0$. Figure 5.4 (a) depicts measured depth scans. For various mirror positions between 5 mm and 12 mm (brightly colored scans) the scans are superimposed, each curve resulting from averaging 100 scans. Because the depth information results from a Fourier analysis of the scan traces in the frequency domain, negative depths $z - z_{\mathrm{r}} < 0$ located inside the chip cannot be discriminated from the true positive depths outside the chip (depth degeneracy). Therefore the on-chip backscatter (black part of the scan) appears also in

space-inverted form at depths $z - z_r > 0$ (gray part of scan), and the backscatter from the mirrors could be also seen at $z - z_r < 0$ (lightly colored scans). Note that the depth axis was derived assuming light propagation in vacuum, such that internal backscatter appears over a 5 mm long depth range even though the scattering on-chip waveguides are approximately 1.4 mm long. The measurement range is hence limited to $z - z_r > 5\,\mathrm{mm}$. Because the edge reflection cannot be removed, the associated fluctuations due to relative intensity noise determine the noise floor in the measurement window and therefore the sensitivity, as has been explained in Sect. 5.3 and Figure 5.3 (b). For mirror positions between 5 mm and 10 mm, the noise level is measured to be between 50 dB and 53 dB below the mirror reflection leading to a dynamic range of up to 53 dB. The minimum measureable sample reflectivity would be −53 dB and defines the measurement sensitivity. This is in good agreement with the 56 dB DR and the −56 dB sensitivity estimated for the OCT*int* system in Section 5.3. The spatial variation of the measured peak reflectivities is attributed to the finite coherence length of the swept source and the finite Rayleigh range of the focused Gaussian beam after the ball lens. The spatial autocorrelation function of the swept-source laser in vacuum is shown as a black broken line in Figure 5.4 (a). A 10 dB coherence length of $l_c = 2 \times 6\ \mathrm{mm}$ can be inferred. The drop in measured reflectivities for positions outside the focus is described by a defocusing function, black dotted line in Figure 5.4 (a). If the ball lens focus is positioned properly, here at 10 mm from the chip facet, the resulting defocusing function partially compensates the signal drop caused by the limited coherence length.

The axial 3 dB-resolution was measured to be 11 µm, which is slightly worse than the 7 µm estimated from the wavelength scanning range of the source. Since dispersion is inherently compensated by equal lengths of on-chip waveguide sections, the reduced resolution is attributed to an imperfect knowledge of the frequency-time relation of the swept-frequency source. In general, the frequency of the tunable laser does not increase linearly with time during the rising slope of a frequency sweep. This can be compensated by digital signal processing if the nonlinearity of the frequency sweep is known exactly. To this end, the time-dependent increase of frequency must be extracted from a

calibration measurement using a mirror as sample reflector [129]. Ideally, for a system with no dispersion imbalance between the sample and the reference path, this time-frequency mapping should lead to an axial resolution that is only limited by the tuning range of the swept source. In practice, however, residual errors of the measured time-dependent increase of frequency lead to a depth-dependent broadening of the reflection peaks in *z*-space.

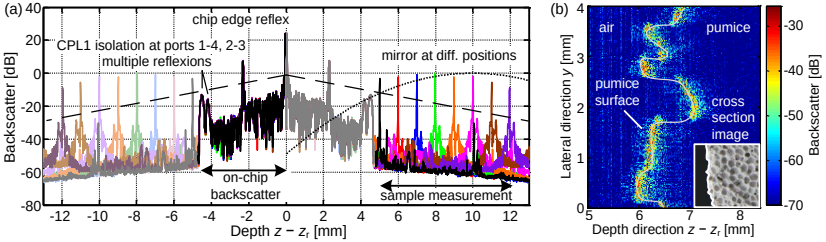

Figure 5.4: Backscatter measurements on the OCT*int* chip with integrated reference path. (a) Reflections from a plane mirror at 8 (positive) depth positions $z - z_r$. A depth $z - z_r = 0$ corresponds to the chip edge. The black broken line is the spatial autocorrelation function of the light source with a 10 dB coherence length of $l_c = 2{\times}6$ mm in vacuum. The beam is focused by a ball lens (BL) at $z - z_r = 10$ mm. The defocusing function (black dotted line) describes the depth-dependent variations of the power reflected from a plane mirror and coupled back into the on-chip waveguide. The drop in spatial coherence (black broken line) partially compensates the defocusing function. The 8 axial A-scans of the mirror backreflections are superimposed (brightly colored scans, normalized to the maximum of the 8 backreflections). The finite isolation of ports 1-4 and 2-3 of coupler CPL1, multiple reflections, and irregularities inside the chip lead to backscatter at negative depths ($z - z_r < 0$, black part of scan). Because the depth information results from a Fourier analysis of the scan traces in the *k*-domain, negative depths cannot be discriminated from the true positive depths (depth degeneracy). Therefore the on-chip backscatter appears also at depths $z - z_r > 0$ (gray part of scan), and the backscatter from the mirrors could be also seen at $z - z_r < 0$ (lightly colored scans). The backscatter in combination with the depth degeneracy limits the measurement range to $z - z_r > 5$ mm. The measured mirror reflections are uniform with variations of less than 3 dB for mirror positions between 5 mm and 10 mm. The noise is measured to be between 50 dB and 53 dB below the mirror reflection leading to a dynamic range of up to 53 dB. A minimum measureable sample reflectivity of −53 dB defines the measurement sensitivity. (b) Two-dimensional B-scan of a piece of pumice. The gray line emphasizes the sample surface. The porous surface structure is clearly visible on both the B-scan and the photograph of the cross-section (inset).

The imaging capability of the OCT*int* system is tested by two-dimensional measurements of a piece of pumice, Figure 5.4 (b). Strong scattering prevents measurable reflections from deeper ranges inside the material, but the porous surface structure is clearly visible (see the photograph in the inset).

5.4.2 OCT chip with external reference path (OCT*ext* system)

The OCT*ext* system is also investigated by using a movable plane mirror as a sample. For calibrating the backscatter measurements a sample mirror with a 1 % reflection factor (20 dB return loss) is placed at a position $z - z_r = 1$ mm within the measurement window 1 mm ≤ $z - z_r$ ≤ 10 mm. The chip edge is located at $z_{edge,\,ext} - z_r = -8$ m and hence does not influence the measurements. Figure 5.5 (a) shows the superposition of single depth-scans (A-scans) for a single −20 dB sample reflector placed at 1 mm increments within the measurement window. The sample reflector comprises a plane mirror and a neutral density filter with 10 dB single-pass attenuation. Each curve results from averaging 100 scans. The noise level, which defines the sensitivity of the system with respect to a 0 dB reference return loss, is measured to be −64 dB. This is in fair agreement with the sensitivity of – 61 dB estimated in Sect. 5.3 based on an analysis of effects of spurious on-chip backscatter.

The imaging depth of the OCT*ext* system is mainly limited by three effects: The limited coherence length of the source (black broken line), the defocusing of the measurement beam which leads to a drop of power coupled back into the fiber for positions outside the focus (defocusing function, black dotted line), and by residual errors of the time-frequency mapping of the swept source. These residual errors lead to a depth-dependent broadening and a decrease of the maxima of the reflection peaks in *z*-space. The total decay caused by limited coherence, defocusing and imperfect time-frequency mapping amounts to approximately 3.3 dB / mm, see Figure 5.5 (a).

The depth resolution of the system is 30 µm, which is significantly worse than the 7 µm expected from the tuning range of the swept source, also when taking into account the effects of imperfect time-frequency mapping. The rather

bad axial resolution is caused by unbalanced dispersion in the sample and reference path. This originates from the fact that the sample and the reference path are composed of different fiber lengths and different path lengths of the on-chip SOI waveguides. Dispersion-induced resolution limitations can be overcome by carefully designing the dispersion maps of the two paths.

Using a perfect reflector, the measured dynamic range is 60 dB at $z - z_r = 1$ mm (not shown) and is limited by the laser RIN. This DR agrees very well with the DR of 60 dB estimated in Sect. 5.3, see also Figure 5.5 (c). The dynamic range is not limited by the RIN originating from the reflection at the chip edge, which is located at $z_{edge,\,ext} - z_r = -8$ m far outside the measurement range. The corresponding $\mathrm{RIN}(28.4\,\mathrm{GHz})$ is not measureable.

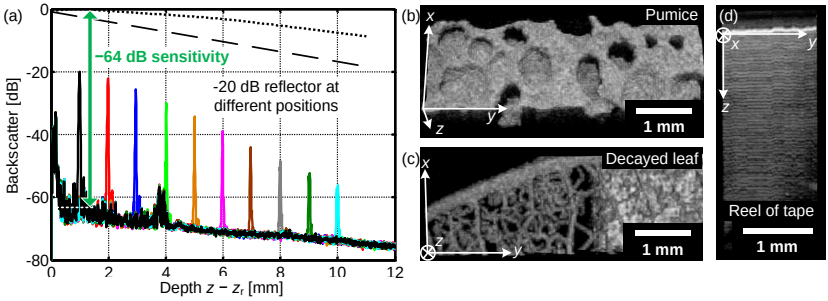

Figure 5.5: Backscatter measurements obtained with the OCT*ext* chip using an external reference path. A depth $z - z_r = 0$ denotes an approximate geometrical position 8 m off the chip edge. (a) Axial scans of a −20 dB reflector as test sample placed at various depth positions $z - z_r$, showing a signal decay of 3.3 dB / mm. The black broken line is the spatial autocorrelation function of the light source with a 10 dB coherence length of $l_c = 2\times6$ mm in vacuum. The position 1 mm coincides with the focus of the scan lens. The black dotted line represents the influence of defocusing on the reflected power coupled back into the on-chip waveguides. The sample is placed at distances from 1 mm to 10 mm within the scanning range, and the resulting scans are superimposed. For each curve, 100 subsequent scans are averaged. The measurement sensitivity is −64 dB for objects placed in a region $0.5\ \mathrm{mm} \le z - z_r \le 2$ mm. (b,c,d) Three-dimensional C-scans of biological and non-biological objects. The images are averages of 100 scans. (b) shows a piece of pumice, (c) a part of a decayed leaf of cornus sanguinea, and (d) a cross section of a reel of tape.

The applicability of the system to sample imaging is demonstrated with 3D volume scans of biological and non-biological samples. Figure 5.5 shows three-dimensional scans (C-Scans) of a piece of pumice (b), a part of a decayed leaf of cornus sanguinea (c), and a reel of adhesive tape (d).

5.5 Summary and outlook

We demonstrate silicon photonic swept-source OCT systems with integrated photodetectors. We design, implement and characterize two different OCT configurations with on-chip internal reference path (OCT*int*) and with external reference path (OCT*ext*). We demonstrate the viability of the systems by imaging both technical and biological samples: Configuration OCT*int* enables imaging directly in front of the chip facet. For this system, we measure sensitivities between −50 dB and −53 dB over 5 mm axial scanning range. As a demonstration, we show a cross-sectional B-scan of a scattering pumice sample. Configuration OCT*ext* supports the use of a remote standard OCT scan head. For this system, a sensitivity of −64 dB was achieved – the best value reported so far for a fully integrated optical OCT processing unit. The OCT*ext* system achieves a better sensitivity than the OCT*int* system, although a larger number of fiber-chip interfaces add to the coupling loss. However, our directly written [125] optimized polymer microlenses minimize this loss. For the OCT*int* setup, aberrations caused by the use of a standard ball lens lead to suboptimal coupling. The limiting factors for both systems are coupling losses and on-chip backscatter. The OCT*int* exhibits a measured dynamic range of 53 dB, limited by the RIN contribution from the strong chip edge reflection. The dynamic range of the OCT*ext* is 60 dB, limited by the RIN contribution from a fully reflecting object.

We believe that our miniaturized OCT systems are suitable for a wide range of both medical and technical applications, including also advanced schemes such as Doppler OCT [130], optical coherence elastography (OCE) [131], or photo-thermal OCT [132]. By combining silicon photonic OCT engines with chip-scale swept-source lasers [133], fully integrated OCT systems come

within reach. We report on a first proof-of-concept demonstration, with vast potential for improving the performance: Polymer microlenses, as used in OCT*ext*, could be used for the OCT*int* system as well, enhancing power coupling and reducing chip-edge reflections. Thus, a higher dynamic range and an improved sensitivity could be achieved with this system. For OCT*ext*, the effects of on-chip backscatter can be significantly improved by optimized fabrication processes and device design. In both cases, sensitivities better than −90 dB can be achieved based on technological and design improvements. Moreover, we believe that compact and highly integrated OCT systems with tens or even hundreds of parallel spatial sensors will open completely new application spaces and create attractive market opportunities.

[End of Publication P1]

6 Summary and Outlook

In the course of this work, OCT systems have been developed, both fibre-based implementations and photonic integrated circuits on a silicon chip. The fibre-based system has been designed for either single-polarization or polarization-sensitive operation, as well as for in-line dispersion-state monitoring of nanocomposites during compounding. In addition to system setup, a light scattering model for nanomaterial analysis has been developed. Combined with Mie's scattering theory accurate particle size determination has been demonstrated. An extension of the model towards different polarizations enabled the precise characterization of gold nanorods with respect to their diameter and aspect ratio. The micro and nanostructure of composite materials has been characterized in a probing volume of several cubic millimeters, using image processing techniques on OCT measured data for larger features, and by applying scattering model analysis, which allowed to obtain nanoscale information on the sample structure. Besides material analysis, photonic integration of OCT systems during this work has led to silicon photonic OCT circuits, comprising interferometer and balanced detector on chip. These systems allowed imaging of biological and technical samples. In the following, the key achievements of this work are summarized and an outlook to possible future activities is given.

For nanomaterial analysis with OCT, a **polarization-resolved light scattering model** has been developed. The model is adequate for weakly scattering samples and links the scattering properties of the single particles to the backscattering signal obtained in the OCT measurement. This allows the analysis of scatterers beyond the resolution limit of OCT [P2, P3, P5]. At higher sample depths or for strongly scattering samples, multiple-scattered light adds to the measurement signal. Future work might address this effect by models that account for multiple scattering.

A **polarization-sensitive optical coherence tomography system** has been developed using standard single-mode fibres, free-space polarization optics,

and a polarization-sensitive receiver. For experiments during nanocomposite production, a dedicated OCT probe for measurements at a compounding extruder with rugged titanium shaft, adjustable optics and temperature and scratch-resistant sapphire window has been developed and applied to production process monitoring [P2].

Dispersion-state analysis of nanocomposites has been one main application of the light scattering model. The dispersion state, which is crucial to the functionality of nanocomposites, has been characterized based on both, image processing of OCT depth-scans and model-based evaluation of the backscatter signals. Image analysis has been applied to particle agglomerates which are bigger than the resolution of the system. For a quantitative evaluation, the image data has been segmented and two independent parameters have been extracted: Area fraction and perimeter-to-area ratio, both of which show strong correlation with the dispersion effort in sample production [P2]. The scattering model analysis has been applied successfully to CNT-epoxy samples prepared in three-roll mills and even outperformed conventional light microscopic analysis methods [P2, P6]. In addition, the extracted parameters were strongly correlated with trends observed for electrical permittivity of the sample. Further macroscopic material parameters, like chemical barrier properties, tensile strength or electrical conductivity are possible design goals of nanocomposite manufacturers. The direct correlation of the OCT analysis to these parameters could significantly advance material development.

In addition to sample characterization in a laboratory environment, a dedicated extruder probe was developed and demonstrated for **OCT-based in-line characterization** in a fabrication environment. The OCT sample head with extruder probe was mounted on a compounding extruder at a pilot plant at the Fraunhofer Institute for Chemical Technology (ICT). During nanocomposite processing, the dispersion state has been monitored in real time, revealing good correlation with the processing parameters [P2]. This technique is not limited to compounding extruders but can be applied to a range of composite material production methods.

Apart from nanocomposites, the **analysis of single dispersed nanoparticles of different sizes and shapes** has been conducted in this work. Making use of the size-dependent scattering of nano and micro particles, dispersed polystyrene nanospheres of different diameter and concentration have been characterized using OCT [P2, P3, P5]. By fitting the calibrated single scattering model to the measurements based on Mie's scattering theory, the particle diameters have been determined with an accuracy of below 4 % [P2]. In addition, aspect ratio and diameter of dispersed gold nanorods have been estimated. For this purpose, polarization-sensitive OCT measurements have been fitted to numerical scattering calculations. The rod diameters have been determined with 25 % deviation and the aspect ratio matches the nominal value by at maximum 10 % deviation. The application of this technique to monitor fabrication processes of particles with critical demands on shape or size could lead to greatly reduced development cycles of nanoparticles for technical or medical applications.

In addition to fibre-optic OCT systems and material analysis with OCT, the **integration of OCT on a silicon photonic chip** has been demonstrated in this work. In the framework of a multi-project-wafer run [38], silicon photonic integrated OCT systems have been fabricated at A*STAR IME in Singapore. Our demonstrations represent the first fully integrated swept-source OCT on silicon, including an interferometer and a balanced photodetector. Two different configurations have been fabricated, one with external reference arm for long-distance imaging, and one with internally integrated reference arm allowing sample measurements at the chip edge. The systems offer up to −64 dB sensitivity and enable imaging of biological and technical samples [P1, P4, P7-10]. The sensitivity is still below those of fibre-based systems, however, improvements in coupling losses and reflections offer the perspective to enhance the sensitivity to at least −90 dB. The on-chip integration brings substantial advantages in robustness, cost per unit, and footprint and is hence an essential step towards low-cost sensors for industrial applications. Highly integrated OCT systems with many parallel channels could even obviate lateral mechanical beam scanning, and thus represent a further step towards powerful OCT characterization of large sample volumes.

Appendix

A. Mathematical and physical definitions

A.1 Fourier transform

This section serves as reference for the Fourier transforms used within this work and derives important correspondences. All definitions refer to Kiencke and Jäkel [134]. The Fourier transform $\mathcal{F}\{\cdot\}$ of a signal $y(t)$ in the time domain to a signal $\breve{y}(f)$ in frequency domain has been favoured over the often seen transformation to angular frequency ω, as it gets along without additional asymmetric pre-factors.

Note that temporal and spatial Fourier transforms and their inverse transforms assume a time dependency of the form $\exp(\mathrm{j}\omega t)$, as it is common in electrical engineering. In physics, the symbol $\mathrm{i}=\sqrt{-1}$ is often used for the imaginary unit, and a time dependence of the form $\exp(-\mathrm{i}\omega t)$ is assumed. Both notations describe the same physical situation. The formulations are complex conjugate to each other.

The Fourier transform and the inverse Fourier transform are defined as

$$\begin{aligned} \breve{y}(f) &= \mathcal{F}\{y(t)\} = \int_{-\infty}^{+\infty} y(t)\,\mathrm{e}^{-\mathrm{j}2\pi ft}\mathrm{d}t, \\ y(t) &= \mathcal{F}^{-1}\{\breve{y}(f)\} = \int_{-\infty}^{+\infty} \breve{y}(f)\,\mathrm{e}^{\mathrm{j}2\pi ft}\mathrm{d}f. \end{aligned} \tag{A.1}$$

The concatenation of inverse and forward Fourier transforms leads to the original signal, shown here for the spectrum

$$\breve{y}(f) = \int_{-\infty}^{+\infty} y(t)\, \mathrm{e}^{-\mathrm{j}2\pi ft}\mathrm{d}t = \int_{-\infty}^{+\infty}\int_{-\infty}^{+\infty} \breve{y}(f')\, \mathrm{e}^{\mathrm{j}2\pi f't}\mathrm{d}f'\, \mathrm{e}^{-\mathrm{j}2\pi ft}\mathrm{d}t$$

$$= \int_{-\infty}^{+\infty} \breve{y}(f') \underbrace{\int_{-\infty}^{+\infty} \mathrm{e}^{-\mathrm{j}2\pi(f-f')t}\mathrm{d}t}_{\delta(f-f')}\, \mathrm{d}f' = \int_{-\infty}^{+\infty} \breve{y}(f')\delta(f-f')\mathrm{d}f' \quad \text{(A.2)}$$

$$= \breve{y}(f) \ .$$

A multiplication in time domain corresponds to a convolution in frequency domain

$$\mathcal{F}\{y_1(t)y_2(t)\} = \breve{y}_1(f) * \breve{y}_2(f) = \int_{-\infty}^{+\infty} \breve{y}_1(f')\breve{y}_2(f-f')\,\mathrm{d}f' \ . \quad \text{(A.3)}$$

Time shift is linked to linearly increasing phase of the spectrum

$$\mathcal{F}\{y(t-t_0)\} = \mathrm{e}^{-\mathrm{j}2\pi ft_0}\ \breve{y}(f)\ , \quad \text{(A.4)}$$

and a linear phase increase in the time domain corresponds to a spectral shift in the frequency domain,

$$\mathcal{F}\left\{\mathrm{e}^{\mathrm{j}2\pi f_0 t}\ y(t)\right\} = \breve{y}(f-f_0)\,. \quad \text{(A.5)}$$

The cosine-function corresponds to a pair of delta-functions

$$\mathcal{F}\{\cos(2\pi f_0 t)\} = \frac{1}{2}\big(\delta(f+f_0) + \delta(f-f_0)\big)\ . \quad \text{(A.6)}$$

A rectangular window function

$$\mathrm{rect}_{\Delta t}(t) = \begin{cases} 1 & , \ |t| < \dfrac{\Delta t}{2} \\ 0 & , \ |t| > \dfrac{\Delta t}{2} \end{cases} \quad \text{(A.7)}$$

corresponds to a sinc function

$$\mathcal{F}\{\mathrm{rect}_{\Delta t}(t)\} = \Delta t \frac{\sin(f\Delta t)}{f\Delta t} = \Delta t\ \mathrm{sinc}(f\Delta t)\,. \quad \text{(A.8)}$$

A Hann window that weights a rectangular function with a raised cosine function of one period

$$y_{\mathrm{Hn},\Delta t}(t) = \frac{1}{2}\mathrm{rect}_{\Delta t}(t)\left(1+\cos\left(\frac{2\pi}{\Delta t}t\right)\right) \tag{A.9}$$

corresponds to three overlapping π-shifted sinc-spectra, which partially suppress the side-lobes of each other [135,136]

$$\mathcal{F}\left\{y_{\mathrm{Hn},\Delta t}(t)\right\} = \frac{\Delta t}{2}\left[\mathrm{sinc}(\pi f \Delta t) + \frac{1}{2}\mathrm{sinc}(\pi f \Delta t + \pi) + \frac{1}{2}\mathrm{sinc}(\pi f \Delta t - \pi)\right]. \tag{A.10}$$

A Gaussian pulse of $1/\mathrm{e}$-width of $1/\sqrt{a}$ in the time domain transforms into a Gaussian spectrum of $1/\mathrm{e}$-width of $\sqrt{a}/\pi$

$$\mathcal{F}\left\{\mathrm{e}^{-at^2}\right\} = \sqrt{\frac{\pi}{a}}\,\mathrm{e}^{-\frac{(\pi f)^2}{a}}. \tag{A.11}$$

A.2 Discrete Fourier transform

In the discrete Fourier transform (DFT), signals in both domains, here referred to as time and frequency domain, are discretized and limited in number of elements. The discretization in time domain leads to a periodic spectrum, and the limited number of observation points in time domain leads to discrete sampling points in the frequency domain [134]. The total observation time

$$\Delta t_{\mathrm{d}} = M\,\delta t_{\mathrm{d}} \tag{A.12}$$

is split into M equal sampling time steps δt_{d}. The sampling frequency

$$f_{\mathrm{d}} = \frac{1}{\delta t_{\mathrm{d}}} = 2\Delta f_{\mathrm{d}} \tag{A.13}$$

is the reciprocal of the sampling time δt_{d} and is twice the observable bandwidth Δf_{d}. The frequency resolution is obtained by dividing the sampling

frequency f_d into M intervals, resulting in the reciprocal of the total observation time,

$$\delta f_\mathrm{d} = \frac{f_\mathrm{d}}{M} = \frac{1}{\delta t_\mathrm{d} M} = \frac{1}{\Delta t_\mathrm{d}} \ . \tag{A.14}$$

With counting variables m and i for points in time and frequency domain, respectively, the DFT and the inverse DFT are defined as

$$\begin{aligned} \breve{y}_i &= \sum_{m=0}^{M-1} y_m \mathrm{e}^{-\mathrm{j}\,2\pi i m/M} \ , \\ y_m &= \frac{1}{M} \sum_{i=0}^{M-1} \breve{y}_i \ \mathrm{e}^{\mathrm{j}\,2\pi i m/M} \ . \end{aligned} \tag{A.15}$$

In this relation, y_m are the elements of the data vector in time domain and $\breve{y}_i$ the elements in frequency domain.

A.3 Convolution and correlation

The convolution of two signals is given by

$$y_1(t) * y_2(t) = \int_{-\infty}^{+\infty} y_1(\tau) y_2(t-\tau) \mathrm{d}\tau \ . \tag{A.16}$$

In this thesis random processes are assumed to be ergodic, see A.6. The temporal correlation [44] of two signals is then defined as

$$\vartheta_{y_1 y_2}(\tau) = \int_{-\infty}^{+\infty} y_1^*(t) y_2(t+\tau) \mathrm{d}t \ . \tag{A.17}$$

A.4 Delta distribution

The delta distribution [137], or Dirac delta function $\delta(x)$, is defined by its measure with a test function $\Phi(x)$

$$\langle \delta, \Phi \rangle = \int_{-\infty}^{+\infty} \delta(x)\Phi(x)\mathrm{d}x = \Phi(0), \tag{A.18}$$

yielding the value of the test function at the position $x = 0$. The test function $\Phi(x)$ needs to be continuous and indefinitely often continuously differentiable. The function $\Phi(x)$ either needs to be zero outside a limited region, or the function and all its derivatives need to approach zero for $|x| \to \infty$, faster than any power $|x|^{-n}$ approaches zero. The second case includes the Gauss-function e^{-x^2}. The delta distribution can be described as follows,

$$\begin{aligned} &\delta(x) = 0, \quad \text{in} -\infty < x < 0 \text{ and } 0 < x < +\infty, \\ &\int_{-\infty}^{+\infty} \delta(x)\mathrm{d}x = 1\,. \end{aligned} \tag{A.19}$$

The integral of a delayed delta function with a test function results in the test function at the value of the delay,

$$\int_{-\infty}^{+\infty} \delta(x - x_a)\Phi(x)\mathrm{d}x = \int_{-\infty}^{+\infty} \delta(x_a - x)\Phi(x)\mathrm{d}x = \Phi(x_a)\,. \tag{A.20}$$

A.5 Gaussian beams

A Gaussian beam is a solution of the paraxial Helmholtz equation and combines wave- and ray-optical elements [138]. It is characterized by a beam waist with radius w_0 at position z_f and a Gaussian-shaped decay of the complex field amplitude $\underline{A}_\mathrm{G}(r,z)$ with increasing radial distance. Here, we assume linear polarization and $\underline{A}_\mathrm{G}(r,z)$ denotes the complex amplitude of the dominant transversal field component. Its radial and axial dependence is described by

$$\underline{A}_\mathrm{G}(r,z) = A_{\mathrm{G},0}\frac{w_0}{w(z)}\,\mathrm{e}^{-\left(\frac{r}{w(z)}\right)^2}\,\mathrm{e}^{-\frac{\mathrm{j}kr^2}{2R_\mathrm{G}(z)}}\,\mathrm{e}^{\mathrm{j}(\varphi_\mathrm{G}(z)-k(z-z_\mathrm{f}))}. \tag{A.21}$$

Here, $A_{\mathrm{G},0}$ is the maximum field amplitude,

$$b = \frac{2\pi w_0^2}{\lambda} \tag{A.22}$$

is the confocal parameter,

$$w(z) = w_0 \sqrt{1 + \left(\frac{2(z - z_\mathrm{f})}{b} \right)^2} \tag{A.23}$$

is the beam radius over axial position z,

$$R_\mathrm{G}(z) = (z - z_\mathrm{f}) \left(1 + \left(\frac{b}{2(z - z_\mathrm{f})} \right)^2 \right) \tag{A.24}$$

is the radius of curvature of the phase fronts, and

$$\varphi_\mathrm{G}(z) = \arctan\left(\frac{2(z - z_\mathrm{f})}{b} \right) \tag{A.25}$$

denotes the Gouy phase, which describes a continuous phase shift of the mode from $-\pi/2$ to $+\pi/2$, when passing the focal point.

A.6 Coherence of optical fields

Coherence of optical fields describes the correlation of their field vector components either at different positions in space (spatial coherence) or at different times (temporal coherence), or for different vector components q_1, q_2, with $q_\mathrm{i} = \{x, y, z\}$ [139]. The coherence function of the first order

$$\underline{G}_{q_1, q_2}(t_1, \vec{r}_1; t_2, \vec{r}_2) = \overline{\underline{E}_{q_1}(t_1, \vec{r}_1) \underline{E}^*_{q_2}(t_2, \vec{r}_2)} \tag{A.26}$$

is given by the correlation of two complex electric fields $\underline{E}_{q_1}(t_1, \vec{r}_1)$, $\underline{E}_{q_2}(t_2, \vec{r}_2)$ in directions q_1, q_2, at the points in time t_1, t_2 and at the spatial positions $\vec{r}_1, \vec{r}_2$. The normalized complex coherence function

$$\begin{aligned} &\underline{g}_{q_1, q_2}(t_1, \vec{r}_1; t_2, \vec{r}_2) \\ &= \underline{G}_{q_1, q_2}(t_1, \vec{r}_1; t_2, \vec{r}_2) \Big/ \sqrt{\underline{G}_{q_1, q_1}(t_1, \vec{r}_1; t_1, \vec{r}_1) \underline{G}_{q_2, q_2}(t_2, \vec{r}_2; t_2, \vec{r}_2)} \end{aligned} \tag{A.27}$$

states, if two fields are coherent to the first order, then $\left|\underline{g}_{q_1,\,q_2}\left(t_1,\vec{r}_1;t_2,\vec{r}_2\right)\right|=1$, or if two fields are incoherent to first order, $\left|\underline{g}_{q_1,\,q_2}\left(t_1,\vec{r}_1;t_2,\vec{r}_2\right)\right|=0$. Intermediate values define partially coherent fields.

Up to now, ensemble averages are considered. If averaging over a sufficiently large ensemble of realizations of a random process leads to the same result than averaging one realization of the process over time, the process is called ergodic. Stationarity is a prerequisite for ergodicity, but is not sufficient [134].

In most practical cases, ergodicity can be assumed. Then, not the absolute points in time t_1, t_2, but only the time difference $\tau=t_2-t_1$ is relevant and Eq. (A.26) results in

$$\underline{\Gamma}_{q_1,\,q_2}\left(\tau,\vec{r}_1,\vec{r}_2\right)=\overline{\underline{E}_{q_1}\left(t,\vec{r}_1\right)\underline{E}^{*}_{q_2}\left(t-\tau,\vec{r}_2\right)}, \tag{A.28}$$

which is normalized to

$$\underline{\gamma}_{q_1,\,q_2}\left(\tau,\vec{r}_1,\vec{r}_2\right)=\underline{\Gamma}_{q_1,\,q_2}\left(\tau,\vec{r}_1,\vec{r}_2\right)\Big/\sqrt{\underline{\Gamma}_{q_1,\,q_1}\left(0,\vec{r}_1,\vec{r}_1\right)\underline{\Gamma}_{q_2,\,q_2}\left(0,\vec{r}_2,\vec{r}_2\right)}\,. \tag{A.29}$$

Since the coherence function is represented by a correlation of $\underline{E}_{q_1}\left(t_1,\vec{r}_1\right)$ and $\underline{E}_{q_2}\left(t_2,\vec{r}_2\right)$, the Wiener-Khintchine theorem [26] can be applied to calculate their mutual spectral density $\breve{\underline{\Gamma}}_{q_1,\,q_2}\left(f,\vec{r}_1,\vec{r}_2\right)$ by a Fourier transform of $\underline{\Gamma}_{q_1,\,q_2}\left(\tau,\vec{r}_1,\vec{r}_2\right)$. This results in

$$\breve{\underline{\Gamma}}_{q_1,\,q_2}\left(f,\vec{r}_1,\vec{r}_2\right)=\int_{-\infty}^{+\infty}\underline{\Gamma}_{q_1q_2}\left(\tau,\vec{r}_1,\vec{r}_2\right)\mathrm{e}^{-\mathrm{j}\,2\pi f\tau}\,\mathrm{d}\tau\,. \tag{A.30}$$

Temporal coherence describes the correlation in time at one position in space, thus the normalized coherence function is given by $\underline{\gamma}\left(\tau,\vec{r}_1,\vec{r}_1\right)$. The coherence time τ_c defines the maximum time difference $|\tau|\le\tau_\mathrm{c}$ for which $\left|\underline{\gamma}\left(\tau,\vec{r}_1,\vec{r}_1\right)\right|\approx 1$ holds. In accordance with this, the coherence length $l_\mathrm{c}=c_0\tau_\mathrm{c}$ defines the propagation length in which the field varies sinusoidally with constant phase offset and amplitude and can thus be assumed to be one longitudinal mode [44]. The reciprocal of the coherence time is the spectral width $\delta f=1/\tau_\mathrm{c}$.

When spatial coherence is investigated, the time difference is set to $\tau = 0$, and the spatial coherence function results, $\underline{\gamma}(0, \vec{r}_1, \vec{r}_2)$. The coherence radius $r_c \leq |\vec{r}_1 - \vec{r}_2|$ gives the maximum spatial distance of $\vec{r}_1, \vec{r}_2$ for which $|\underline{\gamma}(0, \vec{r}_1, \vec{r}_2)| \approx 1$. From this, a coherence area $F_c = \pi r_c^2$ can be defined.

B. Bibliography

1. D. Huang, E. A. Swanson, C. P. Lin, J. S. Schuman, W. G. Stinson, W. Chang, M. R. Hee, T. Flotte, K. Gregory, C. A. Puliafito, and J. G. Fujimoto, "Optical coherence tomography," Science **254**, 1178–1181 (1991).
2. M. R. Hee, C. A. Puliafito, C. Wong, E. Reichel, J. S. Duker, J. S. Schuman, E. A. Swanson, and J. G. Fujimoto, "Optical coherence tomography of central serous chorioretinopathy," Am. J. Ophthalmol. **120**, 65–74 (1995).
3. M. Bechmann, M. J. Thiel, A. S. Neubauer, S. Ullrich, K. Ludwig, K. R. Kenyon, and M. W. Ulbig, "Central corneal thickness measurement with a retinal optical coherence tomography device versus standard ultrasonic pachymetry," Cornea **20**, 50–54 (2001).
4. J. Welzel, "Optical coherence tomography in dermatology: a review," Skin Res. Technol. **7**, 1–9 (2001).
5. G. J. Tearney, M. E. Brezinski, B. E. Bouma, S. A. Boppart, C. Pitris, J. F. Southern, and J. G. Fujimoto, "In vivo endoscopic optical biopsy with optical coherence tomography," Science **276**, 2037–2039 (1997).
6. M. E. Brezinski, G. J. Tearney, B. E. Bouma, J. A. Izatt, M. R. Hee, E. A. Swanson, J. F. Southern, and J. G. Fujimoto, "Optical coherence tomography for optical biopsy: properties and demonstration of vascular pathology," Circulation **93**, 1206–1213 (1996).
7. J. J. Esteve-Taboada, A. Domínguez-Vicent, D. Monsálvez-Romín, A. J. Del Águila-Carrasco, and R. Montés-Micó, "Non-invasive measurements of the dynamic changes in the ciliary muscle, crystalline lens morphology, and anterior chamber during accommodation with a high-resolution OCT," Graefe's archive for clinical and experimental ophthalmology = Albrecht von Graefes Archiv fur klinische und experimentelle Ophthalmologie **255**, 1385–1394 (2017).
8. C. S. Langlo, E. J. Patterson, B. P. Higgins, P. Summerfelt, M. M. Razeen, L. R. Erker, M. Parker, F. T. Collison, G. A. Fishman, C. N. Kay, J. Zhang, R. G. Weleber, P. Yang, D. J. Wilson, M. E. Pennesi, B. L. Lam,

J. Chiang, J. D. Chulay, A. Dubra, W. W. Hauswirth, and J. Carroll, "Residual Foveal Cone Structure in CNGB3-Associated Achromatopsia," Investigative ophthalmology & visual science **57**, 3984–3995 (2016).

9. B. D. Chithrani, A. A. Ghazani, and W. C. W. Chan, "Determining the size and shape dependence of gold nanoparticle uptake into mammalian cells," Nano Lett. **6**, 662–668 (2006).
10. S. Schneider, F. Eppler, M. Weber, G. Olowojoba, P. Weiss, C. Hubner, I. Mikonsaari, W. Freude, and C. Koos, "Multiscale dispersion-state characterization of nanocomposites using optical coherence tomography," Scientific reports **6**, 31733 (2016).
11. M. Okamoto, P. H. Nam, P. Maiti, T. Kotaka, N. Hasegawa, and A. Usuki, "A house of cards structure in polypropylene/clay nanocomposites under elongational flow," Nano Lett. **1**, 295–298 (2001).
12. D. L. Carroll, R. Czerw, and S. Webster, "Polymer–nanotube composites for transparent, conducting thin films," Synthetic Met. **155**, 694–697 (2005).
13. Y. Zhang, J. Wang, X. Bai, T. Jiang, Q. Zhang, and S. Wang, "Mesoporous silica nanoparticles for increasing the oral bioavailability and permeation of poorly water soluble drugs," Mol. Pharm. **9**, 505–513 (2012).
14. C. Novo, A. M. Funston, and P. Mulvaney, "Direct observation of chemical reactions on single gold nanocrystals using surface plasmon spectroscopy," Nature nanotechnology **3**, 598–602 (2008).
15. X. Huang, I. H. El-Sayed, W. Qian, and M. A. El-Sayed, "Cancer cell imaging and photothermal therapy in the near-infrared region by using gold nanorods," Journal of the American Chemical Society **128**, 2115–2120 (2006).
16. S. S. Kumar, P. Venkateswarlu, V. R. Rao, and G. N. Rao, "Synthesis, characterization and optical properties of zinc oxide nanoparticles," Int Nano Lett **3**, 30 (2013).
17. J. E. Evans, K. L. Jungjohann, N. D. Browning, and I. Arslan, "Controlled Growth of Nanoparticles from Solution with In Situ Liquid Transmission Electron Microscopy," Nano Lett. **11**, 2809–2813 (2011).
18. A. C. Balazs, T. Emrick, and T. P. Russell, "Nanoparticle polymer composites: where two small worlds meet," Science **314**, 1107–1110 (2006).

19. H. Kwon, M. Leparoux, and A. Kawasaki, “Functionally graded dual-nanoparticulate-reinforced aluminium matrix bulk materials fabricated by spark plasma sintering,” J. Mater. Sci. Technol. **30**, 736–742 (2014).
20. N. Jouault, F. Dalmas, F. Boué, and J. Jestin, “Multiscale characterization of filler dispersion and origins of mechanical reinforcement in model nanocomposites,” Polymer **53**, 761–775 (2012).
21. S. Sathyanarayana, G. Olowojoba, P. Weiss, B. Caglar, B. Pataki, I. Mikonsaari, C. Hübner, and F. Henning, “Compounding of MWCNTs with PS in a twin-screw extruder with varying process parameters: Morphology, interfacial behavior, thermal stability, rheology, and volume resistivity,” Macromol. Mater. Eng. **298**, 89–105 (2013).
22. P. J. Wyatt, “Submicrometer particle sizing by multiangle light scattering following fractionation,” J. Colloid. Interf. Sci. **197**, 9–20 (1998).
23. V. Guschin, W. Becker, N. Eisenreich, and A. Bendfeld, “Determination of the nanoparticle size distribution in media by turbidimetric measurements,” Chem. Eng. Technol. **35**, 317–322 (2012).
24. J. Pencer and F. R. Hallett, “Effects of Vesicle Size and Shape on Static and Dynamic Light Scattering Measurements,” Langmuir **19**, 7488–7497 (2003).
25. W. Anderson, D. Kozak, V. A. Coleman, A. K. Jamting, and M. Trau, “A comparative study of submicron particle sizing platforms: accuracy, precision and resolution analysis of polydisperse particle size distributions,” Journal of Colloid and Interface Science **405**, 322–330 (2013).
26. M. Born and E. Wolf, *Principles of optics. Electromagnetic theory of propagation, interference and diffraction of light. 4.ed* (Pergamon press, 1970).
27. A. F. Fercher, C. K. Hitzenberger, G. Kamp, and S. Y. El-Zaiat, “Measurement of intraocular distances by backscattering spectral interferometry,” Optics Commun. **117**, 43–48 (1995).
28. S. R. Chinn, E. A. Swanson, and J. G. Fujimoto, “Optical coherence tomography using a frequency-tunable optical source,” Opt. Lett. **22**, 340–342 (1997).

29. A. Rollins, S. Yazdanfar, M. Kulkarni, R. Ung-Arunyawee, and J. Izatt, "In vivo video rate optical coherence tomography," Opt. Express **3**, 219 (1998).
30. M. Choma, M. Sarunic, C. Yang, and J. Izatt, "Sensitivity advantage of swept source and Fourier domain optical coherence tomography," Opt. Express **11**, 2183 (2003).
31. de Boer, Johannes F., B. Cense, B. H. Park, M. C. Pierce, G. J. Tearney, and B. E. Bouma, "Improved signal-to-noise ratio in spectral-domain compared with time-domain optical coherence tomography," Opt. Lett. **28**, 2067 (2003).
32. W. Wieser, W. Draxinger, T. Klein, S. Karpf, T. Pfeiffer, and R. Huber, "High definition live 3D-OCT in vivo: design and evaluation of a 4D OCT engine with 1 GVoxel/s," Biomed. Opt. Express **5**, 2963–2977 (2014).
33. T. Klein, W. Wieser, L. Reznicek, A. Neubauer, A. Kampik, and R. Huber, "Multi-MHz retinal OCT," Biomed. Opt. Express **4**, 1890–1908 (2013).
34. W. Wieser, B. R. Biedermann, T. Klein, C. M. Eigenwillig, and R. Huber, "Multi-megahertz OCT: High quality 3D imaging at 20 million A-scans and 4.5 GVoxels per second," Opt. Express **18**, 14685–14704 (2010).
35. M. Hochberg and T. Baehr-Jones, "Towards fabless silicon photonics," Nature Photon. **4**, 492–494 (2010).
36. A. Rahim, J. Goyvaerts, B. Szelag, J.-M. Fedeli, P. Absil, T. Aalto, M. Harjanne, C. Littlejohns, G. Reed, G. Winzer, S. Lischke, L. Zimmermann, D. Knoll, D. Geuzebroek, A. Leinse, M. Geiselmann, M. Zervas, H. Jans, A. Stassen, C. Dominguez, P. Munoz, D. Domenech, A. L. Giesecke, M. C. Lemme, and R. Baets, "Open-Access Silicon Photonics Platforms in Europe," IEEE J. Select. Topics Quantum Electron. **25**, 1–18 (2019).
37. E. Timurdogan, Z. Su, C. V. Poulton, M. J. Byrd, S. Xin, R.-J. Shiue, B. R. Moss, E. S. Hosseini, and M. R. Watts, "AIM Process Design Kit (AIMPDKv2.0): Silicon Photonics Passive and Active Component Li-

braries on a 300mm Wafer," in *Optical Fiber Communication Conference* (OSA), M3F.1.

38. T. Baehr-Jones, R. Ding, A. Ayazi, T. Pinguet, M. Streshinsky, N. Harris, J. Li, L. He, M. Gould, Y. Zhang, A. Eu-Jin Lim, T.-Y. Liow, S. Hwee-Gee Teo, G.-Q. Lo, and M. Hochberg, "A 25 Gb/s silicon photonics platform," ArXiv e-prints, 1203.0767 (2012).
39. Y. Pan, R. Birngruber, J. Rosperich, and R. Engelhardt, "Low-coherence optical tomography in turbid tissue: theoretical analysis," Appl. Opt. **34**, 6564–6574 (1995).
40. W. Freude, S. Schneider, M. Lauermann, P.-I. Dietrich, C. Weimann, and C. Koos, "Silicon photonic integrated circuits for optical coherence tomography," in *2016 18th International Conference on Transparent Optical Networks (ICTON)* (IEEE, 2016), pp. 1–4.
41. W. Drexler and J. G. Fujimoto, *Optical coherence tomography. Technology and applications* (Springer, 2008).
42. B. J. Vakoc, S. H. Yun, G. J. Tearney, and B. E. Bouma, "Elimination of depth degeneracy in optical frequency-domain imaging through polarization-based optical demodulation," Opt. Lett. **31**, 362–364 (2006).
43. D. Gloge, "Weakly guiding fibers," Appl. Opt. **10**, 2252–2258 (1971).
44. G. K. Grau and W. Freude, *Optische Nachrichtentechnik. Eine Einführung*, 3., völlig neubearbeitete und erw. Aufl. (Springer-Verlag, 1991).
45. C. Blatter, B. Grajciar, C. M. Eigenwillig, W. Wieser, B. R. Biedermann, R. Huber, and R. A. Leitgeb, "Extended focus high-speed swept source OCT with self-reconstructive illumination," Opt. Express **19**, 12141–12155 (2011).
46. K. Petermann, *Laser Diode Modulation and Noise* (Kluwer Academic Publishers; KTK Scientific Publishers, 1988).
47. S. Yun, G. Tearney, J. de Boer, N. Iftimia, and B. Bouma, "High-speed optical frequency-domain imaging," Opt. Express **11**, 2953 (2003).
48. U. Kiencke and R. Eger, *Messtechnik. Systemtheorie für Elektrotechniker*, 6., durchges. und korrigierte Aufl. (Springer, 2005).
49. J. D. Jackson, *Classical electrodynamics*, 2d ed. (Wiley, 1975).
50. C. F. Bohren and D. R. Huffman, *Absorption and scattering of light by small particles* (Wiley, 1983).

51. W. A. Shurcliff, *Polarized light* (Thomson Learning, 1964).
52. R. Barakat, "Bilinear constraints between elements of the 4 x 4 Mueller-Jones transfer matrix of polarization theory," Optics Communications **38**, 159–161 (1981).
53. M. R. Hee, E. A. Swanson, J. G. Fujimoto, and D. Huang, "Polarization-sensitive low-coherence reflectometer for birefringence characterization and ranging," J. Opt. Soc. Am. B **9**, 903 (1992).
54. J. F. de Boer, T. E. Milner, M. J. C. van Gemert, and J. S. Nelson, "Two-dimensional birefringence imaging in biological tissue by polarization-sensitive optical coherence tomography," Opt. Lett. **22**, 934 (1997).
55. C. Hitzenberger, E. Goetzinger, M. Sticker, M. Pircher, and A. Fercher, "Measurement and imaging of birefringence and optic axis orientation by phase resolved polarization sensitive optical coherence tomography," Opt. Express **9**, 780 (2001).
56. J. F. de Boer, T. E. Milner, and J. S. Nelson, "Determination of the depth-resolved Stokes parameters of light backscattered from turbid media by use of polarization-sensitive optical coherence tomography," Opt. Lett. **24**, 300 (1999).
57. B. H. Park, M. C. Pierce, B. Cense, and J. F. de Boer, "Jones matrix analysis for a polarization-sensitive optical coherence tomography system using fiber-optic components," Opt. Lett. **29**, 2512 (2004).
58. G. Yao and L. V. Wang, "Two-dimensional depth-resolved Mueller matrix characterization of biological tissue by optical coherence tomography," Opt. Lett. **24**, 537 (1999).
59. J. Zhang, W. Jung, J. S. Nelson, and Z. Chen, "Full range polarization-sensitive Fourier domain optical coherence tomography," Opt. Express **12**, 6033 (2004).
60. D. Fried, J. Xie, S. Shafi, J. D. B. Featherstone, T. M. Breunig, and C. Le, "Imaging caries lesions and lesion progression with polarization sensitive optical coherence tomography," J. Biomed. Opt. **7**, 618–627 (2002).
61. J. de Boer, S. Srinivas, A. Malekafzali, Z. Chen, and J. Nelson, "Imaging thermally damaged tissue by Polarization Sensitive Optical Coherence Tomography," Opt. Express **3**, 212 (1998).

62. J. Strasswimmer, M. C. Pierce, B. H. Park, V. Neel, and J. F. de Boer, "Polarization-sensitive optical coherence tomography of invasive basal cell carcinoma," Journal of biomedical optics **9**, 292–298 (2004).
63. T. Marvdashti, L. Duan, J. Tang, S. Aasi, and A. E. Bowden, "Machine-learning detection of basal cell carcinoma in human skin using polarization sensitive optical coherence tomography," in *Biomedical Optics 2016* (OSA, 2016), JM4A.5.
64. E. Götzinger, M. Pircher, B. Baumann, C. Hirn, C. Vass, and C. K. Hitzenberger, "Retinal nerve fiber layer birefringence evaluated with polarization sensitive spectral domain OCT and scanning laser polarimetry: a comparison," Journal of biophotonics **1**, 129–139 (2008).
65. J.-T. Oh and S.-W. Kim, "Polarization-sensitive optical coherence tomography for photoelasticity testing of glass/epoxy composites," Opt. Express **11**, 1669–1676 (2003).
66. E. Hecht, *Optik*, 6., verb. Aufl. (Oldenbourg [u.a.], 2014).
67. Saleh, Bahaa E. A. and M. C. Teich, *Grundlagen der Photonik*, 2., vollst. überarb. und erw. Aufl. [=1. dt. Aufl.] (Wiley-VCH, 2008).
68. N. Vansteenkiste, P. Vignolo, and A. Aspect, "Optical reversibility theorems for polarization. Application to remote control of polarization," J. Opt. Soc. Am. A **10**, 2240 (1993).
69. N. C. Pistoni, "Simplified approach to the Jones calculus in retracing optical circuits," Applied optics **34**, 7870–7876 (1995).
70. L. Spanhel, "Colloidal ZnO nanostructures and functional coatings: A survey," J. Sol-Gel Sci. Techn. **39**, 7–24 (2006).
71. J. W. Gilman and T. Kashiwagi, "Nanocomposites: A revolutionary new flame retardant approach," SAMPE J. **33**, 40–46 (1997).
72. B. Liu, P. Soares, C. Checkles, Y. Zhao, and G. Yu, "Three-dimensional hierarchical ternary nanostructures for high-performance Li-ion battery anodes," Nano Lett. **13**, 3414–3419 (2013).
73. J. N. Coleman, U. Khan, and Y. K. Gun'ko, "Mechanical reinforcement of polymers using carbon nanotubes," Adv. Mater. **18**, 689–706 (2006).
74. J. Gaume, C. Taviot-Gueho, S. Cros, A. Rivaton, S. Thérias, and J.-L. Gardette, "Optimization of PVA clay nanocomposite for ultra-barrier

multilayer encapsulation of organic solar cells," Sol. Energ. Mat. Sol. C. **99**, 240–249 (2012).
75. H. Hagendorfer, R. Kaegi, M. Parlinska, B. Sinnet, C. Ludwig, and A. Ulrich, "Characterization of silver nanoparticle products using asymmetric flow field flow fractionation with a multidetector approach - a comparison to transmission electron microscopy and batch dynamic light scattering," Anal. Chem. **84**, 2678–2685 (2012).
76. J. E. Chandler, L. Cherkezyan, H. Subramanian, and V. Backman, "Nanoscale refractive index fluctuations detected via sparse spectral microscopy," Biomed. Opt. Express **7**, 883–893 (2016).
77. S. B. Kondawar, M. D. Deshpande, and S. P. Agrawal, "Transport properties of conductive polyaniline nanocomposites based on carbon nanotubes," Int. J. Comp. Mater. **2**, 32–36 (2012).
78. A. Wurm, D. Lellinger, A. A. Minakov, T. Skipa, P. Pötschke, R. Nicula, I. Alig, and C. Schick, "Crystallization of poly(ε-caprolactone)/MWCNT composites: A combined SAXS/WAXS, electrical and thermal conductivity study," Polymer **55**, 2220–2232 (2014).
79. W. Drexler, U. Morgner, F. X. Kärtner, C. Pitris, S. A. Boppart, X. D. Li, E. P. Ippen, and J. G. Fujimoto, "In vivo ultrahigh-resolution optical coherence tomography," Opt. Lett. **24**, 1221 (1999).
80. S. Schneider, A. Krämer, F. Eppler, H. Alemye, C. Huebner, I. Mikonsaari, J. Leuthold, W. Freude, and C. Koos, "Polarization-sensitive optical coherence tomography for characterization of size and shape of nano-particles," in *CLEO: Science and Innovations* (2013), DOI: 10.1364/CLEO_SI.2013.AF1J.4.
81. W. R. Broughton, T. Koukoulas, P. Woolliams, J. Williams, and S. S. Rahatekar, "Assessment of nanoparticle loading and dispersion in polymeric materials using optical coherence tomography," Polym. Test. **32**, 1290–1298 (2013).
82. J. Kalkman, R. Sprik, and T. G. van Leeuwen, "Path-length-resolved diffusive particle dynamics in spectral-domain optical coherence tomography," Phys. Rev. Lett. **105**, 198302 (2010).
83. R. K. Chhetri, K. A. Kozek, A. C. Johnston-Peck, J. B. Tracy, and A. L. Oldenburg, "Imaging three-dimensional rotational diffusion of plasmon

resonant gold nanorods using polarization-sensitive optical coherence tomography," Phys. Rev. B **83**, 40903 (2011).

84. A. Wax, C. Yang, V. Backman, M. Kalashnikov, R. R. Dasari, and M. S. Feld, "Determination of particle size by using the angular distribution of backscattered light as measured with low-coherence interferometry," J. Opt. Soc. Am. A **19**, 737 (2002).
85. N. Bosschaart, D. J. Faber, T. G. van Leeuwen, and M. C. G. Aalders, "Measurements of wavelength dependent scattering and backscattering coefficients by low-coherence spectroscopy," J. Biomed. Opt. **16**, 30503 (2011).
86. S. A. Alexandrov, J. McGrath, H. Subhash, F. Boccafoschi, C. Giannini, and M. Leahy, "Novel approach for label free super-resolution imaging in far field," Sci. Rep. **5**, 13274 (2015).
87. P. E. Stanga, A. Sala-Puigdollers, S. Caputo, H. Jaberansari, M. Cien, J. Gray, Y. D'Souza, S. J. Charles, S. Biswas, D. B. Henson, and D. McLeod, "In vivo imaging of cortical vitreous using 1050-nm swept-source deep range imaging optical coherence tomography," Am. J. Ophthalmol. **157**, 397-404.e2 (2014).
88. K. Wiesauer, M. Pircher, E. Goetzinger, C. K. Hitzenberger, R. Engelke, G. Ahrens, G. Gruetzner, and D. Stifter, "Transversal ultrahigh-resolution polarization-sensitive optical coherence tomography for strain mapping in materials," Opt. Express **14**, 5945–5953 (2006).
89. V. M. Kodach, D. J. Faber, J. van Marle, T. G. van Leeuwen, and J. Kalkman, "Determination of the scattering anisotropy with optical coherence tomography," Opt. Express **19**, 6131–6140 (2011).
90. L. Thrane, M. H. Frosz, T. M. Jørgensen, A. Tycho, H. T. Yura, and P. E. Andersen, "Extraction of optical scattering parameters and attenuation compensation in optical coherence tomography images of multilayered tissue structures," Opt. Lett. **29**, 1641–1643 (2004).
91. M. Almasian, N. Bosschaart, T. G. van Leeuwen, and D. J. Faber, "Validation of quantitative attenuation and backscattering coefficient measurements by optical coherence tomography in the concentration-dependent and multiple scattering regime," J. Biomed. Opt. **20**, 121314-1-121314-11 (2015).

92. S. A. Hojjatoleslami and J. Kittler, “Region growing: A new approach,” IEEE T. Image Process. **7**, 1079–1084 (1998).
93. L. Thrane, H. T. Yura, and P. E. Andersen, “Analysis of optical coherence tomography systems based on the extended Huygens–Fresnel principle,” J. Opt. Soc. Am. A **17**, 484 (2000).
94. M. F. L. De Volder, S. H. Tawfick, R. H. Baughman, and A. J. Hart, “Carbon nanotubes: present and future commercial applications,” Science **339**, 535–539 (2013).
95. G. Olowojoba, S. Sathyanarayana, B. Caglar, B. Kiss-Pataki, I. Mikonsaari, C. Hübner, and P. Elsner, “Influence of process parameters on the morphology, rheological and dielectric properties of three-roll-milled multiwalled carbon nanotube/epoxy suspensions,” Polymer **54**, 188–198 (2013).
96. V. J. Gokhale, O. A. Shenderova, G. E. McGuire, and M. Rais-Zadeh, “Infrared Absorption Properties of Carbon Nanotube/Nanodiamond Based Thin Film Coatings,” J. Microelectromech. Syst. **23**, 191–197 (2014).
97. K. Kohlgrüber, *Co-Rotating Twin-Screw Extruder* (Carl Hanser Verlag GmbH & Company KG, 2012).
98. S. Schneider, M. Lauermann, P.-I. Dietrich, C. Weimann, W. Freude, and C. Koos, “Optical coherence tomography system mass-producible on a silicon photonic chip,” Opt. Express **24**, 1573–1586 (2016).
99. V. Leitgeb, A. Trügler, S. Köstler, M. K. Krug, U. Hohenester, A. Hohenau, A. Leitner, and J. R. Krenn, “Three dimensional sensitivity characterization of plasmonic nanorods for refractometric biosensors,” Nanoscale **8**, 2974–2981 (2016).
100. E. Martinsson, M. M. Shahjamali, N. Large, N. Zaraee, Y. Zhou, G. C. Schatz, C. A. Mirkin, and D. Aili, “Influence of Surfactant Bilayers on the Refractive Index Sensitivity and Catalytic Properties of Anisotropic Gold Nanoparticles,” Small (Weinheim an der Bergstrasse, Germany) **12**, 330–342 (2016).
101. R. Narayanan and M. A. El-Sayed, “Shape-dependent catalytic activity of platinum nanoparticles in colloidal solution,” Nano Lett. **4**, 1343–1348 (2004).

102. S. Shukla, F. J. Eber, A. S. Nagarajan, N. A. DiFranco, N. Schmidt, A. M. Wen, S. Eiben, R. M. Twyman, C. Wege, and N. F. Steinmetz, "The Impact of Aspect Ratio on the Biodistribution and Tumor Homing of Rigid Soft-Matter Nanorods," Advanced healthcare materials **4**, 874–882 (2015).
103. C. M. Hoo, N. Starostin, P. West, and M. L. Mecartney, "A comparison of atomic force microscopy (AFM) and dynamic light scattering (DLS) methods to characterize nanoparticle size distributions," J Nanopart Res **10**, 89–96 (2008).
104. G. Göring, P.-I. Dietrich, M. Blaicher, S. Sharma, J. G. Korvink, T. Schimmel, C. Koos, and H. Hölscher, "Tailored probes for atomic force microscopy fabricated by two-photon polymerization," Appl. Phys. Lett. **109**, 63101 (2016).
105. A. L. Oldenburg, R. K. Chhetri, J. M. Cooper, W.-C. Wu, M. A. Troester, and J. B. Tracy, "Motility-, autocorrelation-, and polarization-sensitive optical coherence tomography discriminates cells and gold nanorods within 3D tissue cultures," Opt. Lett. **38**, 2923–2926 (2013).
106. A. I. Carswell and S. R. Pal, "Polarization anisotropy in lidar multiple scattering from clouds," Applied optics **19**, 4123–4126 (1980).
107. G. D. Lewis, D. L. Jordan, and P. J. Roberts, "Backscattering target detection in a turbid medium by polarization discrimination," Applied optics **38**, 3937 (1999).
108. CST of America, "An integral equation solver for military applications," Microwave Journal (2007).
109. B. T. Draine and P. J. Flatau, "Discrete-Dipole Approximation For Scattering Calculations," J. Opt. Soc. Am. A **11**, 1491 (1994).
110. M. A. Yurkin, D. de Kanter, and A. G. Hoekstra, "Accuracy of the discrete dipole approximation for simulation of optical properties of gold nanoparticles," J. Nanophoton **4**, 41585 (2010).
111. T. L. Farias, U. O. Koylu, and M. G. Carvalho, "Range of validity of the Rayleigh-Debye-Gans theory for optics of fractal aggregates," Applied optics **35**, 6560–6567 (1996).

112. M. I. Mishchenko, L. D. Travis, and D. W. Mackowski, "T-matrix computations of light scattering by nonspherical particles. A review," Journal of Quantitative Spectroscopy and Radiative Transfer **55**, 535–575 (1996).
113. B. N. Khlebtsov and N. G. Khlebtsov, "Multipole Plasmons in Metal Nanorods. Scaling Properties and Dependence on Particle Size, Shape, Orientation, and Dielectric Environment," J. Phys. Chem. C **111**, 11516–11527 (2007).
114. O. L. Muskens, G. Bachelier, N. D. Fatti, F. Vallée, A. Brioude, X. Jiang, and M.-P. Pileni, "Quantitative absorption spectroscopy of a single gold nanorod," J. Phys. Chem. C **112**, 8917–8921 (2008).
115. P. B. Johnson and R. W. Christy, "Optical constants of the noble metals," Phys. Rev. B **6**, 4370–4379 (1972).
116. P. Drude, "Zur Elektronentheorie der Metalle," Ann. Phys. **306**, 566–613 (1900).
117. R. C. Jones, "A new calculus for the treatment of optical systems," J. Opt. Soc. Am. **31**, 488 (1941).
118. M. Hochberg, N. C. Harris, R. Ding, Y. Zhang, A. Novack, Z. Xuan, and T. Baehr-Jones, "Silicon photonics: the next fabless semiconductor industry," IEEE Solid-State Circuits Mag. **5**, 48–58 (2013).
119. S. Schneider, M. Lauermann, C. Weimann, W. Freude, and C. Koos, "Silicon photonic optical coherence tomography system," in *CLEO: Applications and Technology* (2014), paper ATu2P.4.
120. G. Yurtsever, N. Weiss, J. Kalkman, T. G. van Leeuwen, and R. Baets, "Ultra-compact silicon photonic integrated interferometer for swept-source optical coherence tomography," Opt. Lett. **39**, 5228–5231 (2014).
121. Z. Wang, H.-C. Lee, D. Vermeulen, L. Chen, T. Nielsen, S. Y. Park, A. Ghaemi, E. Swanson, C. Doerr, and J. Fujimoto, "Silicon photonic integrated circuit swept-source optical coherence tomography receiver with dual polarization, dual balanced, in-phase and quadrature detection," Biomed. Opt. Express **6**, 2562–2574 (2015).
122. V. D. Nguyen, N. Weiss, W. Beeker, M. Hoekman, A. Leinse, R. G. Heideman, T. G. van Leeuwen, and J. Kalkman, "Integrated-optics-based swept-source optical coherence tomography," Opt. Lett. **37**, 4820–4822 (2012).

123. B. I. Akca, D. van Nguyen, J. Kalkman, N. Ismail, G. Sengo, F. Sun, A. Driessen, T. G. van Leeuwen, M. Pollnau, K. Wörhoff, and R. M. de Ridder, "Toward spectral-domain optical coherence tomography on a chip," IEEE J. Select. Topics Quantum Electron. **18**, 1223–1233 (2012).
124. B. I. Akca, A. Alex, R. M. de Ridder, W. Drexler, M. Pollnau, B. Povazay, and K. Wörhoff, "Miniature spectrometer and beam splitter for an optical coherence tomography on a silicon chip," Opt. Express **21**, 16648–16656 (2013).
125. N. Lindenmann, S. Dottermusch, M. L. Goedecke, T. Hoose, M. R. Billah, T. P. Onanuga, A. Hofmann, W. Freude, and C. Koos, "Connecting silicon photonic circuits to multicore fibers by photonic wire bonding," J. Lightwave Technol. **33**, 755–760 (2015).
126. A. M. Rollins and J. A. Izatt, "Optimal interferometer designs for optical coherence tomography," Opt. Lett. **24**, 1484 (1999).
127. F. Morichetti, A. Canciamilla, C. Ferrari, M. Torregiani, A. Melloni, and M. Martinelli, "Roughness induced backscattering in optical silicon waveguides," Physical review letters **104**, 33902 (2010).
128. G. Kurczveil, P. Pintus, M. J. R. Heck, J. D. Peters, and J. E. Bowers, "Characterization of insertion loss and back reflection in passive hybrid silicon tapers," IEEE Photonics J. **5**, 6600410 (2013).
129. Y. Yasuno, V. D. Madjarova, S. Makita, M. Akiba, A. Morosawa, C. Chong, T. Sakai, K.-P. Chan, M. Itoh, and T. Yatagai, "Three-dimensional and high-speed swept-source optical coherence tomography for in vivo investigation of human anterior eye segments," Opt. Express **13**, 10652 (2005).
130. Z. Chen, T. E. Milner, D. Dave, and J. S. Nelson, "Optical Doppler tomographic imaging of fluid flow velocity in highly scattering media," Opt. Lett. **22**, 64 (1997).
131. B. F. Kennedy, K. M. Kennedy, and D. D. Sampson, "A review of optical coherence elastography: fundamentals, techniques and prospects," IEEE J. Select. Topics Quantum Electron. **20**, 272–288 (2014).
132. J. Heo, E. Jang, S. Haam, S. J. Oh, Y.-M. Huh, J.-S. Suh, E. Chung, and C. Joo, "In vivo photothermal optical coherence tomography of targeted

mouse brain tumors using gold nanostars," in *CLEO: Science and Innovations* , SM4P.3.
133. M. Bonesi, M. P. Minneman, J. Ensher, B. Zabihian, H. Sattmann, P. Boschert, E. Hoover, R. A. Leitgeb, M. Crawford, and W. Drexler, "Akinetic all-semiconductor programmable swept-source at 1550 nm and 1310 nm with centimeters coherence length," Opt. Express **22**, 2632–2655 (2014).
134. U. Kiencke and H. Jäkel, *Signale und Systeme*, 4., korrigierte Aufl. (Oldenbourg, 2008).
135. K. D. Kammeyer and K. Kroschel, *Digitale Signalverarbeitung*. *Filterung und Sprektralanalyse* (Teubner, 1989).
136. F. J. Harris, "On the use of windows for harmonic analysis with the discrete Fourier transform," Proc. IEEE **66**, 51–83 (1978).
137. F. Constantinescu, *Distributionen und ihre Anwendung in der Physik* (Teubner, 1974).
138. Saleh, Bahaa E. A. and M. C. Teich, *Fundamentals of Photonics*, 2nd ed. (Wiley-Interscience, 2007).
139. W. Freude, *Field Propagation and Coherence*, Lecture notes, Karlsruhe Institute of Technology (KIT), 2011.

C. Glossary

C.1 List of acronyms

A-Scan	One-dimensional (1D) OCT depth scan
A1,2	Anode of a diode with contacts 1,2
ACF	Autocorrelation function
ADC	Analogoue-to-digital converter
AF	Area fraction
AFM	Atomic force microscopy
APC	Angled physical contact connector
AR	Aspect ratio
AWG	Arrayed waveguide grating
B-Scan	2-D OCT cross sectional scan
BD	Balanced detector
BL	Ball lens
BS	Beam splitter
C-Scan	3-D OCT volumetric scan
C1,2	Cathode of a diode with contacts 1,2
CCD	Charge-coupled device
CMOS	Complementary metal-oxide-semiconductor technology
CMRR	Common-mode rejection ratio
CNT	Carbon nanotube
CPL	Optical 3-dB coupler
DDA	Discrete-Dipole Approximation

DFT	Discrete Fourier transform
DLS	Dynamic light scattering
DR	Dynamic range
FC	Fibre collimator
FD-OCT	Fourier-domain optical coherence tomography
FT	Fourier transform
FWHM	Full width at half the maximum
G1, G2	Gold nanorod samples in aqueous dispersion
HWP	Half-wave plate
IDFT	Inverse discrete Fourier transform
ITO	Indium tin oxide
LF	Lensed fibre
LM	Light microscope
LP-modes	Linear polarized modes in fibres or cylindrical waveguides
MMI	Multimode interference
MoM	Method of Moments numeric field calculation approach
MPW	Multi-project-wafer
MWCNT	Multi-wall carbon nanotube
NEP	Noise-equivalent power
NIST	National Institute of Standards and Technology
OCT	Optical coherence tomography
OCT*ext*	Integrated OCT system with external reference arm
OCT*int*	Integrated OCT system with internal integrated reference arm
PA	Polyamide

PAR	Perimeter-to-area ratio
$\overline{\text{PAR}}$	Modified pixel-wise PAR
PBS	Polarization beam splitter
PC	Personal computer
PD	Photodiode
PIC	Photonic integrated circuit
PL	Polymer microlens
PMF	Polarization-maintaining fibre
Pol	Polarizer
PolC	Polarization controller
PP	Polypropylene
PS	Polystyrene
PS-BD	Polarization-sensitive balanced detector
PWC	Partial wave spectroscopic microscopy
QWP	Quarter-wave plate
RDG	Rayleigh-Debye-Gans Theory
RIN	Relative intensity noise
RMS	Root mean square
RP	Reference path
S1, S2, S3, S4	Nanoparticle samples with different concentration and nanosphere diameter
SAXS	Small-angle X-ray scattering
SD-OCT	Spectral-domain optical coherence tomography
SEM	Scanning electron microscopy
SESF	Spectral encoding of spatial frequency

SLD	Superluminescent diode
SLS	Static light scattering
SMF	Single-mode fibre
SNR	Signal-to-noise ratio
SOI	Silicon-on-insulator
SP	Sample path
SS	Swept-laser source
SS-OCT	Swept-source optical coherence tomography
TD-OCT	Time-domain optical coherence tomography
TE mode	Transverse electric mode
TEM	Transmission electron microscopy
TIA	Transimpedance amplifier
TRPS	Tunable resistive pulse shaping
XRD	X-ray diffraction

C.2 List of symbols

Greek symbols

Symbol		Unit
α	Orientation angle of the electric field	rad
γ	Strain amplitude	1
$\underline{\gamma}_{q_1,q_2}$	Normalized coherence function of ergodic fields in spatial directions q_1, q_2	1
$\underline{\Gamma}_{\mathrm{L}}(\tau)$	Complex coherence function of the source field	$\mathrm{V}^2/\mathrm{m}^2$

$\underline{\Gamma}_{q_1, q_2}$	Coherence function of ergodic fields in spatial directions q_1, q_2	V^2/m^2
$\underline{\breve{\Gamma}}_{q_1, q_2}$	Mutual spectral density of two fields in spatial directions q_1, q_2	V^2s/m^2
$\delta(x)$	Dirac delta distribution	
δ	Common phase in Jones vector	rad
δ_{dB}	Difference in parasitic reference power to nominal reference power (OCT*ext*)	dB
δf	Instantaneous source bandwidth	Hz
δf_{d}	Frequency step size after sampling	Hz
$\delta P_0(t)$	Mean-free optical power fluctuations $\delta P_0(t) = P_0(t) - \overline{P_0(t)}$	W
$\delta r, \delta x, \delta y$	Lateral resolution of an OCT system	m
δt_{d}	Sampling-related resolution in sample return time	s
δt_{s}	Measurement resolution of the sample response time	s
δu_{q}	Quantization voltage step size	V
δz	Axial (depth) resolution of an OCT system	m
Δ_{tot}	Total ratio of measurement and simulation in particle shape determination	dB
Δf	Optical measurement bandwidth in FD-OCT	Hz
Δf_{el}	Electrical measurement bandwidth	Hz
Δf_{d}	Total frequency range after sampling	Hz
Δt_{d}	Unambiguity range in sample return time due to sampling	s

Δt	Temporal width of an exemplary rectangular function	s
Δt_s	Coherence limited measurable time range of sample responses	s
Δz	Coherence related imaging depth	m
Δz_f	Focal measurement range	m
$\Delta\lambda$	Wavelength span of an OCT light source	m
$\Delta\sigma_t, \Delta\sigma_{b,m}, \Delta\eta$	Ratio of simulated and measured scattering cross section, polarization maintaining backscattering cross section and polarization cross talk, respectively	dB
$\Delta\varphi$	Optical phase difference of light returning from sample and reference arm	rad
ε_0	Vacuum permittivity $\varepsilon_0 = 1/\left(\mu_0 c_0^2\right) \approx 8.854\times10^{-12}$ As/(Vm)	$\mathrm{As}/(\mathrm{Vm})$
ε_{AR}	Relative accuracy in particle aspect ratio determination	1
ε_d	Accuracy in particle diameter determination	m
ε_r	Relative permittivity	1
ζ	Common-mode power rejection ratio of a balanced detector (linear)	1
ζ_{dB}	Common-mode power rejection ratio of on-chip receiver (dB)	dB
$\eta_f(r,z)$	Focal power response function of an OCT system	1
η	Polarization cross talk in PS-OCT measurements	1

ϑ_Q, ϑ_P	Rotation angle of the fast axis of the QWP (ϑ_Q) and of the transmission axis of the polarizer (ϑ_P) with respect to the horizontal axis	rad
$\vartheta_{y_1 y_2}(\tau)$	Temporal correlation of the signals y_1, y_2.	
$\kappa_L(\tau)$	Real-valued normalized baseband coherence function of the source field	1
λ	Optical wavelength in vacuum, $\lambda = c_0/f$	m
λ_m	Central wavelength of an OCT light source	m
μ_0	Magnetic permittivity, $\mu_0 = 4\pi \times 10^{-7}$ N/A^2	N/A^2
$\mu_{b,m}$, $\mu_{b,c}$	Polarization maintaining (m) and cross-polarized (c) backscattering coefficient	m^{-1}
μ_r	Relative magnetic permittivity	1
$\mu_{t,b}$	Extinction μ_t and backscattering coefficient μ_b	m^{-1}
ν	Factor describing fractions of a particle diameter	1
ρ	Responsivity of the photodiode	A/W
$\rho_{BG,dB}$	Backscatter floor of OCT*ext*	dB
$\rho_{WG,dB}$	Distributed on-chip waveguide backscatter within resolution δz	dB
$\sigma_{a,s,t,b}$	Absorption- σ_a, total scattering- σ_s, extinction- σ_t, and backscattering cross section σ_b	m^2
$\sigma_{b,m}$, $\sigma_{b,c}$	Polarization maintaining (m) and cross-polarized (c) backscatter cross section	m^2

τ	Time difference	s
τ_{r}	Reference mirror return time	s
τ_{c}	Coherence time	s
φ	Relative phase in Jones vector	rad
φ_0	Constant phase offset in an SS-OCT signal	rad
$\varphi_{\mathrm{G}}(z)$	Gouy phase in a Gaussian beam	rad
$\Phi(x)$	Arbitrary test function on *x*, indefinitely often differentiable and outside a limited region identically zero.	
ω	Optical angular frequency, $\omega = 2\pi f$	s^{-1}
ω_0	Optical angular carrier frequency of the light source	s^{-1}

Latin symbols

Symbol		Unit
a	Parameter of a Gauss function	s^{-2}
a_{dB}	Lensed port power loss (OCT*ext*)	dB
A	Electric field amplitude	V/m
$\vec{A}$, $A_{x,y,z}$	Electric field amplitude vector and *x*,*y*,*z* components thereof	V/m
$\underline{A}_0$	Slowly-varying random amplitude of the source field	V/m
$A_{\mathrm{G}}(r,z)$	Complex field amplitude of a Gaussian beam with maximum $A_{\mathrm{G},0}$	V/m
A_i	Individual agglomerate area	m^2
A_{tot}	Imaging cross section	m^2

b	Confocal parameter of a Gaussian beam	m
b_r	Mechanical oscillation amplitude of a rheometer	m
$\vec{B}$	Magnetic induction field vector	T
c_0	Vacuum speed of light, $c_0 = 299\,792\,458\ \mathrm{m/s}$	m/s
d	Diameter of a scatterer	m
d_G	Nanorod diameters of samples G1 and G2	m
$\vec{D}$	Electric displacement field vector	As/m²
$\vec{e}_x$, $\vec{e}_y$, $\vec{e}_z$	Unit vectors	1
$\vec{E}$	Electric field vector	V/m
$\underline{E}_0$	Electric field emitted by the light source	V/m
$\underline{E}_\mathrm{d}$	Electric field measured at the photodetector	V/m
$\underline{\vec{E}}_\mathrm{in}$	Electric field vector of polarized incident electric field	V/m
$\underline{\vec{E}}_\mathrm{out}$, $\underline{\vec{E}}_\mathrm{out,m}$, $\underline{\vec{E}}_\mathrm{out,c}$	Electric field vector of polarized output electric field $\underline{\vec{E}}_\mathrm{out}$, polarization maintaining (m) and cross-polarized (c)	V/m
$\underline{E}_\mathrm{r}$	Electric field reflected by the reference mirror, measured after second pass of the beam splitter	V/m
$\underline{E}_\mathrm{s}$	Electric field backscattered from the sample, measured after second pass of the beam splitter	V/m
f	Frequency	Hz
f'	Auxiliary frequency variable, replacing f	Hz

f_0	Optical carrier frequency of the light source	Hz
$f_{\mathrm{a,b}}$	Baseband frequency in RIN measurement	Hz
f_{d}	Sampling frequency	Hz
f_{c}	Electrical carrier frequency	Hz
f_{m}	Centre frequency of a FD-OCT frequency span	Hz
f_{sig}	OCT signal frequency	Hz
F_0	Electric field-covered area of the source emitted beam	m^2
F_{c}	Coherence area	m^2
$\underline{g}_{q_1, q_2}$	Normalized coherence function of fields in spatial directions q_1, q_2	1
$\underline{G}_{q_1, q_2}$	Coherence function of the first order of fields in spatial directions q_1, q_2	$\mathrm{V}^2/\mathrm{m}^2$
$h_{\mathrm{s}}(t)$, $h_{\mathrm{r}}(t)$	Field impulse responses of sample and reference path	s^{-1}
$\breve{\underline{h}}_{\mathrm{s}}(f)$, $\breve{\underline{h}}_{\mathrm{r}}(f)$	Complex field transfer function of sample and reference path	Hz^{-1}
$\vec{H}$	Magnetic field vector	A/m
i	Counting variable, e. g. in a DFT	1
i_{c}	OCT photocurrent related to sample-reference interference	A
i'_{c}	Effective OCT photocurrent related to sample-reference interference, $i'_c = 2\,\mathrm{Re}\left\{\underline{E}_s \underline{E}_r^*\right\} \sim i_c$	$\mathrm{V}^2/\mathrm{m}^2$

$\breve{i}_c'$	Fourier transformed effective OCT photocurrent	V^2/m^2
$i_{d,d1,d2}$	Photocurrent in general or from PD 1 or PD 2, respectively	A
i_{max}	Maximum photocurrent	A
i_n	Total noise current	A
i_q	Quantization noise current	A
i_{RIN}	RIN-current	A
$i_{sig,BD}$	OCT signal current after balanced detection	A
$i_{sig,lim}$	Equivalent photocurrent according to ADC or PD limitation	A
i_{sh}	Shot noise current	A
i_{dn}	Detector noise current	A
I_{tot}, I_{hor}, I_{ver}, I_{45}, I_{135}, I_{RZ}, I_{LZ}	Light intensities depending on polarization: total I_{tot}, horizontal I_{hor}, vertical I_{ver}, at 45° I_{45}, at 135° I_{135}, right-circular I_{RZ}, and left-circular I_{LZ}	W/m²
$I_G(r,z)$	Intensity of a Gaussian beam with maximum $I_{G,0}$ at the focus	W/m²
j	Imaginary unit, $j=\sqrt{-1}$	1
$\vec{J}$, $J_{x,y}$	Jones vector and *x*,*y* components thereof	1
$\vec{J}_{in}$, $\vec{J}_m$	Jones vector exiting the fibre towards the sample $(\vec{J}_{in})$ and entering the PS-BD $(\vec{J}_m)$	1
$\vec{J}_s$, $\vec{J}_r$	Jones vectors towards sample (s) and towards reference (r) arm in the free-space PS-OCT setup in Figure 2.12	1

$\mathbf{J}$	Jones matrix; transformation of Jones vectors	1
$\mathbf{J}_{\mathrm{ref}}$	Jones matrix of the reference arm in the free-space PS-OCT setup in Figure 2.12	1
$\mathbf{J}_{\mathrm{rev}}$	Jones matrix of reverse propagation through any optical reciprocal material	1
$\mathbf{J}_{\mathrm{QWP}}$, $\mathbf{J}_{\mathrm{HWP}}$, $\mathbf{J}_{\mathrm{Pol}}$, $\mathbf{J}_{\mathrm{s}}$, $\mathbf{J}_{\mathrm{sys}}$, $\mathbf{J}_{\mathrm{M}}$	Jones matrices of a QWP, a HWP, a Polarizer (Pol), a sample (s), a fibre optic system (sys) and a plane mirror (M)	1
k	Angular optical wavenumber, $k = 2\pi/\lambda$	m^{-1}
$\vec{k}$, $k_{x,y,z}$	Optical wave vector and x,y,z components thereof	m^{-1}
$k_{\mathrm{L}}(\tau)$	Real-valued normalized coherence function of the source field	1
$K_{\mathrm{L}}(\tau)$	Real-valued coherence function of the source field	$\mathrm{V}^2/\mathrm{m}^2$
l_{c}	Coherence length	m
l_{G1}, l_{G2}	Nanorod lengths of samples G1 and G2	m
m	Counting variable, e. g. in a DFT	1
$m_{1\ldots4}$	Jones matrix elements of an optical reciprocal material	1
M	Number of sampling points in a DFT	1
n	Refractive index. Refractive index of sample n_{s}, and reference path n_{r}.	1
n_{q}	Quantization error of a voltage signal	V
N	Volume number density	m^{-3}
p_{b}	Backscattering probability	1

p_q	Probability density of quantization noise inside quantization interval	1
P	Optical power	W
P_0	Optical power emitted by the source	W
P_b	Optical power scattered back from the sample	W
P_d	Optical power at photodetector	W
P_{in}	Optical power incident on the sample	W
P_{out}, $P_{out,m}$, $P_{out,c}$	Optical output power (P_{out}), with maintained polarization (m) and cross-polarized (c)	W
$P_{s,r}$	Optical power incident on one detector photodiode, which is returned from the sample path or the reference path, respectively.	W
$\vec{P}$	Material polarization vector	As/m²
q	Decay calibration factor in an OCT measurement	m^{-1}
q_0	Elementary charge, $q_0 = 1.602 \times 10^{-19}$ C	C
Q	Power calibration factor in an OCT measurement	1
r	Radius with respect to the optical axis	m
$\vec{r}$	Spatial vector, e.g. propagation direction of an electric field	m
r_c	Coherence radius	m
$r_r(z)$	Amplitude reflectivity depth-profile of the reference path	m^{-1}

r_R	Amplitude reflectivity of the reference mirror	1
$r_s(z)$	Amplitude reflectivity depth-profile of the sample	m^{-1}
$\mathbf{R}(\vartheta)$	Rotation matrix, with rotation angle ϑ	1
$R_0(z)$	Theoretical backscattering factor from a scattering sample, excluding influences of the measurement system	1
$R_{dB}(z)$	Semi-logarithmic OCT backscatter signal	dB
$R_G(z)$	Radius of curvature of the phase fronts of a Gaussian beam	m
R_m, R_c	Backscatter factor with maintained polarization (m) and cross-polarized (c)	m^{-1}
R_n	Noise floor in an OCT measurement, expressed in minimum measurable power reflectivity of a sample	1
R_R	Power reflectivity of the reference mirror	1
$R_s(z)$	Depth-dependent power reflectivity profile of the sample	m^{-1}
R_S	Power reflectivity of a sample reflector	1
$R_{xx}, R_{yx}, R_{xy}, R_{yy}$	Backscattering coefficient R_{ij} denoting scattering of *i*- into *j*-polarization	m^{-1}
$\mathrm{RIN}(f - f_c)$	Spectral RIN density around carrier frequency f_c	Hz^{-1}
$\mathrm{RIN}_{dB}(f - f_c)$	RIN in 1 Hz bandwidth around carrier f_c	dB Hz^{-1}
RIN_{tot}	Total RIN integrated over entire spectrum	1

$\mathrm{RIN}_{\mathrm{z}}(z-z_{\mathrm{c}})$	Spatial RIN profile around reflection at z_{c}	mm^{-1}
$\mathrm{RIN}_{\mathrm{z,\,dB}}(z-z_{\mathrm{c}})$	Spatial RIN within OCT depth resolution δz	dB (8 µm)$^{-1}$
s	Rheometer plate distance	m
s_i	Perimeter of a single agglomerate	m
s_{sw}	Tuning slope of a swept-source laser	Hz/s
S	Sensitivity of the OCT system, expressed in sample power reflectivity	1
$\vec{S}$	Poynting vector	$\mathrm{W/m^2}$
$\vec{S}_{\mathrm{t}}$	Stokes vector describing the polarization of light	$\mathrm{W/m^2}$
t	Time	s
t_0	Frequency ramp start time	s
t_{r}	Reference path return time	s
t_{s}	Sample path return time	s
T	Absolute temperature	K
T_{sw}	Swept-source ramp duration	s
u_0, u_{q}	Input signal u_0 and output signal u_{q} of a quantizer. Here: voltage signals	V
u_1, u_2	Matrix elements of a unitary Jones matrix	1
$u_{\mathrm{max,PD}}$, $u_{\mathrm{max,ADC}}$	Voltage saturation limits of photodetector and ADC, respectively.	V
$u_{\mathrm{sig,BD}}$	OCT signal voltage after balanced detection	V

$v_{s,r}$	Speed of light in sample and reference arm, respectively	m/s
w_0	Waist radius of a Gaussian beam	m
$w(z)$	Radius of a Gaussian beam over axial position	m
$W(f_0)$	Spectral windowing function	1
$\breve{W}(t)$	Temporal windowing function	1
x	Lateral spatial coordinate in an OCT measurement	m
	Arbitrary variable in exemplary functions	
y	Lateral spatial coordinate in an OCT measurement	m
$y(t)$	Arbitrary time-dependent function	
$\breve{y}(f)$	Correspondent function to $y(t)$, after Fourier transform, with dependence on frequency *f*.	
y_m	Time-data vector element in a DFT	
$\breve{y}_i$	Frequency-data vector element in a DFT	
z	Depth axis of an OCT measurement	m
$z_{1...9}$	Depth position of a sample mirror	m
$z_{a,b}$	RIN probing depth	m
z_c	Depth position of a reflection peak	m
$z_{edge,int}$	Facet position of OCT*int* chip	m
$z_{edge,ext}$	Facet position of OCT*ext* chip	m
z_f	Beam waist position of a Gaussian beam	m

z_{geo}	Depth axis of an OCT measurement (geometrical depth)	m
z_O	Depth position of the beam splitter	m
z_r	Depth position of the reference mirror	m
z_s	Depth position of the sample	m
Z_0	Impedance of free space	Ω
Z_a	Transimpedance gain of the photodiode amplifier	V/A

Danksagung

Die vorliegende Dissertation entstand während meiner Tätigkeit am Institut für Photonik und Quantenelektronik (IPQ) am Karlsruher Institut für Technologie (KIT). Große Teile dieser Arbeit gehen auf Ergebnisse des von der Baden-Württemberg Stiftung geförderten Projekts „Charakterisierung von polymeren Nanokompositen (ChaPlyN)“ zurück und entstanden unter dem Dach des Doktorandenprogramms der Karlsruhe School of Optics and Photonics (KSOP). Zuletzt bleibt mir die angenehme Aufgabe mich bei all jenen zu bedanken, die mich in den letzten Jahren unterstützt und damit wesentlich zum Gelingen dieser Arbeit beigetragen haben.

Zunächst gilt mein besonderer Dank meinem Doktorvater Prof. Christian Koos, der diese Arbeit überhaupt erst ermöglicht hat. Vielen Dank für das entgegengebrachte Vertrauen, die Betreuung, sowie für die Bereitstellung der Infrastruktur und der finanziellen Mittel. Als steter Quell neuer Ideen und durch seine visionäre Weitsicht trug er maßgeblich zu dieser Arbeit bei.

Herrn Prof. Wolfgang Freude danke ich für die Übernahme des Korreferates, sowie für seinen nimmermüden Einsatz bei der Durchsicht und Überarbeitung sämtlicher Manuskripte. Er dient mir als Vorbild wissenschaftlicher Präzision und sprachlicher Exaktheit. Vielen Dank für den tiefgreifenden fachlichen Austausch und die eingebrachte Expertise.

Mein weiterer Dank gilt Prof. Jürg Leuthold, der zu Beginn meiner Tätigkeit Institutsleiter war und meine Arbeit unterstützte.

Darüber hinaus danke ich Prof. Wilhelm Stork für die Übernahme des Korreferates, sowie für Anregungen und Korrekturvorschläge.

Die Arbeit war eingebunden in das Doktorandenprogramm der KSOP. Ich möchte mich an dieser Stelle für deren finanzielle Unterstützung, sowie für die Begleitung durch meine beiden Mentoren Dr. Timo Mappes und Dr. Martin Lauer bedanken.

Wesentliche Teile dieser Arbeit entstanden im Rahmen des von der Baden-Württemberg Stiftung geförderten Projekts „Charakterisierung von polymeren Nanokompositen (ChaPlyN)“. Ich bedanke mich bei allen Projektpartnern für die gemeinsame Arbeit und bei der Baden-Württemberg Stiftung für die Projektförderung. Besonders danken möchte ich Irma Mikonsaari und Dr. Christof Hübner, sowie ihren Kollegen vom Fraunhofer Institut für Chemische Technologie in Pfinztal für die gute Zusammenarbeit, die Probenherstellung und Charakterisierung, sowie für das Ermöglichen einer gemeinsamen Messkampagne.

Besonderer Dank gilt meinen Doktorandenkollegen und Postdocs, mit denen ich viele bereichernde Momente im Labor, bei der Betreuung von Lehrveranstaltungen, auf Konferenzen, auf Ausflügen, am Kickertisch oder am Grill auf dem Institutsdach verbringen konnte. Vielen Dank für die tolle Atmosphäre und den guten Zusammenhalt. Hervorheben möchte ich meine Bürokollegen Kira Köhnle, Wladislaw Hartmann, Dr. Matthias Lauermann, Aleksandar Nesic, Dr. Jörg Pfeifle und Claudius Weimann. Dr. Nicole Lindenmann danke ich speziell für ihre Unterstützung in der ersten Zeit und Dr. Stefan Wolf für die vielen Tipps in der Endphase dieser Arbeit. Dem Übungsleiterteam zur Veranstaltung Halbleiterbauelemente um Wladislaw Hartmann, Dr. Matthias Lauermann, Sascha Mühlbrandt und Dr. Robert Palmer danke ich für viele lehrreiche Stunden die wir gemeinsam verbracht haben. Für die Umsetzung meiner integriert-photonischen Messkonzepte in hervorragendem Chip Design danke ich Dr. Matthias Lauermann. Philipp-Immanuel Dietrich gebührt Dank für die ersten 3D-lithographisch hergestellten Mikrolinsen zur stabilen optischen Ankopplung des optischen Kohärenztomographie-Chips.

Ein großes Dankeschön geht an das Team im Sekretariat. Bernadette Lehmann, Tatiana Gassmann und Andrea Riemensberger, vielen Dank für euer jederzeit offenes Ohr, die schnelle Unterstützung in allen administrativen Belangen und die herzliche Umsorgung.

Jede noch so gute Idee bedarf einer geeigneten technischen Umsetzung. Letztere verdanke ich in vielen Fällen dem Labor für Aufbau- und Verbindungstechnik um Oswald Speck und Florian Rupp, der Elektronik- und IT-Werkstatt

mit Martin Winkeler und David Guder, sowie der mechanischen Werkstatt mit Hans Bürger und Marco Hummel und ihren Teams. Vielen Dank für eure oft einfachen Lösungen zu kompliziert formulierten Problemstellungen.

Meinen Studenten Ahmed El Amri, Dr. Florian Eppler, Alexandra Krämer, Hana Alemeye, Leo Walkling, Johannes Müller und Marco Weber danke ich für ihre herausragenden Arbeiten. Es hat mir viel Spaß gemacht, mit euch zusammenzuarbeiten und ihr habt einen wesentlichen Anteil zu dieser Arbeit beigetragen.

Meinen Eltern Beate und Volker, meinem Bruder Victor und besonders meiner Freundin Marianne danke ich für ihre herzliche und aufmunternde Unterstützung über all die Jahre.

List of Publications

Journal publications

[P1] **S. Schneider**, M. Lauermann, P.-I. Dietrich, C. Weimann, W. Freude, and C. Koos, "Optical coherence tomography system mass-producible on a silicon photonic chip," Opt. Express Vol. 24, No. 2, 1573-1586, (2016)

[P2] **S. Schneider**, F. Eppler, M. Weber, G. Olowojoba, P. Weiss, C. Hübner, I. Mikonsaari, W. Freude, and C. Koos, "Multiscale dispersion-state characterization of nanocomposites using optical coherence tomography," Sci. Rep. 6, 31733 (2016)

Conference publications

[P3] **S. Schneider**, A. Krämer, F. Eppler, H. Alemye, C. Hübner, I. Mikonsaari, J. Leuthold, W. Freude, and C. Koos, "Polarization-sensitive optical coherence tomography for characterization of size and shape of nano-particles," in CLEO: Science and Innovations (2013), paper AF1J.4

[P4] **S. Schneider**, M. Lauermann, C. Weimann, W. Freude, and C. Koos, "Silicon photonic optical coherence tomography system," in CLEO: Applications and Technology (2014), paper ATu2P.4

[P5] **S. Schneider**, A. Krämer, F. Eppler, H. Alemye, C. Hübner, I. Mikonsaari, W. Freude, and C. Koos, "Polarization-sensitive optical coherence tomography for characterization of size and shape of nano-particles," in 115th Annual DGaO Conference (DGaO'14), talk A16 Deutsche Gesellschaft für angewandte Optik e.V. (DGaO) (2014)

[P6] **S. Schneider**, G. Olowojoba, I. Mikonsaari, W. Freude, C. Hübner, and C. Koos, "Optical coherence tomography for nanocomposite dispersion characterization," Inno.CNT Jahreskongress 2014 – Kohlenstoff Nanomaterialien

[P7] P.-I. Dietrich, I. Reuter, M. Blaicher, **S. Schneider**, M. Billah, T. Hoose, A. Hofmann, C. Caer, R. Dangel, B. Offrein, M. Möhrle, U. Troppenz, M. Zander, W. Freude, and C. Koos, "Lenses for Low-Loss Chip-to-Fiber and Fiber-to-Fiber Coupling Fabricated by 3D Direct-Write Lithography," in CLEO: Science and Innovations (2016), paper SM1G.4

[P8] W. Freude, **S. Schneider**, M. Lauermann, P.-I. Dietrich, C. Weimann, and C. Koos, "Silicon photonic integrated circuits for optical coherence tomography," 18th International Conference on Transparent Optical Networks (ICTON), 2016, paper Tu.C5.1 (invited)

[P9] W. Freude, **S. Schneider**, C. Weimann, F. Hoeller, M. Lauermann, P.-I. Dietrich, and C. Koos, "Integrated optics for optical coherence tomography and surface topography characterization," Light: Science & Applications, Light Conference, 2016, (invited)

[P10] C. Koos, W. Freude, A. Guber, T. Schimmel, M. Lauermann, **S. Schneider**, C. Weimann, S. Mühlbrandt, T. Harter, S. Wondimu, T. Wienhold, S. von der Ecken, P.-I. Dietrich, G. Goering, "Photonic Integration for Metrology and Sensing," Integrated Photonics Research, Silicon and Nanophotonics (IPR), 2017, paper Ith1A.1 (invited)

Patents

S. Schneider, C. Koos, W. Freude, and J. Leuthold: „Optisches Kohärenztomographiesystem mit erweitertem Dynamikbereich", Patent WO 2013/107621 A1, Application date: Jan. 2013

Karlsruhe Series in Photonics & Communications, Vol. 25
Edited by Profs. C. Koos, W. Freude and S. Randel

Karlsruhe Institute of Technology (KIT)
Institute of Photonics and Quantum Electronics (IPQ)
Germany

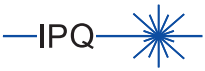

Nanocomposite materials play an increasingly important role in various application areas. A major challenge in the development of nanoparticles and nanocomposites is the control of particle size and shape, and of the uniform particle dispersion in the host material. Conventional characterization techniques lack either resolution, or can only inspect details of small samples. In this book, the application of optical coherence tomography (OCT) for nanocomposite and nanoparticle characterization is investigated. OCT is a three-dimensional imaging method with microscopic resolution. We follow a multi-scale approach: Along with imaging in the micrometre to millimetre regime, we employ a light scattering model to extend the measurement range towards nanoparticle sizes. Industrial use cases pose additional challenges to OCT systems, namely robustness, small system cost and size, and an open path towards parallelization. Photonic integrated systems comply with these requirements. We design and investigate silicon photonic integrated OCT systems that comprise interferometer and balanced photodetectors on a silicon chip.

About the Author

Simon Schneider was born 1984 in Filderstadt, Germany. In 2010, he received the Dipl.-Ing. degree in Electrical Engineering and Information Technology from Karlsruhe Institute of Technology (KIT). In 2019, he was awarded the Dr.-Ing. (Ph.D) degree in Electrical Engineering and Information Technology from KIT. His research focuses on optical metrology and on photonic integration.

ISSN 1865-1100
ISBN 978-3-7315-1027-7

Gedruckt auf FSC-zertifiziertem Papier